The Correction of Spiral Distortion in the Transmission Electron Microscope

A Thesis Submitted for the Degree

of

Doctor of Philosophy

in

The University of Aston in Birmingham

by

Shatha Mohammed Al Hilly

July, 1982

Department of Physics

THE UNIVERSITY OF ASTON IN BIRMINGHAM

THE CORRECTION OF SPIRAL DISTORTION IN THE TRANSMISSION ELECTRON MICROSCOPE

A THESIS FOR THE DEGREE OF
DOCTOR OF PHILOSOPHY
BY
Shatha Mohammed Al-Hilly, 1982

SUMMARY

The present investigation is concerned with the improvement of the image viewing and recording system of the transmission electron microscope, by means of a wide-angle projector lens of low distortion. A critical investigation of a previously proposed system for the correction of distortion by means of conventional magnetic lenses has been carried out; this showed that such lenses are not capable of providing a distortion free image with a projection semi-angle greater than about 10°. Theoretical and experimental investigation has shown that with projection semi-angles in the region of 30°, third order aberration theory is inadequate and can even be misleading. It was therefore desirable to calculate the actual axially symmetric trajectories of the electrons forming the projected image. Special attention was therefore paid to the development of a computer program for calculating the electron trajectory in a system of magnetic lenses with the aid of the general ray equation. Such a calculation allows one to determine the appearance of the final image directly without recourse to aberration theory. This direct image simulation has been achieved by using the output of the general ray program to print out the image of a square mesh grid on an x-y plotter. This enables a direct comparison to be made between the calculated and observed images. An experimental wide-angle lens has been constructed by computer-aided design, using the above principle. Essentially distortion-free images have been obtained over a semi-projection angle of 30°. It is believed that this represents an ultimate limit for a twin-lens design of this type. The projection lens system can find immediate application in TEMs with transmission fluorescent screens and also in high voltage electron mircoscopes.

Keywords

electron microscope, correction of distortion, wide-angle projector lens, lens aberration theory, general ray equation.

DEDICATED TO

MY MOTHER AND FATHER

ACKNOWLEDGEMENTS

I would like to express my sincere gratitude to my supervisor, Professor T. Mulvey, for his advice and supervision throughout the course of the present investigation.

I am indebted to Mr. R. Keen of the Physics Department for considerable technical assistance and to the staff of the physics workshop for the practical realization of the lens design described in this thesis.

Thanks are due to Mr. A.W. Agar of Agar Aids, Mr. K. Anderson of VG Scientific formerly concerned with the AEI Corinth Electron Microscope and Mr. P.B. Kenway of the Department of Metallurgy. UMIST Manchester for helpful discussion on the design of the viewing system of the Corinth Electron Microscope.

I would like to acknowledge my colleagues, Dr. H. Elkamali, Dr. H. Nasr, Mr. S. Christofides, for their helpful discussion.

A sincere acknowledgement is made to Miss Jean Whitmore for conscientiously typing the manuscript.

Especially deep is my indebtedness to my family whose encouragement was indispensable. In particular I would like to thank my Father and Mother.

CONTENTS

Appendices 118

LIST OF FIGURES

Figure Number | Figure Title | Page

LIST OF SYMBOLS

a	Acceleration
A	Magnetic vector potential
$A(z,r)$	The magnetic vector potential for z and r coordinates
A_θ	Azimuthal component of the magnetic vector potential
B	Magnetic flux density
B_r	Radial component of the magnetic flux density
B_z	Axial component of the magnetic flux density
$B_{(r,z)}$	Total flux density at height r and distance z
D_{rd}	Radial distortion coefficient
e	Electron charge
E	Electric field strength
f_p	Projector focal length
F_e	Electric field force
F_m	Magnetic field force
L	Projection length
ℓ	Distance between corrector and projector lens
ℓ_p	Distance between final projector and viewing screen
M	Magnification
m	Mass of the electron
n	Scaling factor
NI	Lens excitation
$NI/\sqrt{V_r}$	Excitation parameter
Q_{rd}	Radial quality factor

Q_{sp}	Spiral quality factor
r	Ray height
r_o	Initial ray height
r'	Slope of ray
r'_o	Initial slope of ray
S	Gap width
T_{INT}	Time interval
V	Accelerating voltage
V_r	Relativistically corrected accelerating voltage
v_r	Velocity in the r direction
v_z	Velocity in the z direction
W	Energy of the electron
X_o, Y_o	Coordinates of a point
Z	Axial distance
$\ddot{Z}$	Axial acceleration
Zscreen	Distance between final lens and screen
α_p	Projection semi-angle
γ	Inclination angle
$\eta (= e/m)$	Charge to mass ratio of electron
ρ	Radial height in the image
ρ_G	Radial height in Gaussian image
$\Delta\rho$	Displacement of an image point from the Gaussian position
$\frac{\Delta\rho}{\rho}$	Relative distortion
θ	Image rotation angle
θ_o	Image rotation (Gaussian approximation)
$\dot{\theta}$	Angular velocity
$\delta\theta$	Angular deviation

CHAPTER 1

INTRODUCTION

1.1 THE ELECTRON MICROSCOPE

In recent years, the electron microscope with its wide variety of electron optical techniques and accessories has reached a high level of performance. It is an indispensible research instrument in the most diverse branches of biology, medicine and material sciences. The most common element of all types of electron microscopes is the magnetic electron lens. Recent developments in improving the performance of the electron microscope has included illuminating systems, vacuum technique, image handling, processing and photographic recording of the image. A further improvement is the use of the image intensifier to reveal the image on the transmission fluorescent screen or on a TV monitor. This can be useful for observing the image in a non-darkened room with a sufficient brightness of the image. However, some of these developments have raised imaging problems that cannot be solved by minor modifications to classical designs. In particular, attention should be paid to improving the projection system and the viewing arrangements.

1.2 VIEWING ARRANGEMENTS IN THE TEM

An ideal projection system should produce a magnified and distortion-free image of the object. This image can be viewed on a fluorescent screen, from which a selected field of view can be recorded. This can either be done by direct exposure on a photographic plate or on a TV monitor, or even by video recording so that dynamic experiments can be performed and recorded; the resulting data can then be extracted at leisure. Because of radiation damage, the electron beam flux at the specimen cannot be increased beyond a certain minimum value and hence the required detail should be established by the minimum number of electrons. Unfortunately, the stray a.c. magnetic field in the viewing chamber may prevent this since the length of the viewing chamber is large (typically of the order of 50cm). This sensitivity to stray magnetic fields decreases with the square of the projection length. Such a reduction is also useful in reducing the effects of mechanical vibrations, since it reduces the total height of the column. However, the final projection lens gives rise to spiral distortion (see section 1.7) which, unlike radial distortion, is surprisingly difficult to correct (Marai and Mulvey, 1977). A distortion-free projection system would enable an appreciable reduction to be made in the projection length and hence a considerable improvement to be made in instrumental performance.

In normal operation most operators prefer to tilt the viewing screen at a convenient angle so that the screen is at right angles to the direction of vision. This, however, will lead to keystone distortion. The term keystone is used by analogy to the keystone at the top of an arch, locking other stones into position. This distortion not only alters the magnification but also the shape of the image projected onto the tilted screen.

1.3 THE ELECTRON OPTICAL COLUMN

The main constructional features of electron optical columns are basically similar, although slight differences arise between different instruments. Because different fields of research make different demands on the instrument, emphasis on certain features, according to its usefulness to the users, is likely to be found. However, the prices of commercial instruments vary considerably according to the precise facilities required and the resolving power specified.

Although much effort has been directed towards higher resolution, the full operational advantages of high resolution microscopy cannot be realized in practice unless more attention is paid to the projection system, the viewing arrangements and the image recording facilities. Before considering the design of the viewing arrangements in TEM it may be useful to look critically at some commercial microscopes.

Figure 1.1 shows the cross-section of the Zeiss EM10 high resolution transmission electron microscope.

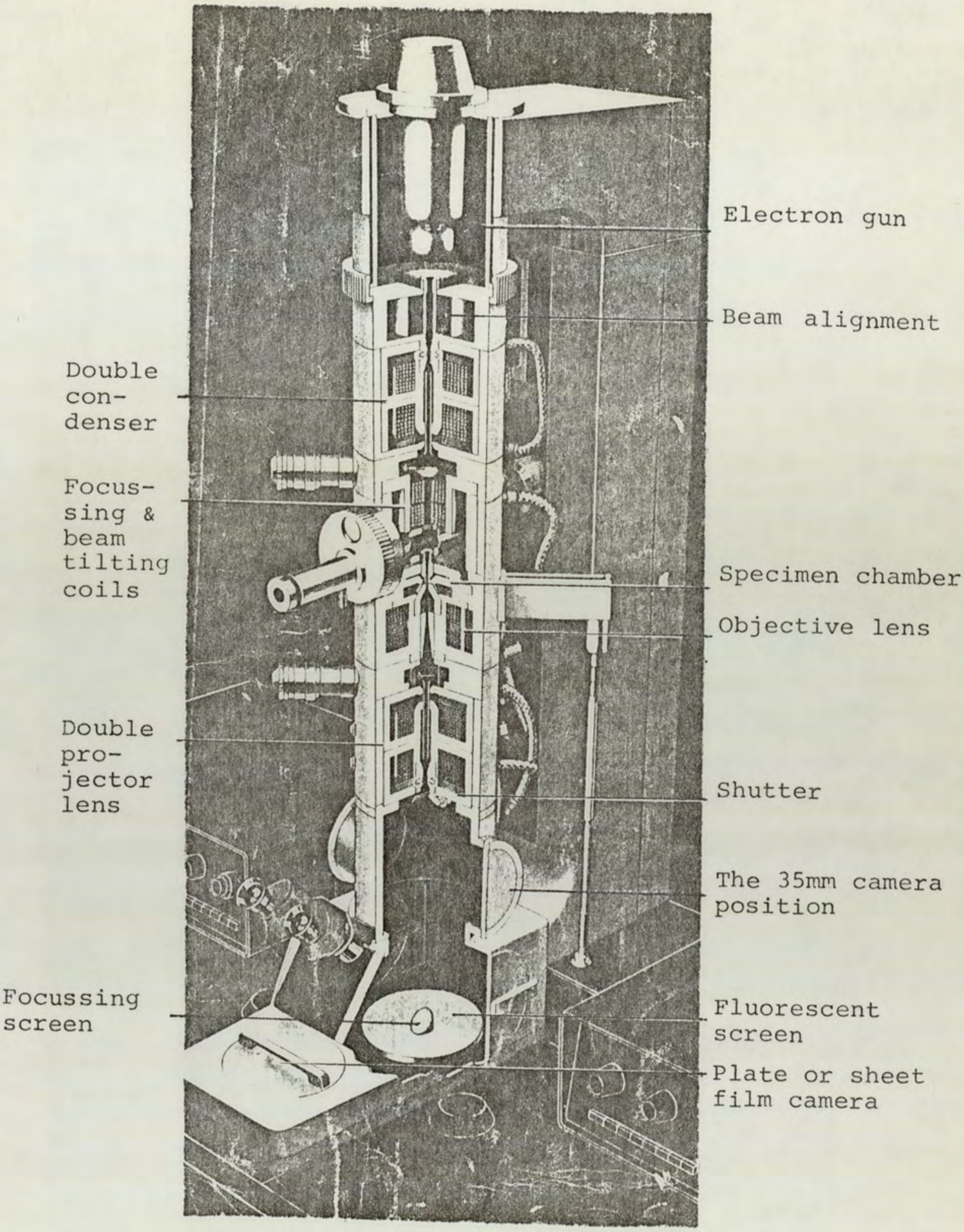

Figure 1.1: Cross section of the Zeiss EM10 high resolution transmission electron microscope.

It is a typical example of the design of a high performance electron microscope; incorporating two cameras, two fluorescent screens, as well as the possibility of fitting extra analytical accessories, such as a TV monitor or a spectrometer.

In this instrument the objective lens produces an intermediate image which is further magnified by the double projector lens system, the final image being formed on the fluorescent screen. It can be recorded on either a photographic plate or by a 35mm camera which can be fitted in the most desirable position, i.e. between the final projector lens and the fluorescent screen. This position is desirable since finer image details can be recorded on photographic plates than can be seen on the fluorescent screen because of the inferior resolution of the screen compared with that of the photographic plate. Placing the camera in this position has the advantage of fitting some accessories, such as the image intensifier or spectrometer, permanently and without interfering with photography.

The present investigation is also relevant to a TEM fitted with a transmission fluorescent screen. A typical example is found in those instruments with a short and inverted column like the AEI Corinth 275 TEM, shown in Figure 1.2, or the JEOL Superscope 30 KV TEM, with a tilted column, Figure 1.3.

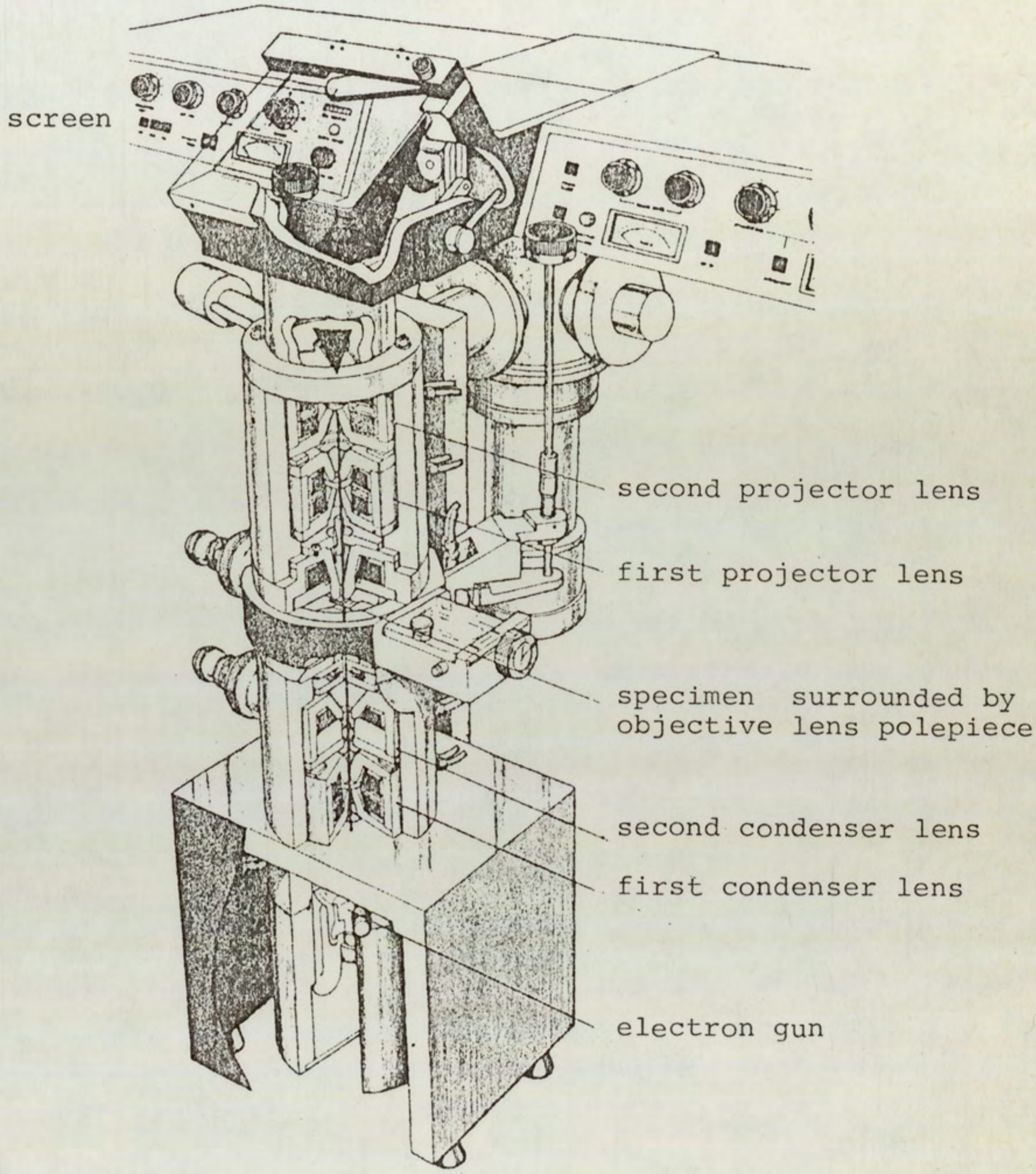

Figure 1.2: Cross section of the AEI Corinth 275 transmission electron microscope with a transmission fluorescent screen.

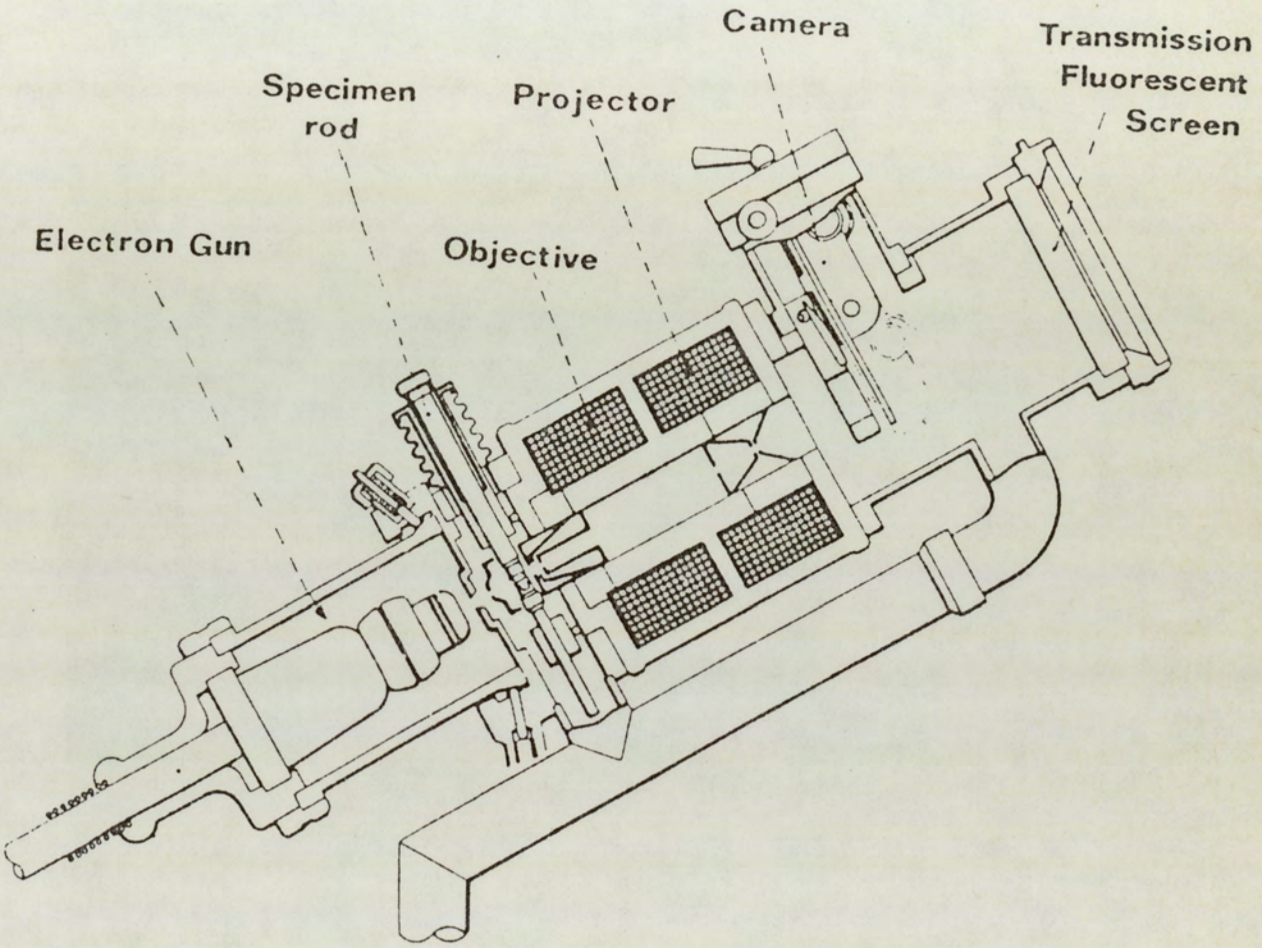

Figure 1.3: The JEOL JEM Superscope 30 KV TEM with transmission fluorescent screen and internal camera of 6.4° projector semi-angle.

1.4 THE CORINTH VIEWING SYSTEM

The Corinth electron microscope (Figure 1.2) has an inverted column; a 60 KV electron gun is located at the base of the column and the screen is at desk level. The electron column has five lenses, a double condenser lens, an objective lens and two projector lenses. All the lenses are magnetic and water cooled. The image is projected onto a comparatively large transmission viewing screen, 165mm square (i.e. 6.5 inches square) which is not obstructed by the electron optical column and whose centre is 7.5mm above the optical axis of the microscope. The square transmission screen is inclined at 30° to the horizontal for convenience in viewing. This, however, introduces keystone distortion (16%). Although most commercial microscopes produce about 14% when their reflection screen is tilted, it is more noticable in a transmission fluorescent screen, i.e. external photography should be avoided. A tilted screen will mask appreciable spiral distortion because of the presence of keystone distortion. Of course, this will not affect the images taken on an internal camera mounted at right angles to the lens axis.

Figure 1.4 is a schematic diagram of the viewing arrangement of the Corinth microscope. The distance L_s between the point at which the electrons cross the optical axis, after the final projector lens and the screen (i.e. the projection distance), is 291mm. The distortion at the edge of the screen amounts to some 15% (see Figure 1.4). The Corinth microscope is fitted with a 70mm roll film

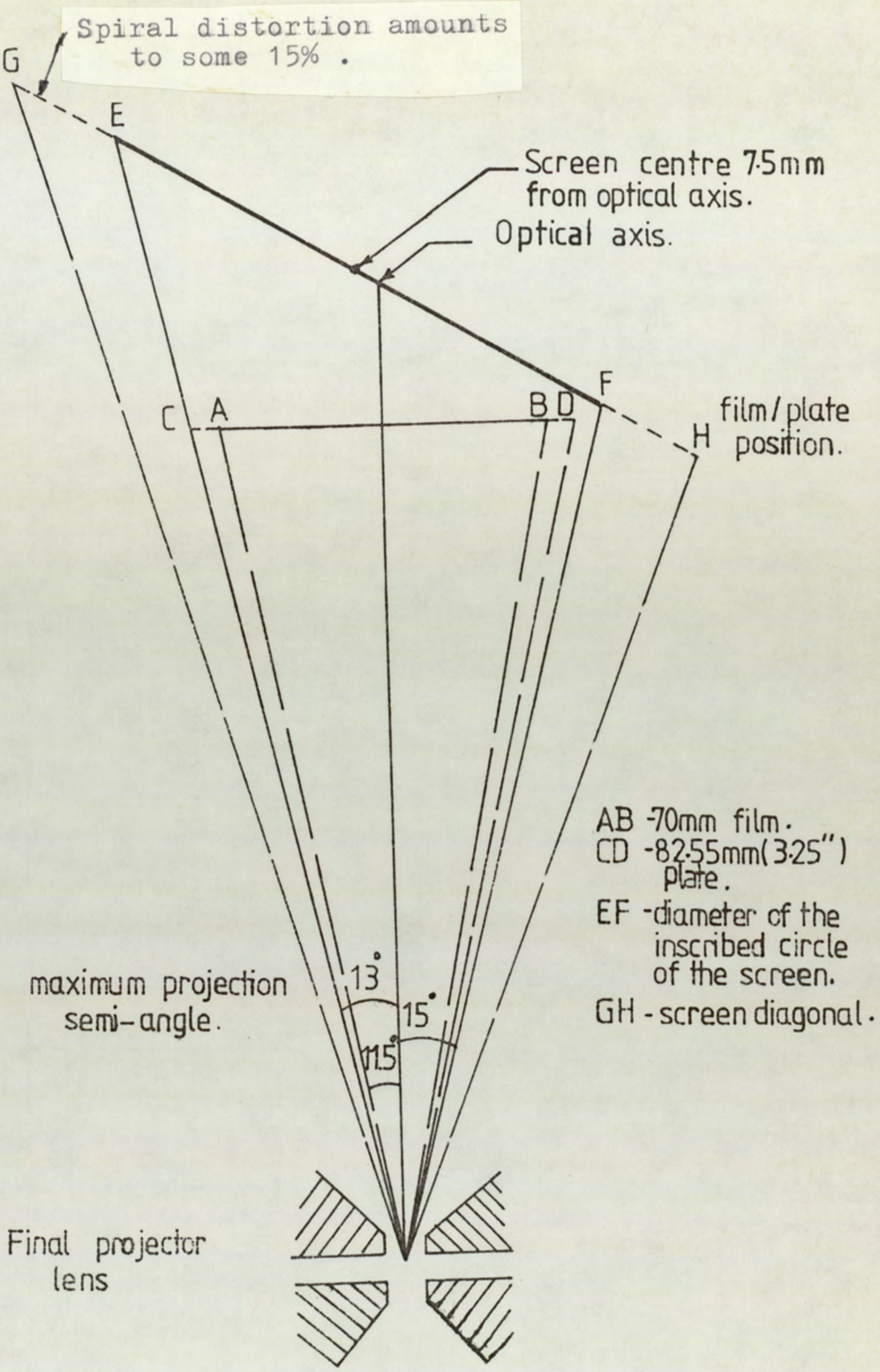

Figure 1.4: Cross section of the viewing chamber of the AEI Corinth 275, with transmission screen tilted at 30° to the photographic plates across the diagonal of the screen and the photographic plates showing corresponding maximum projection semi-angle.

camera.

The film is located 249mm from the back focal point of the final projector lens according to the manufacturer's data. This gives a semi-projection angle of 8°. The spiral distortion at the edge of the 70mm film is 4% . The 70mm film camera can be replaced by the larger 82.55mm (3¼ inch) plates. The projection semi-angle is then increased to 9.4° leading to a maximum image distortion of about 5.5% at the corner of the plate.

Placing the photographic film or plate in the most desirable position together with the short projection distance and the wide field of view makes the Corinth microscope's viewing arrangement unique. However, the amount of distortion present is excessive. This is inevitable with conventional double-polepiece lenses.

1.5 THE JEOL SUPERSCOPE 30 KV TEM

Unlike the Corinth microscope, the JEOL Superscope's column has its axis inclined at an angle of 30° to the horizontal (as shown in Figure 1.3). In this way, the screen need not be tilted like the Corinth's screen but still offers the same convenience to the operator. It has only two lenses: an objective and a projector, but no condenser lens. The viewing chamber of this microscope is the chief item of interest in the present investigation, since the image is projected onto a large transmission fluorescent screen. The photographic film camera is fitted in the optimum position inside the column, i.e. between the projector lens and the fluorescent screen, but the size of the photographic film is only 25mm x 25mm, too small for serious electron microscopy.

The viewing chamber of the JEOL Superscope is illustrated in Figure 1.5. The large transmission-fluorescent screen of 104mm in diameter, 200mm away from the final projector is quite impressive. It gives a projection semi-angle of 14°. Nevertheless, the amount of distortion present near the edge of the screen is excessive (7%). Fitting the photographic film camera in its optimum position inside the column reduces the projection length to 76mm. This arrangement gives a projection semi-angle of about 6.4°. This, of course, reduces the maximum image distortion to the acceptable values of 2% spiral and 1% radial distortion. However, it limits the field of view to a projection semi-angle of 7°. Limiting the field of view that can be photographed to reduce the image distortion in the micrograph is the usual method adopted by almost every commercial microscope manufacturer.

The JEOL Superscope 30 KV TEM has been adapted in the present investigation because of its availability in the department and its good viewing arrangement, i.e. short projection length, large transmission fluorescent screen perpendicular to and centered on the optical axis and free from keystone distortion.

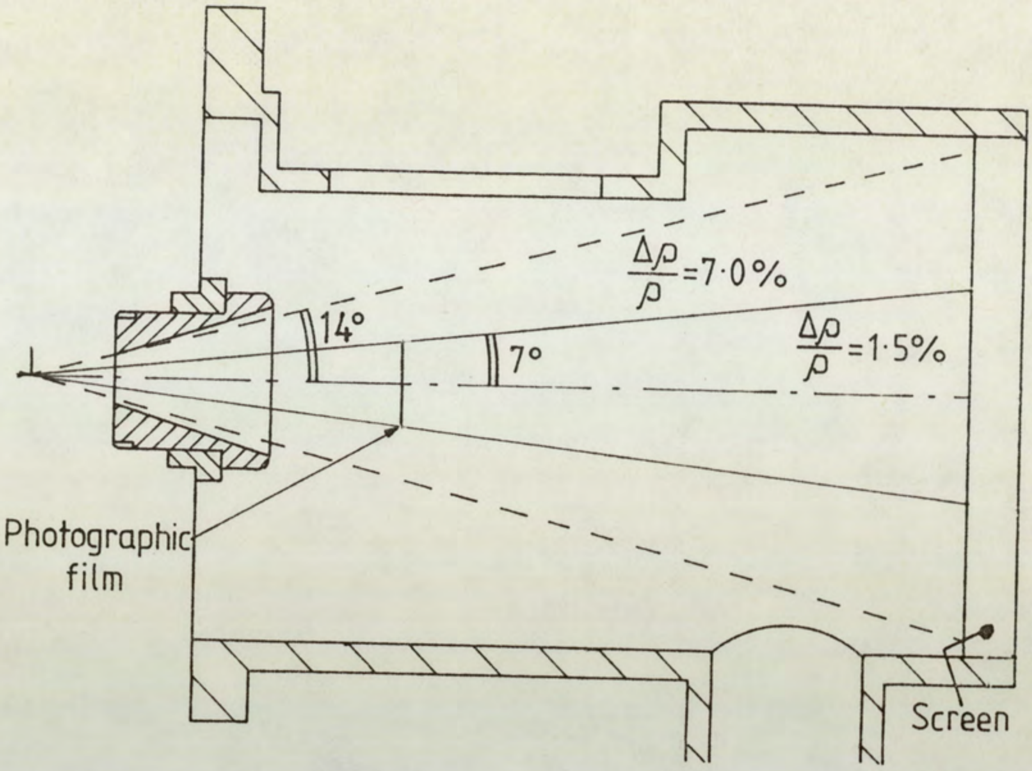

Figure 1.5: The viewing chamber of the JEOL Superscope fitted with an internal camera and a transmission fluorescent screen. The maximum projection semi-angle of the camera is 7°. The projection angle of the viewing screen is 14°.

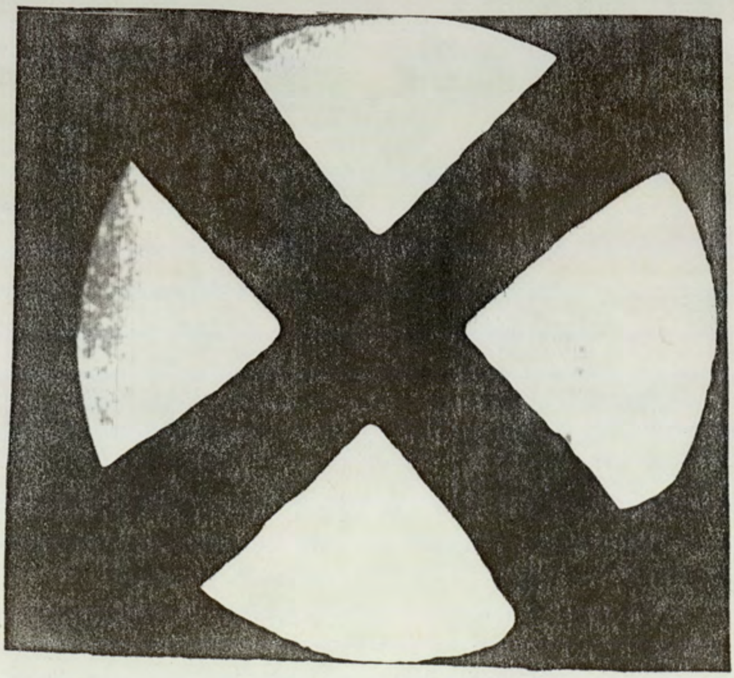

Figure 1.6: Appearance of the image (external photography) on the fluorescent screen of the 'Superscope' showing considerable distortion (7%) on the edge of the screen.

1.6 MAGNETIC LENSES

Magnetic lenses generally produce a magnetic field by an energized coil surrounded by an iron circuit. These lenses are either conventional lenses which in turn could be symmetrical (Figure 1.7a) or of asymmetrical polepiece shape (Figure 1.7b) or single polepiece lenses (Figure 1.7c). The magnetic field distribution will differ from one type of lens to another depending on the position of the coil and the shape of the iron circuit. At the beginning of the development of electron optics, different mathematical models were proposed to represent the field distribution as a function of the axial distance Z. An example of this would be the rectangular field model, where $B_Z = B_O$ for $-S/_2 < Z < S/_2$ and zero for other values. This is a purely mathematical model to simplify the field calculations.

The development of the electron lens design does not consist in the determination of the field distribution alone, but also on its electron optical properties, which are of great importance. Since the optical properties depend mainly on the magnetic field distribution and its derivative, the direction of the incident electron beam is important in the case of an asymmetrical field. The single polepiece lens is a typical example of an asymmetrical field. Here the bore diameter controls the steepness of the rapidly rising part of the field; decreasing the bore diameter

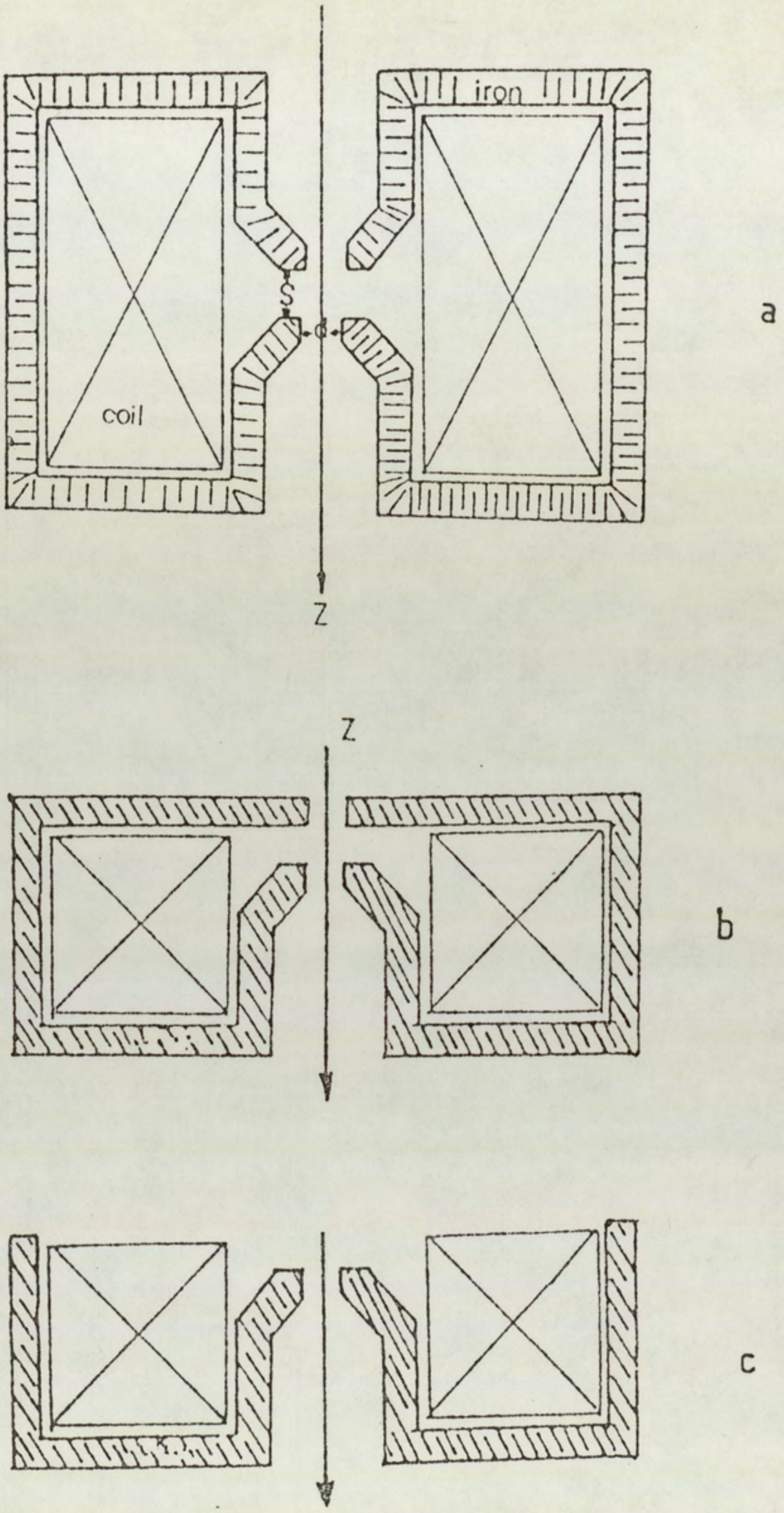

Figure 1.7: Schematic diagram showing various types of magnetic lenses;
a - Double polepiece symmetrical lens
b - Double polepiece asymmetrical lens
c - Single polepiece lens

makes the field rise more steeply (Juma and Mulvey, 1979). This asymmetrical characteristic gives the possibility of using the single polepiece lens in two different modes of operation. The first arises when the polepiece of the lens is facing the incoming electron beam (preferred direction for the projector lens) and the second when the polepiece is facing the screen (non-preferred direction). It has been shown (Marai and Mulvey, 1976) that the lens has a lower distortion coefficient by a factor of about 2.5 when used in the preferred direction than when it is used in the non-preferred direction. This fact can be turned to advantage in the correction of distortion in the electron microscope as can be seen in chapter four.

1.7 ABERRATION OF MAGNETIC PROJECTOR LENSES

Ideally the image produced by a magnetic projector electron lens should be perfectly formed if the electrons follow Gaussian trajectories. The paraxial ray equation applied to the Gaussian trajectories is given by:

$$\frac{d^2r}{dZ^2} + \frac{\eta}{8V_r} B_z^2 r = 0 \qquad (1.1)$$

where V_r is the relativistic accelerating voltage, B_z is the axial flux density and $\eta = e/m$ is the charge to mass ratio of the electron . In general, the electrons do not follow Gaussian trajectories. The departure of the electrons from the Gaussian trajectories is called the aberration. It is usually defined in the Gaussian image plane.

Since a projector lens operates at a very small angular aperture of the ray pencils, it therefore contributes virtually no spherical aberration to the image. This means that the sharpness of the image will not be affected by the spherical aberration of the projector lens. However, image distortion will inevitably arise. Distortion causes a deviation in the image of an object from its Gaussian position. The displacement of an image point may be in the radial direction (radial distortion) and/or the circumferential direction (spiral distortion). Radial distortion takes place if the lens refractive power does not vary linearly with the height of the incoming rays. Spiral distortion takes place if the angle of rotation, a characteristic of magnetic lenses, is dependent on the radial height of the incoming rays from the axis.

Figure 1.8 illustrates radial image displacement, i.e. either towards or away from the centre of the image (radial distortion) or along a circular arc either anticlockwise or clockwise, according to the direction of the current in the lens coil (spiral distortion).

The deviation $\Delta\rho$, in Figure 1.8 of an image point from the corresponding Gaussian image of radius ρ, represents the amount of distortion present in the image. Generally, one refers to relative distortion $\Delta\rho/\rho$ in measuring the distortion aberration in any electron microscope image. In general, $\Delta\rho/\rho$ varies with the square of the height r of the incoming rays.

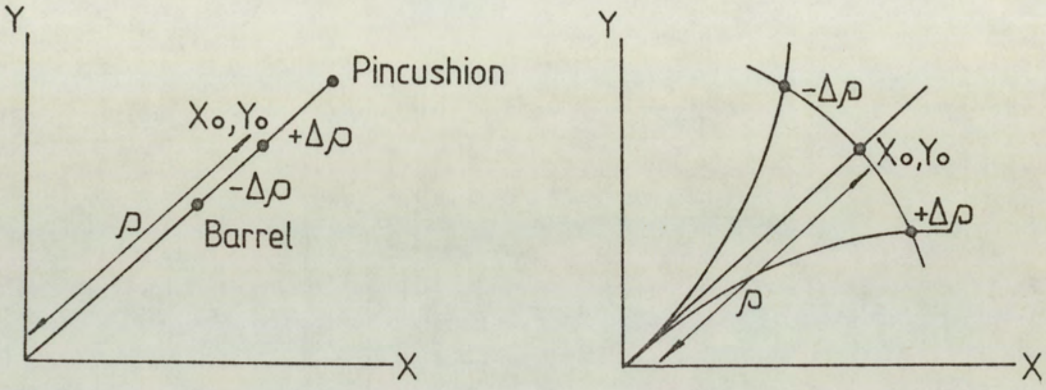

a) Radial distortion b) Spiral distortion

Figure 1.8: The Gaussian image point (X_O,Y_O) and the image displacement (distortion) according with (a) radial and (b) spiral distortion.

1.7.1 RADIAL DISTORTION

In radial distortion, the image of each object point is shifted radially from the Gaussian image point as shown in Figure 1.9. In this figure, a ray of height r entering a lens of bore radius R, ideally reaches the screen at height ρ if the lens has no aberration. Indeed, the radial aberration shifts the ray by a distance $\Delta\rho$ from the Gaussian image point. L here shows the projection distance from the focal point of the lens to the screen.

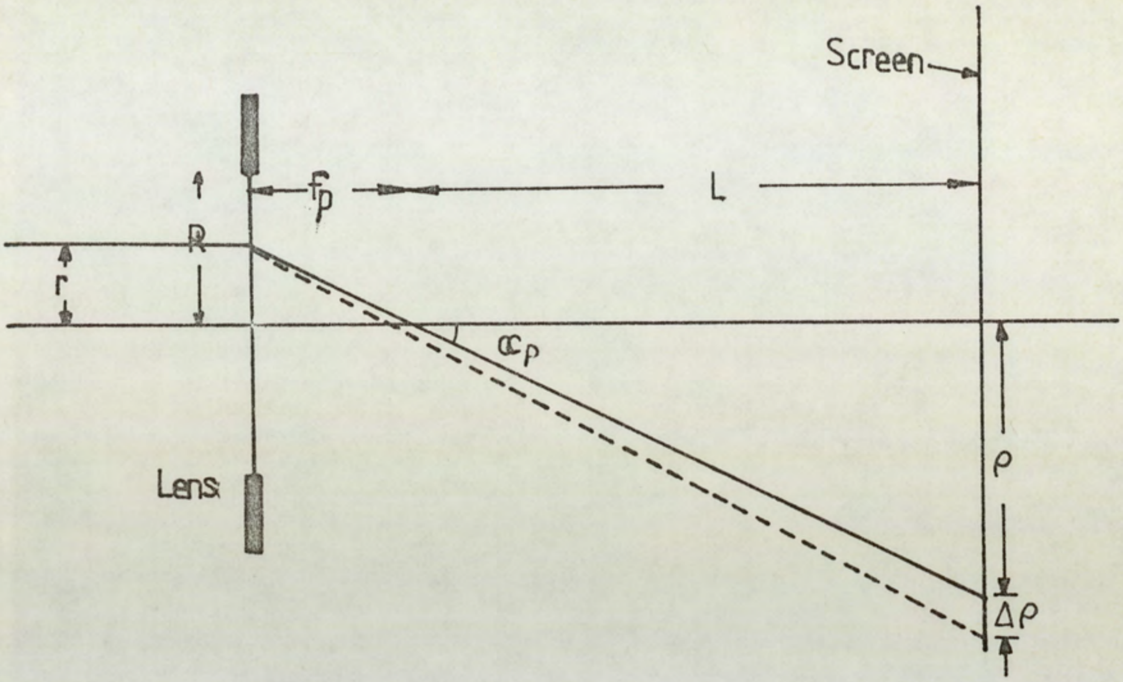

Figure 1.9: Ray diagram illustrating geometrical relations in the final projection lens; r, fp, L, αp are the height of the incoming ray, the projector focal length, the projection length and the projection semi-angle, respectively.

The radial displacement Δρ from the Gaussian image point is given by the following equation:

$$\Delta\rho_{rd} = M\, D_{rd}\, r^3 \qquad (1.2)$$

where r is the height of the incoming ray from the axis (Figure 1.8), M the lens magnification and D_{rd} the radial distortion coefficient.

The general appearance of a projected image of a rectangular grid suffering from radial (barrel (a) and pincushion (b)) distortion is shown in Figure 1.10.

Radial distortion may change from 'pincushion' distortion to 'barrel' distortion by suitably changing the excitation of the lens. This fact suggests for every lens there is a certain excitation value (near its minimum focal length) for which radial distortion vanishes (see Figure 4.9).

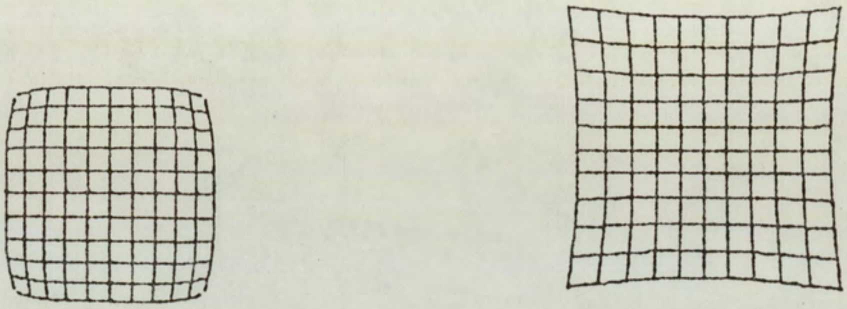

(a) Barrel distortion (b) Pincushion distortion

Figure 1.10: The effect of radial distortion on the appearance of an image of a rectangular mesh grid. Negative $\Delta\rho$ causes barrel distortion and positive $\Delta\rho$ causes pincushion distortion.

1.7.2 SPIRAL DISTORTION

In a magnetic lens, the magnetic field $B(Z,r)$ is a function of both the axial distance (Z) and the radial height r. So the rotation of the image θ will vary with the radial height accordingly. In other words, the rotation of the image is expressed by:

$$\theta = \theta_o + \delta\theta \qquad (1.3)$$

where θ_o is the Gaussian image rotation and $\delta\theta$ the spiral distortion. This actually shifts the Gaussian image (X_o, Y_o) of Figure 1.8b by a distance $\Delta\rho$, measured along a circular arc of radius ρ. Generally, this displacement increases with the cube of the radial height r, as given by

$$\Delta\rho_{sp} = M\, D_{sp}\, r^3 \tag{1.4}$$

where D_{sp} is the coefficient of spiral distortion.

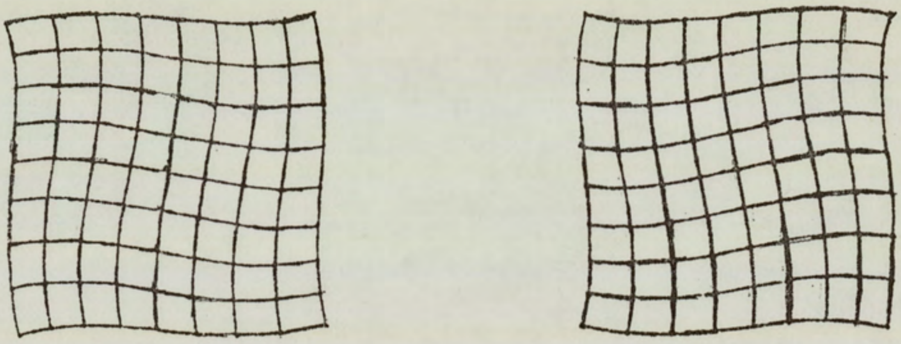

anticlockwise clockwise

Figure 1.11: The effect of spiral distortion on the image of a rectangular mesh grid. Note - On reversing the current of the lens, the direction of distortion is also reversed.

The effect of spiral distortion on the image of a square grid is shown in Figure 1.11. In this figure it is shown that reversing the current of the lens changes the sign of the image rotation and so does the spiral distortion. Consequently, this may give the impression that spiral distortion could easily be corrected by compensating the distortion of the final projector lens by using an intermediate lens with spiral distortion in the opposite direction. This, however, is found surprisingly difficult to achieve in practice (Marai and Mulvey, 1977). as explained in Section 1.8 .

1.7.3 THE DISTORTION QUALITY FACTOR

The geometry of Figure 1.9 gives the relation

$$\frac{L}{f_p} = \frac{\rho}{r} \qquad (1.5)$$

where L is the projection length, f_p is the projector focal length and ρ is the off-axis distance for the projected image on the screen. Hence, the height of the incident ray r will be

$$r = f_p \frac{\rho}{L} \qquad (1.6)$$

substituting the value of r and the value of the magnification M, where $M = \frac{\rho}{r}$ in equation (1.2), gives an image distortion $\frac{\Delta\rho}{\rho}$ as

$$\left(\frac{\Delta\rho}{\rho}\right)_{rd} = D_{rd}\, f_p^{\,2}\, \frac{\rho^2}{L^2} \qquad (1.7)$$

From Figure 1.9, $\tan \alpha_p = \frac{\rho}{L}$ where α_p is the projection semi-angle. Hence:

$$\frac{\Delta\rho}{\rho}_{rd} = D_{rd}\, f_p^{\,2} \tan^2 \alpha_p \qquad (1.8)$$

Marai and Mulvey, 1977, introduced the expression "quality factor (Q)" with Q^2_{rd} to stand for the product

$(D_{rd}f_p^2)$. This dimensionless quantity actually gives a good guide to the performance of the lens. Moreover, it reveals that the amount of distortion present in a magnetic lens cannot be measured by the distortion coefficient D only. For example , the image distortion $\frac{\Delta\rho}{\rho}$ does not necessarily tend to zero when the coefficient D approaches zero, since the focal length f_p tend to infinity. Similarly,

where $(\frac{\Delta\rho}{\rho})_{sp}$ is given by

$$\frac{\Delta\rho}{\rho})_{sp} = D_{sp} f_p^2 \tan^2 \alpha_p \qquad (1.9)$$

and Q^2_{sp} as well is similarly used for the product $(D_{sp}f_p^2)$.

Note - Q_{sp} and Q_{rd} are dimensionless. This shows that scaling a lens does scale the focal length accordingly but will not change image distortion $\Delta\rho/\rho$. This can also be seen by considering the scaling laws for magnetic lenses described in Appendix A.

1.8 PREVIOUS ATTEMPTS AT CORRECTING DISTORTION IN EM

The design of the projector lens and viewing system is largely limited by the difficulty of reducing the radial and spiral distortion in the final projector to the generally agreed tolerable limits of 1% radial and 2% spiral distortion in the micrograph. Most commercial microscopes achieve these limits by restricting the semi-projection angle (α_p) of the beam projected onto the fluorescent screen to about 0.1 radian (5.7°) and by operating the projector lens at its minimum focal length to eliminate radial distortion and where minimum spiral distortion occurs (Liebmann, 1952). This actually leads to bulky viewing chambers.

If the distortion of the projector lens could be corrected, new possibilities would be opened for the design of the viewing system. Thus, Hillier (1946) showed that radial image distortion could be eliminated by placing an auxiliary lens of suitable strength at the back focal point of the final projector lens. Unfortunately, the auxiliary lens was wasteful in that it contributed nothing to the instrumental magnification. In addition, a single coil was employed to energize the two lenses which meant that, although radial distortion was eliminated, spiral distortion was increased since image rotation was additive. Moreover, the projection semi-angle was of the order of 6°.

In 1963, Kynaston and Mulvey proposed the system shown in Figure 1.12 for correcting radial distortion at low magnification. They suggested that the intermediate lens can be set to produce an intermediate image with barrel distortion which will tend to cancel the pincushion distortion produced by the final projector lens. This method has the advantage that it does not depend critically on the focal length or the design of the lenses used. However, it did not solve the problem of achieving large projection semi-angles because of the difficulties in correcting spiral distortion.

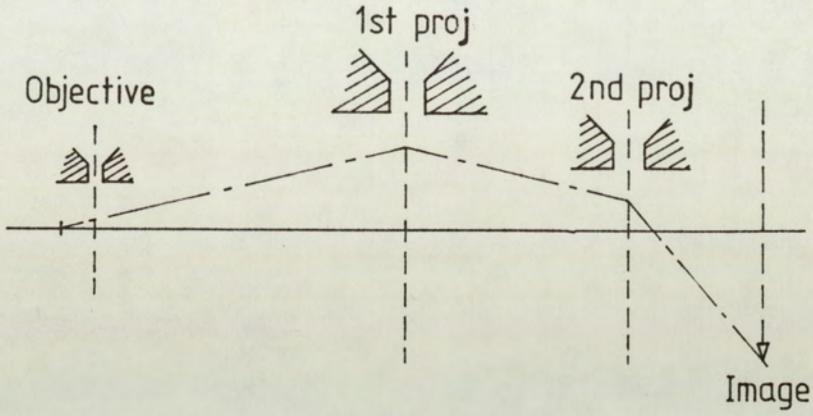

Figure 1.12: Correction of radial distortion (Kynaston and Mulvey, 1963) showing the ray path through the system.

An improvement to the Hillier (1946) two-lens projection system was carried out by Juma and Mulvey (1974, 1975, 1978). Here, the coil of each of the magnetic lenses of the doublet was energized with the same current but passing in opposite directions so to eliminate image rotation, Figure 1.13.

In this twin-lens system, radial distortion was eliminated but spiral distortion correction could not be achieved completely, besides the restriction of the projection semi-angle ($\alpha_p = 3^\circ$), because of the smallness of the lens bores (2mm diameter). An improvement of 50% correction could be reached as the two lenses moved closer to each other (Marai, 1977).

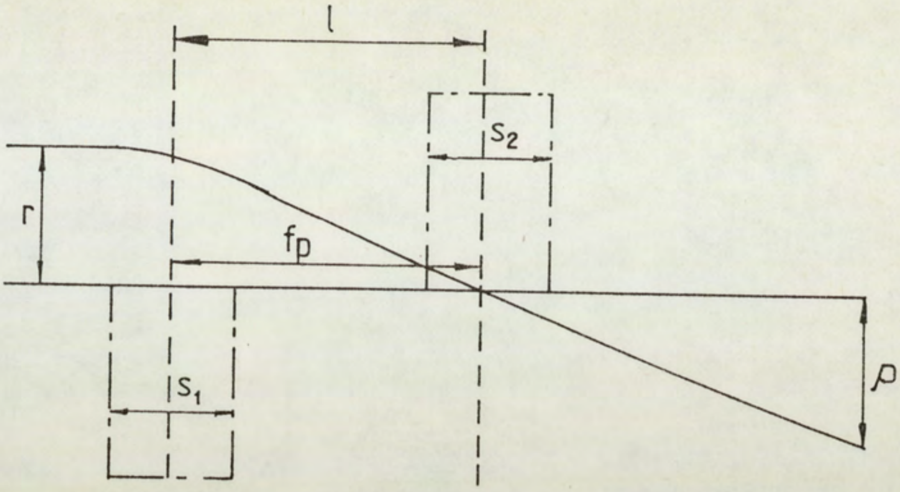

Figure 1.13: Schematic ray path corresponding to the rotation-free lens doublet (Juma and Mulvey, 1978).

Lambrakis et. al. (1977), took up the suggestion made by Mulvey (1976), of using two miniature single polepiece lenses for realizing an experimental wide-angle projection system. This system took into account some special features of the projector lens; namely that the distortion coefficients vary with change of conjugates. In general, the aberration of a lens is smaller for infinite conjugates (i.e. image or object distance equal to infinity) than for finite conjugates. In other words, distortion coefficient increase as the conjugates become smaller. Furthermore, the corrector lens magnification affects the amount of correction that it can contribute to the final image. In addition, the influence of field asymmetry on the aberration of a single polepiece lens can be used to increase the correcting action. Figure 1.14 shows the experimental arrangement for investigating the effectiveness of this approach.

The separation between the opposing polepieces was made adjustable by inserting a vacuum liner tube through the base of the correction lens so that the corrector could slide up and down without affecting the vacuum. A separation of 60mm was found suitable with the two lenses excited at $NI/\sqrt{V_r})_{proj} = 15.5$ and $NI/\sqrt{V_r})_{corr} = 34$.

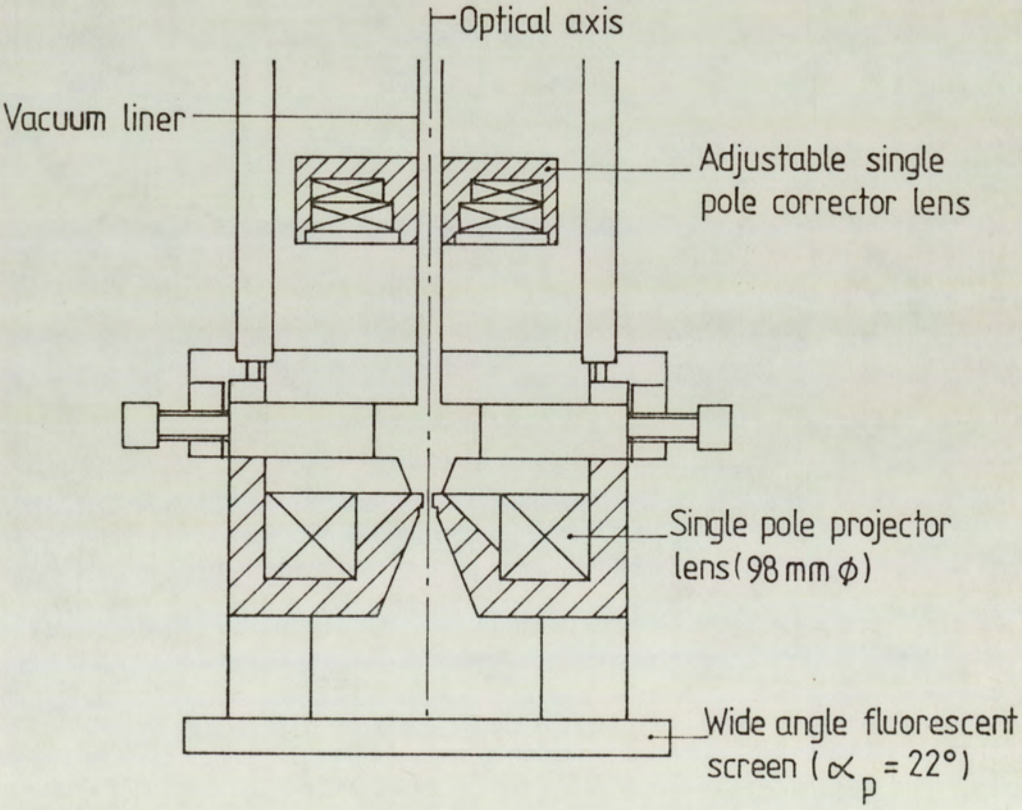

Figure 1.14: The arrangement for correcting spiral distortion (Lambrakis et. al., 1977) using two single polepiece lenses. Projector excitation parameter $NI/\sqrt{V_r} = 15.5$. Corrector excitation parameter = 34.

An image of less than 3% spiral distortion was produced at a projection semi-angle of 22°. The main drawback of this design is the necessity to adjust the separation of the lenses under vacuum. In addition, there is field cancellation by the opposing lens fields; this amounted to about 25% at a snout separation of 60mm. An 'Intercol' electron optical bench was used, forming a shadow image on the transmission fluorescent screen throughout the above investigation.

Further tests were carried out using a 100 KV TEM (Elkamali and Mulvey, 1977). The viewing chamber of an EM6 electron microscope was reduced in length from 23.5 to 14.9cm. The projection system was replaced by two single polepiece lenses as shown in Figure 1.15.

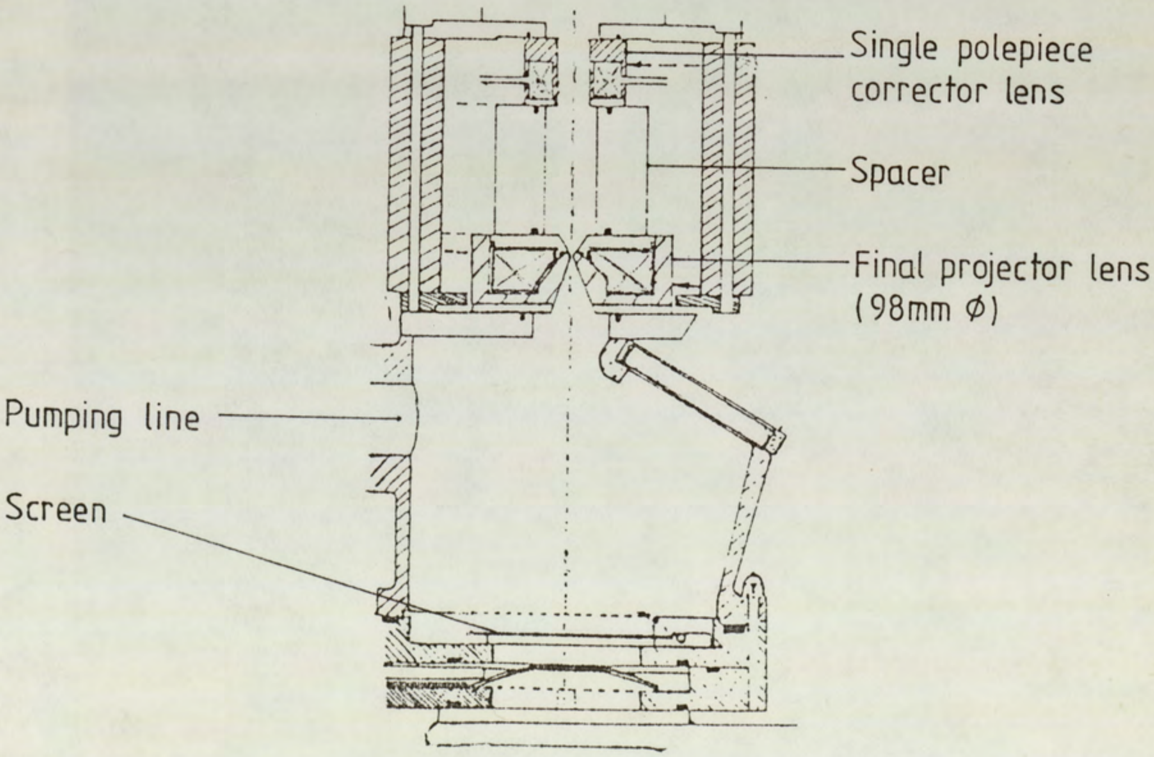

Figure 1.15: Improved projection system of Elkamali and Mulvey (1977) in an EM6 electron microscope.

The experimental result of Elkamali and Mulvey (1977), showed that the spacing between the corrector and the projector lens is critical. For example, a change in separation of ±2mm changes the distortion by about 1% (Elkamali, 1981). An improved wide-angle ($\alpha_p = 30^\circ$), projection system has been devised by Elkamali and Mulvey (1980a,b). This system actually makes use of a virtual image produced by the corrector lens. A light optical analogue consisting of three thin glass lenses has been used to represent the above system and the forming of the virtual image. Figure 1.16 shows the actual system.

The experimental result of Elkamali (1981) has shown that it is quite possible to obtain a satisfactory correction of radial and spiral distortion simultaneously with the system described in Figure 1.16. This system, in fact, operates in the first focal zone, at the high excitation end of this zone. However, the design's most serious disadvantage is the necessity for achieving good alignment, and in adjusting experimentally the position of the two lenses and the middle plate. Moreover, the field cancellation in the system was still too high, (around 20%).

In this investigation, therefore, a theoretical and experimental programme has been carried out on these lines construct a wide angle distortion-free projection system of integral construction for all forms of electron microscope but especially for high voltage microscopes

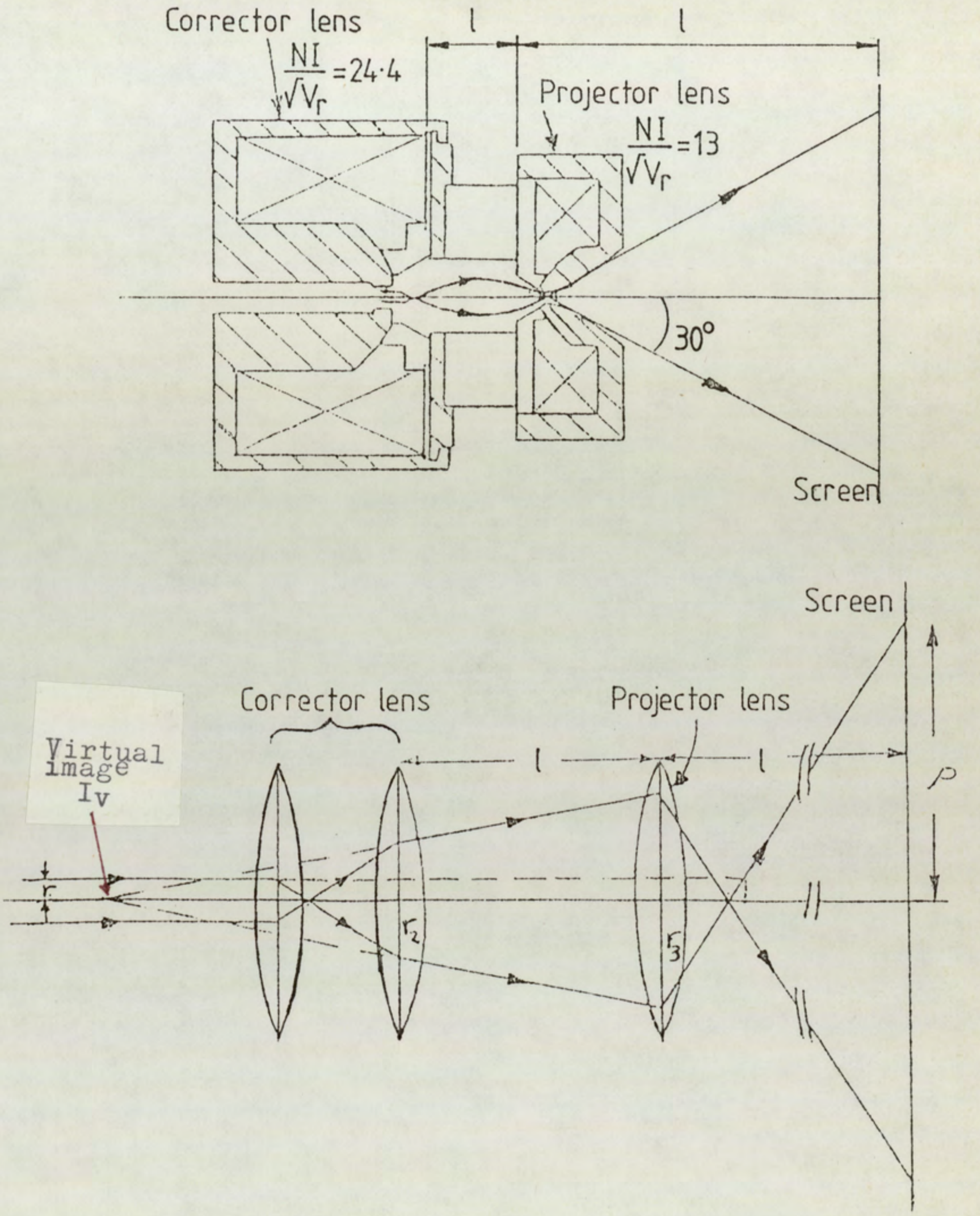

Figure 1.16: Optical analysis of Elkamali and Mulvey(1980 a,b) system.
Note.1) Virtual image I_v of variable magnification.
2) Large finite conjugates of the projector aberration.
3) Spacing L is not critical since projector magnification and hence spiral distorsion of the corrector can be adjusted to achieve correction.

whose viewing systems have been largely neglected. A special feature of the work was to develop a method for calculating the trajectories of off-axis electrons so as to be able to simulate the appearance of the final image directly without recourse to aberration theory. This is discussed in detail in Chapter Three. Such theoretical calculations were used to optimise the electron-optical design without extensive experimental work.

Chapter Two contains a critical analysis of the two-lens gap correcting system previously proposed by Hillier (1946). His design was modified so as to allow a wide projection semi-angle ($\alpha_p \simeq 30^o$) to be obtained. However, it seems that this system is inherently incapable of producing distortion free images at large projection semi-angles.

The design of a suitable wide-angle projection system constructed by the use of the computer-aided design mentioned above, is described in Chapter Four. This pre-aligned lens system was evaluated on a readily available JEOL Superscope with an accelerating voltage of 30 KV.

1.9 ELECTRON OPTICAL COMPUTATIONS

Electron optical computation of the electron microscope magnetic lens is very important, since it is desirable to optimize an electron-optical system before extensive experimental work commences. The relevant magnetic field distributions were calculated by the Munro(1975) computer program or by the improved version (Nasr 1981).

Once the lens field distribution is known, ray tracing can commence and focal properties and aberration coefficients can be deduced. The computation of the general ray path is especially useful in wide-angle image correcting systems. Finally, the computer simulation of the projected image in the electron microscope should be helpful in interpreting the experimentally observed image in the electron microscope.

1.9.1 CALCULATION OF MAGNETIC FIELD DISTRIBUTION

The improved vector potential program written by Nasr (1981) is to be preferred to that of Munro (1975) since the former requires a much smaller core store for a given accuracy it is suitable for use in a minicomputer (Nasr et. al., 1981). This, indeed, speeds up the turn round time of calculations especially when the alternative main frame computer is unavailable. The vector potential distribution and the magnetic flux density distribution throughout the lens and its surrounding for both saturated and unsaturated rotationally symmetric magnetic lenses can be calculated using the above mentioned programs.

To use either of the above programs, an accurate diagram of the unit cross section of the lens is prepared. A suitable mesh distribution is then superimposed in the z and r directions. It should be mentioned that the accuracy of the results is influenced by the chosen distribution of the meshes, and the location of the outer boundary where the vector potential is set to zero. Next the coordinates of the magnetic circuit are defined together with its permeability. Finally, the coordinates of the coil and its current density are defined; these depend on the number of ampere turns present in the defined area of the coil. These two programs differ in the handling of iron saturation. Munro's (M13) program starts from the B-H curve of the iron while Nasr's (VPSAT) program uses the B-μ curve, which seems to lead to more rapid convergence to the solution.

1.9.2 CALCULATION OF THE FOCAL PROPERTIES AND DISTORTION QUALITY FACTORS IN MAGNETIC LENSES

The design of an electron magnetic lens system does not end with the determination of its field distribution. On the contrary, the focal properties and aberration coefficient still have to be calculated, since these coefficients should be kept within tolerable limits, depending on the application in mind. The electron-optical properties of the magnetic lens, such as projector focal length and distortion coefficient D_{rd} and D_{sp} for a single lens as a function of the lens excitation $NI/\sqrt{V_r}$ can be calculated using an available program (Marai, 1977). A recently developed program (Nasr, 1981), for computing the trajectories and aberration coefficients for either a single magnetic lens or a system of magnetic lenses is superior for the present investigations. It was used extensively in designing the correcting systems described here because the aberration coefficient of the complete system can be found directly.

1.9.2.1 RAY TRACING

Accurate ray tracing is particularly important in designing the polepieces so as to permit the passage of electrons emerging from the lens at angles as large as 30°, The usual method based on the paraxial approximations (Marai, 1977) is satisfactory only when the trajectories are close to the electron optical axis. Nevertheless, the paraxial trajectory program was particularly useful during the initial stages of the design, since it gives useful preliminary guidance. It should perhaps be mentioned that, at high Gaussian semi-projection angles, e.g. 30°, paraxial trajectories deviate significantly from the real once. For such large angles, general ray calculations are needed. A program was therefore developed and will be discussed in detail in Chapter Three. This program is useful for calculating the trajectories of marginal rays. The method depends on the equations of force and acceleration, namely:

$$\underline{F} = -e(\underline{v} \times \underline{B})$$

and

$$\underline{a} = \underline{F}/m \qquad (1.12)$$

where $\underline{v}$ is the velocity of the electron and $\underline{a}$ is the acceleration.

From these equations the accelerations $\ddot{z}$ and $\ddot{r}$ and the angular velocity $\dot{\theta}$ can be found. These three values can be expressed in terms of the vector potential and its z and r derivatives as described by Goddard and Klemperer (1944). Thus

$$\ddot{z} = -\left(\frac{e}{m}\right)^2 A \frac{dA}{dZ}$$

$$\ddot{r} = -\left(\frac{e}{m}\right)^2 A \frac{dA}{dr}$$

$$\dot{\theta} = -\left(\frac{e}{m}\right) \frac{A}{r} \qquad (1.13)$$

The values of the vector potential and its derivatives can readily be found from Nasr's program (Nasr, 1981). A general ray program using the Milne formula (Milne, 1933) to obtain z, r and θ was then developed.

1.9.2.2 COMPUTED IMAGE SIMULATION

A simulation of an image observed on the final viewing screen is useful for visualizing the appearance of the image. The expected performance of the lens can then be studied without extensive experimental work. A previous program (Nasr, 1978) was based on the calculation of the coordinates of the displaced points suffering from distortion. The calculation assumes a knowledge of the object point co-ordinates, the radial extent of the image ρ at a projection distance L and the image quality factors Q_{rd} and Q_{sp}. The program calculates the co-ordinates of the displaced points of a square mesh grid for the given values of the quality factor Q. The image then is plotted using the above calculated co-ordinates. A simulated image produced in this way is shown in Figure 1.17.

The simulation, in fact, visualizes the effect of distortion on the final image. It also enables an assessment to be made of the amount of image distortion which can be tolerated in practice without being readily detected by eye. The results obtained, namely 1% of radial and 2% of spiral distortion, agree well with commonly accepted criteria.

It should perhaps be mentioned that such simulation of an image suffering from distortion holds only within the range of the validity of the third order theory. Hence, it is more convenient to use the general ray equation for determining the form of the final image directly and without recourse to the aberration theory. A new program for simulating the appearance of the final image of a square mesh grid

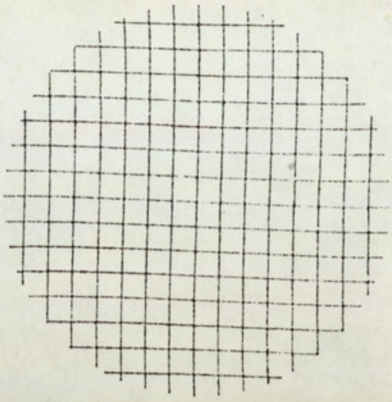

Figure 1.17: Simulated image with a maximum projection semi-angle of 28° showing the tolerable amount of distortion (2% spiral and 1% radial) is present at the image of a lens with distortion quality factor of $Q = 0.264$.

was therefore developed. The latter program uses the output of the general ray program to determine the co-ordinates of the displaced image points observed on the final viewing screen. This will be discussed in Chapter Three.

CHAPTER TWO

MINIMIZATION OF RADIAL AND SPIRAL DISTORTION USING DOUBLE GAP LENSES

2.1 GENERAL CONSIDERATIONS IN DESIGNING A DOUBLE GAP PROJECTOR LENS

The minimization of distortion in the electron microscope may well be regarded as the central problem of designing a high quality projection system. This problem has been solved in the past by using a small ($\alpha_p = 5^o$) projection semi-angle aperture leading to the necessity of a large projection distance to produce an image of the required size. Figure 2.1 illustrates the effect of using a small projection angle as indicated by the inner square ($\alpha_p = 7^o$), a typical figure for commercial electron microscopes. Since electron lenses are analogous to optical lenses, principles of geometrical optics may be applied directly to electron optics. Since it is possible to minimize the distortion of an optical system by the appropriate combination of simple lenses, the method can also be used in electron optics.

A method of correcting radial distortion in electron optics was originally proposed and realised by Hillier (1946). In Hillier's arrangement, two lens gaps were energized in series by a single coil. Here the rays from the first lens pass through the centre of the second lens (as shown in Figure 2.2); its refractive

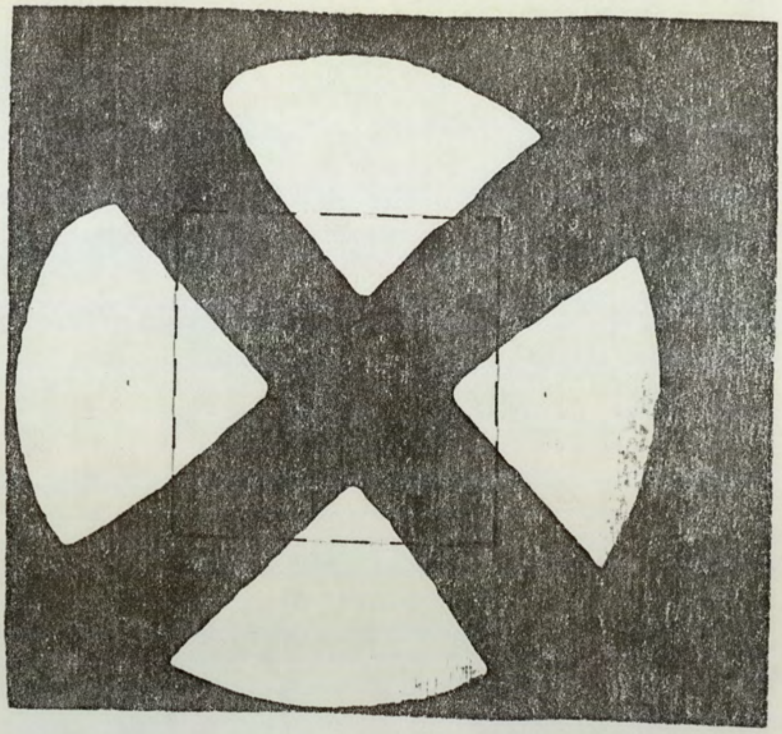

Figure 2.1: Complete image on the viewing screen of the JEOL Superscope obtained by external photography ($\alpha_p = 14^{o}$). The inner square shows the area photographed by the internal camera ($\alpha_p = 7^{o}$).

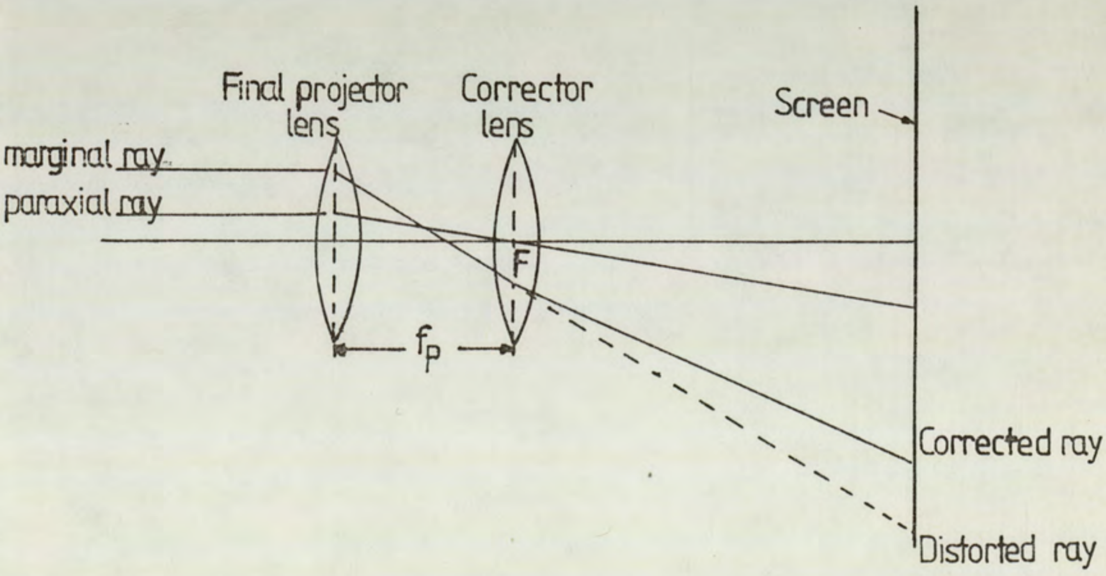

Figure 2.2: Schematic diagram showing Hillier's arrangement for correcting radial distortion. A corrector lens is placed in the back focal plane F of the projector.

power is thus zero. Nevertheless, the second lens serves a useful function in correcting radial distortion since marginal rays from the first lens will not, in general, pass through the paraxial focal point. Such rays will be bent back towards the lens axis in such a way that the radial distortion at the final screen is zero. However, energizing the two lens gaps in series meant that although the radial distortion was corrected, spiral distortion was increased. It is useful here to mention the fact that the spiral distortion coefficient changes sign if the polarity of the magnetic field is reversed by reversing, e.g. the lens current in the coil. Therefore, it is to be expected that the spiral distortion can be corrected by the combination of two lenses with opposite polarities, in other words, with zero combined excitation. Recently, a resurgence of interest has occured in this arrangement devised by Hillier (1946). This is mainly because Hillier's single coil arrangement precluded the possibility of reversing the current in one of the lenses to make a compensation of the spiral distoration. The design of a "doublet" rotation-free system by JUMA and Mulvey (1978), is a recent reversion to the above idea. Some idea of the possibilities of this design for the correction of spiral distortion can be gained from an approximate analysis based on the square-top field.

2.2 THEORETICAL CALCULATION BASED ON SQUARE TOP FIELD MODEL

The square-top magnetic field distribution is the simplest starting point for an analysis of the problem. The paraxial ray equation is readily solved for a ray passing through the square-top field.

Consider the field distributions shown in Figure 2.3. We may consider it as two identical field distribution of length S/2 placed back to back. When reversing the current in the second half of the field distribution (Figure 2.3), the electron trajectories are not affected. Hence, a mathematical approach can be adopted for the correction of spiral distortion in a rotation-free system.

The trajectory of the electron is the solution of the paraxial ray equation

$$\frac{d^2r}{dZ^2} + \frac{e}{8m} \frac{B^2(z)}{V_r} r = 0 \qquad (2.1)$$

If the initial ray height is r_o with initial slope r'_o, then

$$r = r_o \cos KZ + \frac{r'_o}{K} \sin KZ \qquad (2.2)$$

$$r' = r'_o \cos KZ - K r_o \sin KZ \qquad (2.3)$$

where $K^2 = \frac{e}{8m} \frac{B^2(Z)}{V_r}$ and $K = \frac{\theta}{S}$, Z is the axial distance,

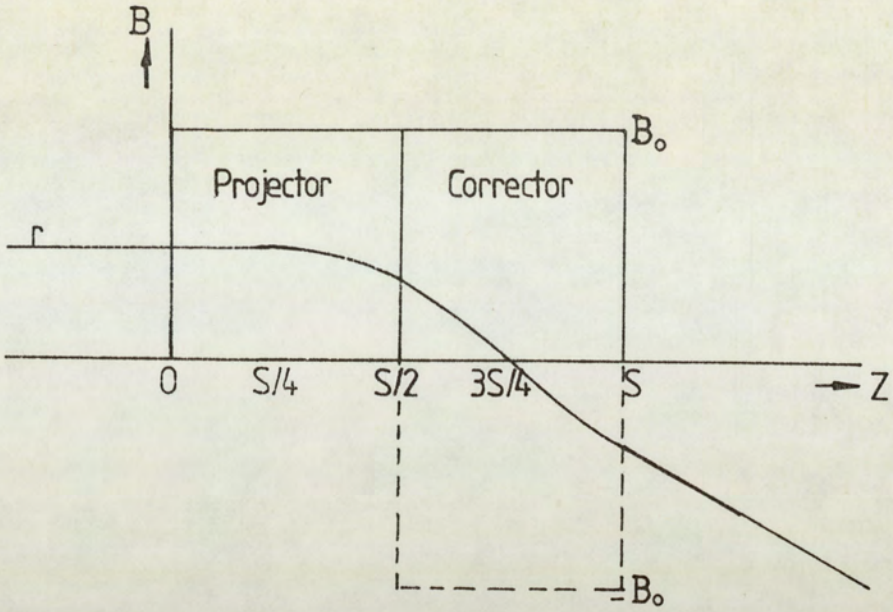

Figure 2.3: Square top field model of the projection system with the refracting power of the second lens equal to zero. The dotted field shows the reversing of the second lens-gap current to compensate the image rotation of the first lens-gap to reduce the spiral distortion.

θ is the total rotational angle in the additive mode which will be zero in the opposition mode and S is the field width of the two lenses.

A ray of height 1 and slope 0 is assumed to pass through the projection field shown in Figure 2.3 passing through the centre of the second lens and hence

$$r_{(\text{at } \frac{3}{4} S)} = 0 \qquad (2.4)$$

since the refractive power of the second half of the field is zero, the final slope of the ray is not affected by the second half of the field. Hence

$$r'_{(\text{at } S/2)} = r'_{(\text{at } S)} \qquad (2.5)$$

Applying the initial conditions and equation 2.4

in equation 2.2 gives

$$\cos \tfrac{3}{4} KS = 0 \text{ and this leads to } \theta = 2\pi/_3 \qquad (2.6)$$

Marai et. al. (1977) expressed the distortion of a square top field model of a single lens as

$$D_{sp} S^2 = \frac{\theta^3}{2} + \frac{\theta^2}{8} \sin 2\theta \qquad (2.7)$$

where D_{sp} is the coefficient of spiral distortion assuming the ray entering the field parallel to the axis of the lens. Substituting the value of θ evaluated above in equation 2.7 gives

$$D_{sp} S^2 = 4.12$$

The focal length of a magnetic lens of a square top field model is given by

$$\frac{S}{f} = \theta \sin \theta$$

Using the same value of θ evaluated in equation 2.6, gives

$$\frac{f}{S} = .5513$$

The image quality factor (Marai and Mulvey, 1977) is given by

$$Q_{sp} = \sqrt{D} \ f$$

$Q_{sp} = 1.119$ for the total field.

Since the image distortion $\frac{\Delta\rho}{\rho}$ is proportional to Q^2_{sp} (i.e. $\Delta\rho/\rho = Q^2_{sp} \tan^2\alpha_p$) then

$\Delta\rho/\rho = 1.25 \tan^2\alpha_p$

Remembering that the total field consists of two identical square top fields of width S/2 (i.e. each causing a rotation $\theta = \pi/3$). Accordingly $D_{sp} S^2$ for the first square top field can be calculated by substituting $\theta = \pi/3$.

$$\text{Hence } D_{sp} (S/2)^2 = \frac{(\pi/3)^3}{2} + \frac{(\pi/3)^2}{8} \sin 2 (\pi/3)$$

$$= .6928$$

$$\text{i.e. } D_{sp} S^2 = 2.7712$$

Remembering that the refracting power of the second lens is zero, then the focal length of the first square top field is the same as that of the total field, i.e. f/S for the first square top field = 0.5513. Thus $Q^2_{sp} \tan^2\alpha_p$ for the first square top field = $0.842 \tan^2\alpha_p$ and $Q^2_{sp} \tan^2\alpha_p$ for the second square top field = $0.410 \tan^2\alpha_p$.

Thus the spiral distortion produced in the image by the seconed (conector lens) is only half that produced by the projector lens. Reversing the current in the corrector (as indicated by the dotted part of the field distribution of figure 2.3) will therefore not correct the image distribution completly but only reduce it by a factor of two.

2.3 EXPERIMENTAL APPROACH TO THE MINIMIZATION OF DISTORTION

The idea was to use two identical lenses. The centre of the second lens is positioned at the focal point of the first. The current in the second lens is opposed to the current in the first lens. Figure 2.4

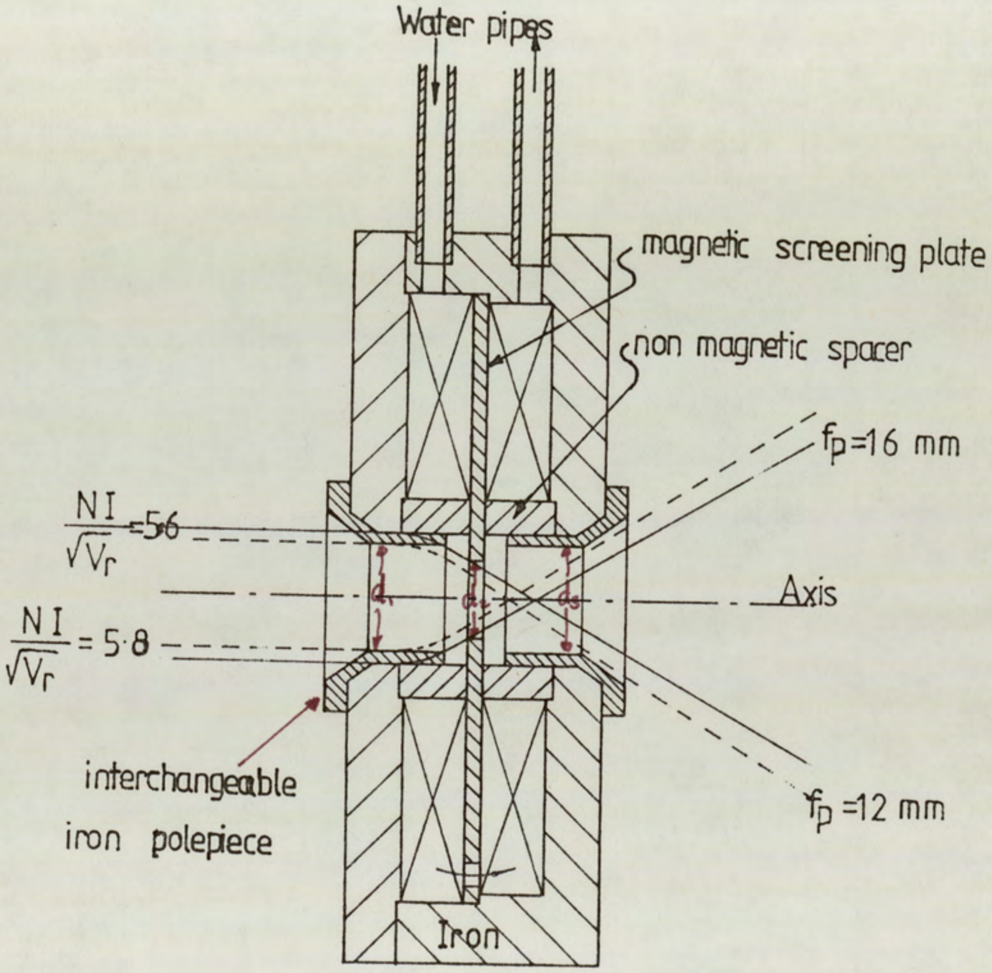

Figure 2.4: Cross-section of the rotation-free doublet. bore of screening plate 10mm. lens bore without polepieces 17mm. lens bore with polepieces 14mm.
paraxial trajectory without polepieces (solid line) for $NI/V_r^{\frac{1}{2}} = 5.6$
paraxial trajectory with polepieces (dashed line) for $NI/V_r^{\frac{1}{2}} = 5.8$

illustrates the design of the doublet lens system. The bores of the doublet was made quite large to allow rays of wide angle to pass through. The paraxial

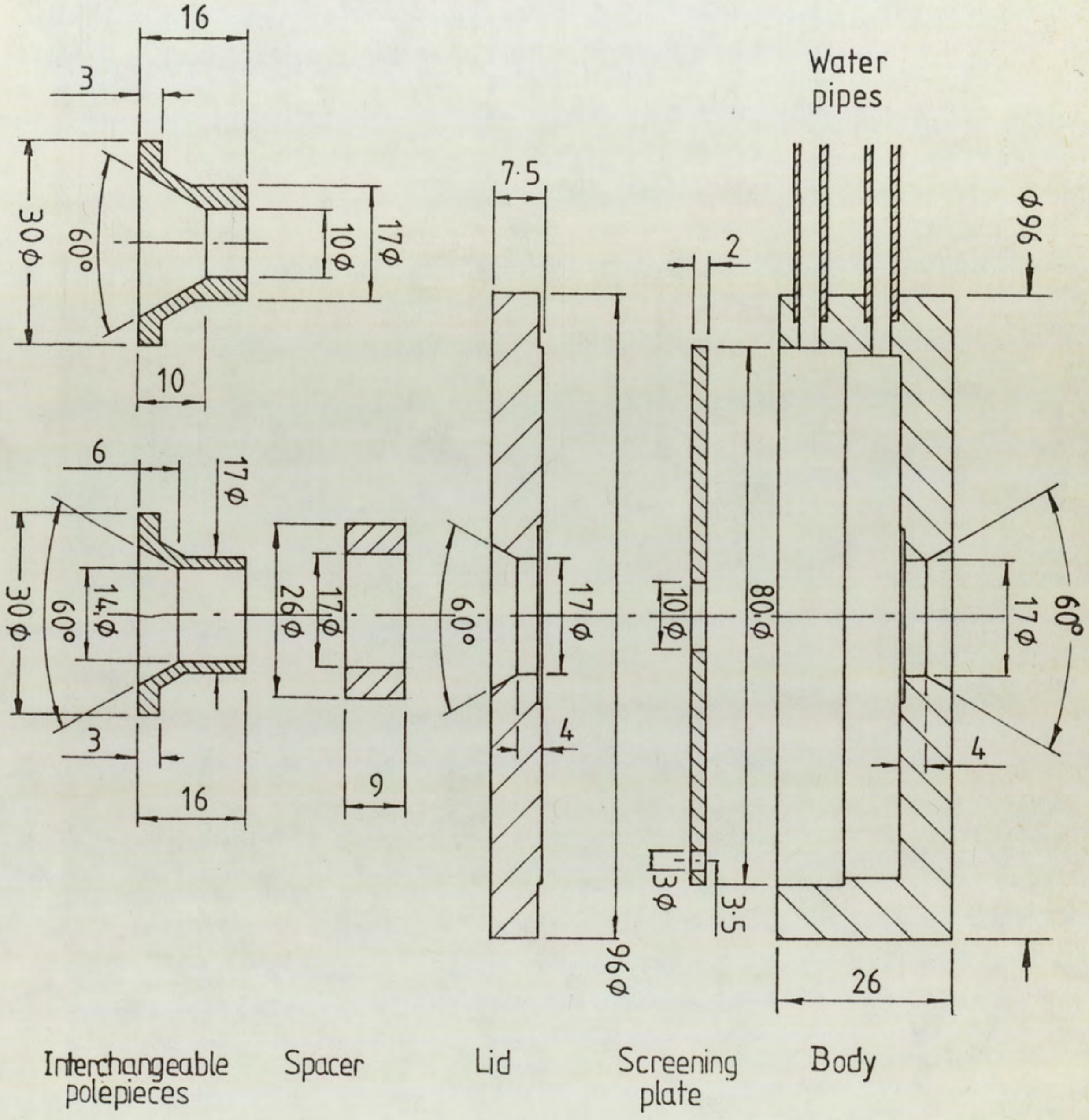

Figure 2.5: Cross section of the doublet showing the three main parts of the design besides the different replacable polepieces used. Note that the spacer is non magnetic material (all dimensions are in mm).

trajectory computation was used in the preparatory design stage. The bore diameter ratio was 17:10:17 mm for $d_1 : d_2 : d_3$; respectively. The lens was constructed in three parts; the body, the middle plate and the lid, as shown in Figure 2.5. An extra polepiece was made to allow the bore diameter to be changed thereby changing the shape of the resulting field distribution (Figure 2.6). Each of the two coils has 250 turns of 24 SWG copper wire. The resistance of the coil was 2.8Ω. The two lenses could be excited in two ways. The first is when both lenses are in the cooperative mode, i.e. $NI_1 = NI_2$, where NI is the lens excitation. The second mode of operation is when their excitations are in opposition, i.e. $NI_1 = -NI_2$. It was also used with unequal excitations. Figure 2.7 shows the field distribution in both modes of operation as measured experimentally.

The Gaussian trajectory passing through the twin lens system, shown in Figure 2.4, indicates that a ray height of 8.5mm will give a wide semi-angle ($\alpha_p = 30^\circ$) when each lens is excited with $NI/\sqrt{V_r} = 5.6$. The corresponding focal length of the twin system is 16mm. A polepiece was then inserted to make the bore ratio $d_1:d_2:d_3$ equal to 14:10:14 mm. This new arrangement, according to the Gaussian trajectories, results in a shorter focal length (12mm) as shown in Figure 2.4. The system was tested in a JEOL Superscope. Figure 2.8 shows the electron optical column of the JEOL Superscope with the twin lens system in place.

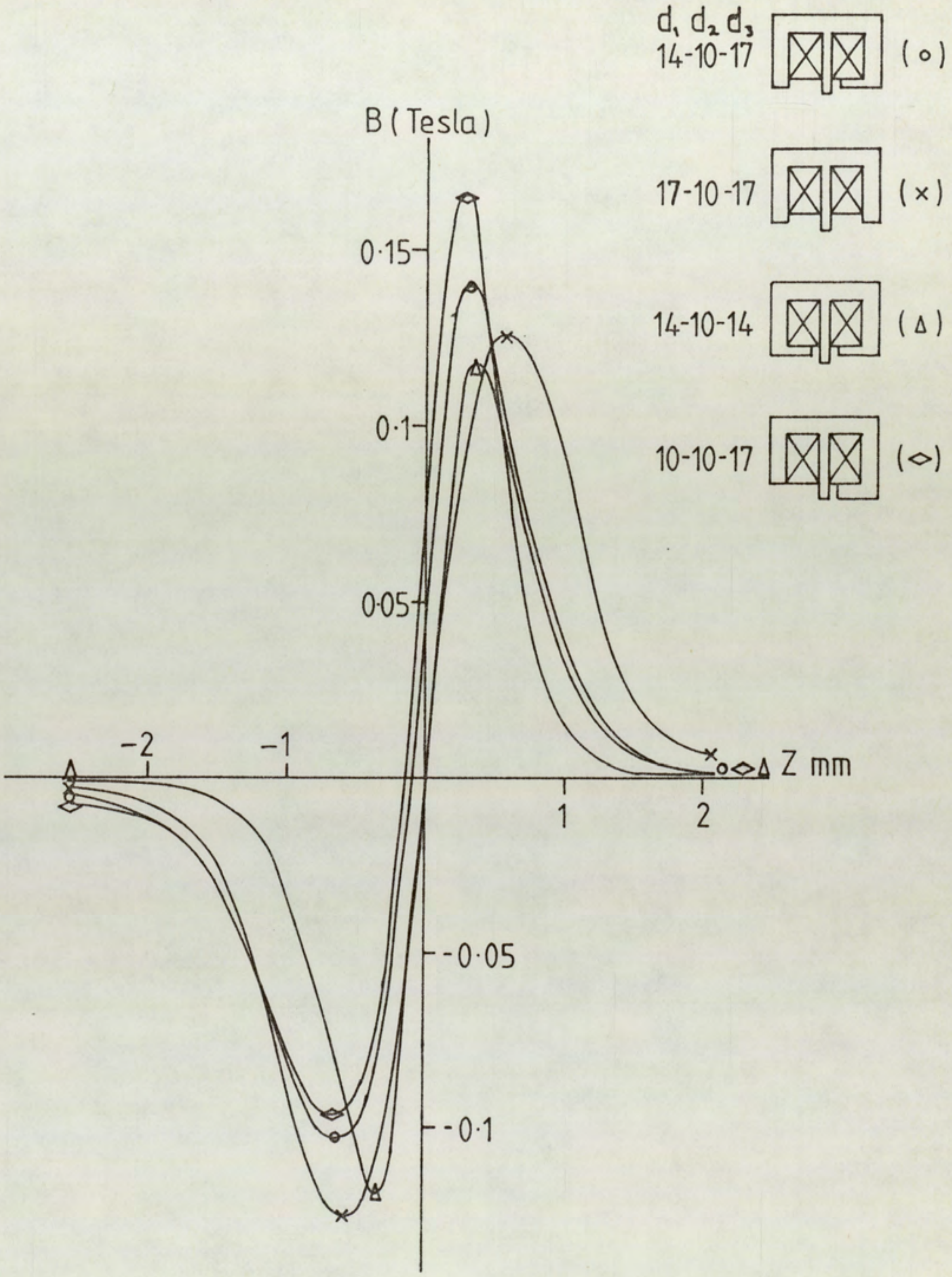

Figure 2.6: Axial field distribution of the doublet showing the effect of changing polepiece diameter. Each lens was excited with NI = 1620 A.t.

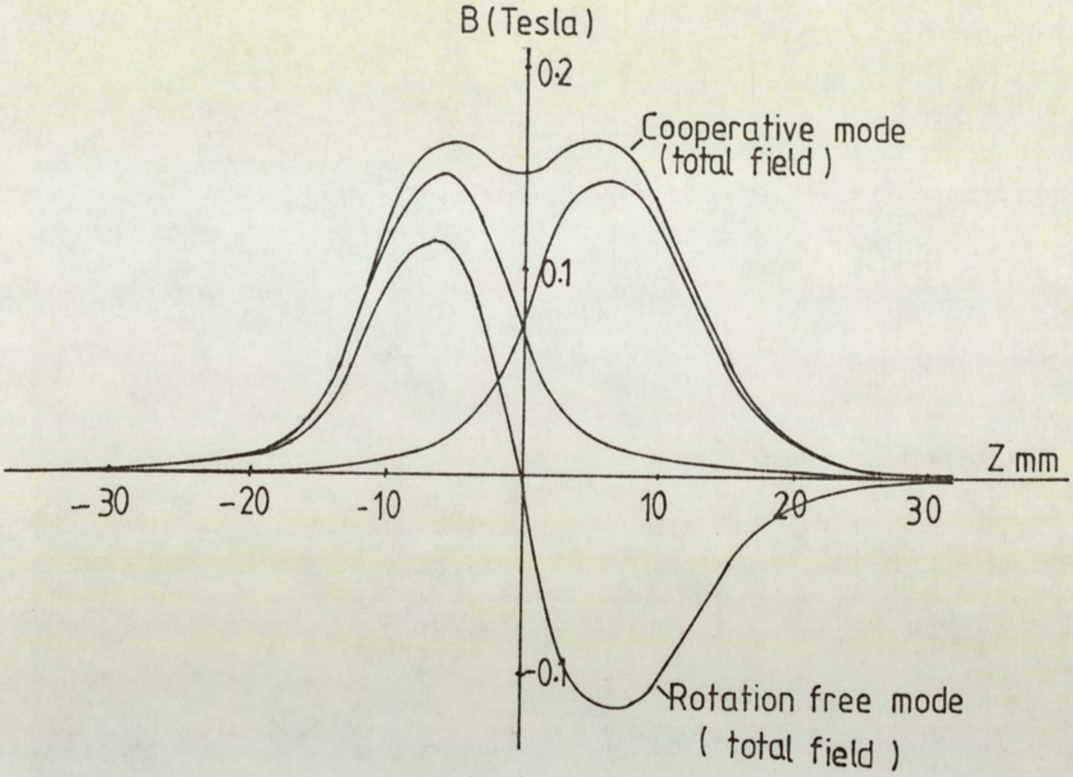

Figure 2.7: Experimentally measured axial field distribution of the doublet with each lens excited with NI = 1620 A.t. Here the two modes of operation are shown.

The doublet is held in position by the water pipes through which the electrical connections to the coils are led. The outside diameter of the doublet was 96mm. The supporting plate shown in Figure 2.9 was used instead of the lid of the internal camera of the Superscope. Extensive experimental investigation showed that either radial or spiral distortion could be corrected. The system was tested as well with a replacable polepiece of different diameter as indicated in Figure 2.6, where the field distribution is shown. In this case, a slight improvement was noticed in which tolerable distortion could be obtained within a semi-angle of about 10°. However, this correcting system,

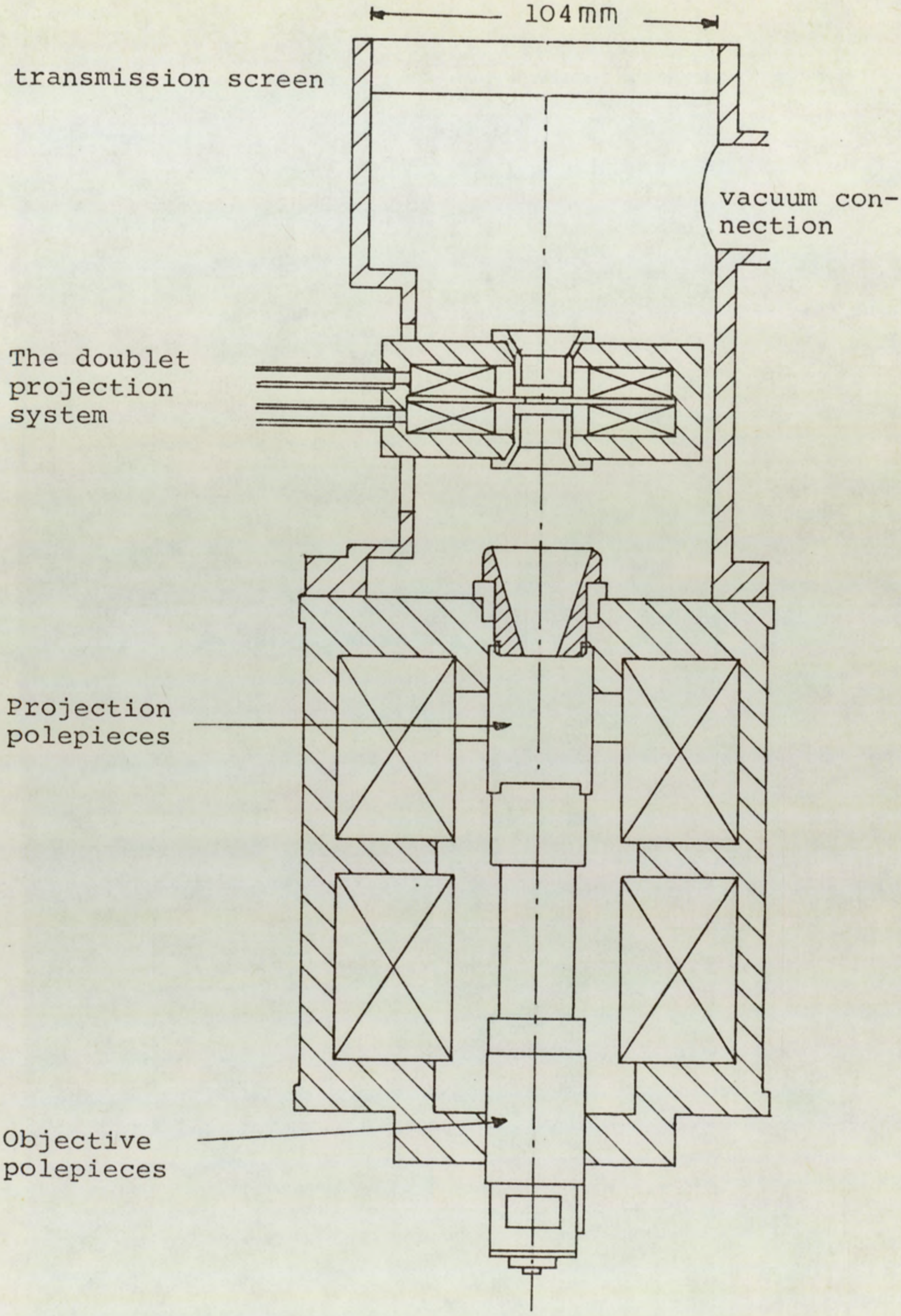

Figure 2.8 : The electron optical column of the JEOL Superscope with the doublet fitted in place of the internal camera.

in fact, does not justify the cost of the power used in energizing the corrector lens, since the second lens power is more or less wasted (i.e. it does not contribute to the total magnification). A well designed single polepiece lens could do as well as this, or maybe better, at the tolerable limit of 2% spiral distortion and 1% radial distortion. The same remarks also apply to the design of the asymmetrical triple polepiece lens produced by Tsuno et. al. (1980) and Tsuno and Harada (1981), who achieved a simultaneous correction, but the projection semi-angle was only 7°.

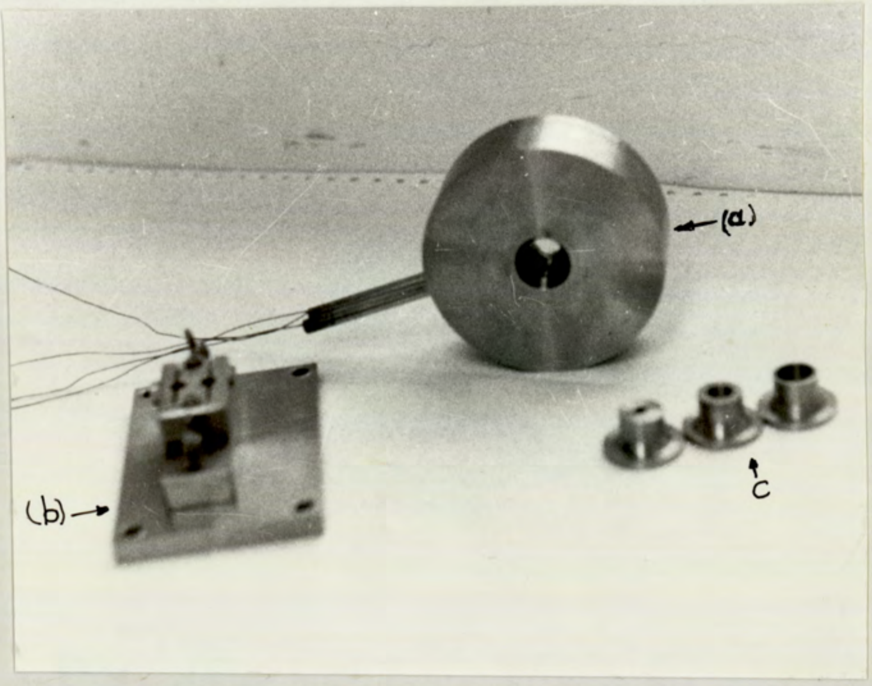

Figure 2.9: Photograph of the experimental doublet (a) projector lens showing the supporting (b) plate and various interchangable polepieces (c) .

Figure 2.10 shows the experimental results. These photographs indicate that there is a limiting angle of projection for a single projector lens and for the system as a whole. The other idea which will be discussed in the next chapter is the folding over of the off-axis rays and hence the appearance of a double image as illustrated in Figure 2.10b. In this figure the rays appearing to fold back towards the axis are in fact projection images of the outer extremities of the cross-wires suffering from severe barrel distortion and spiral distortion. In Chapter Three the image of such a cross-wire has been simulated in a computer (Figure 3.12) showing more clearly the role of the combined high order radial and spiral distortion.

The appearance of such images indicated the need for a computer program to trace marginal rays directly.

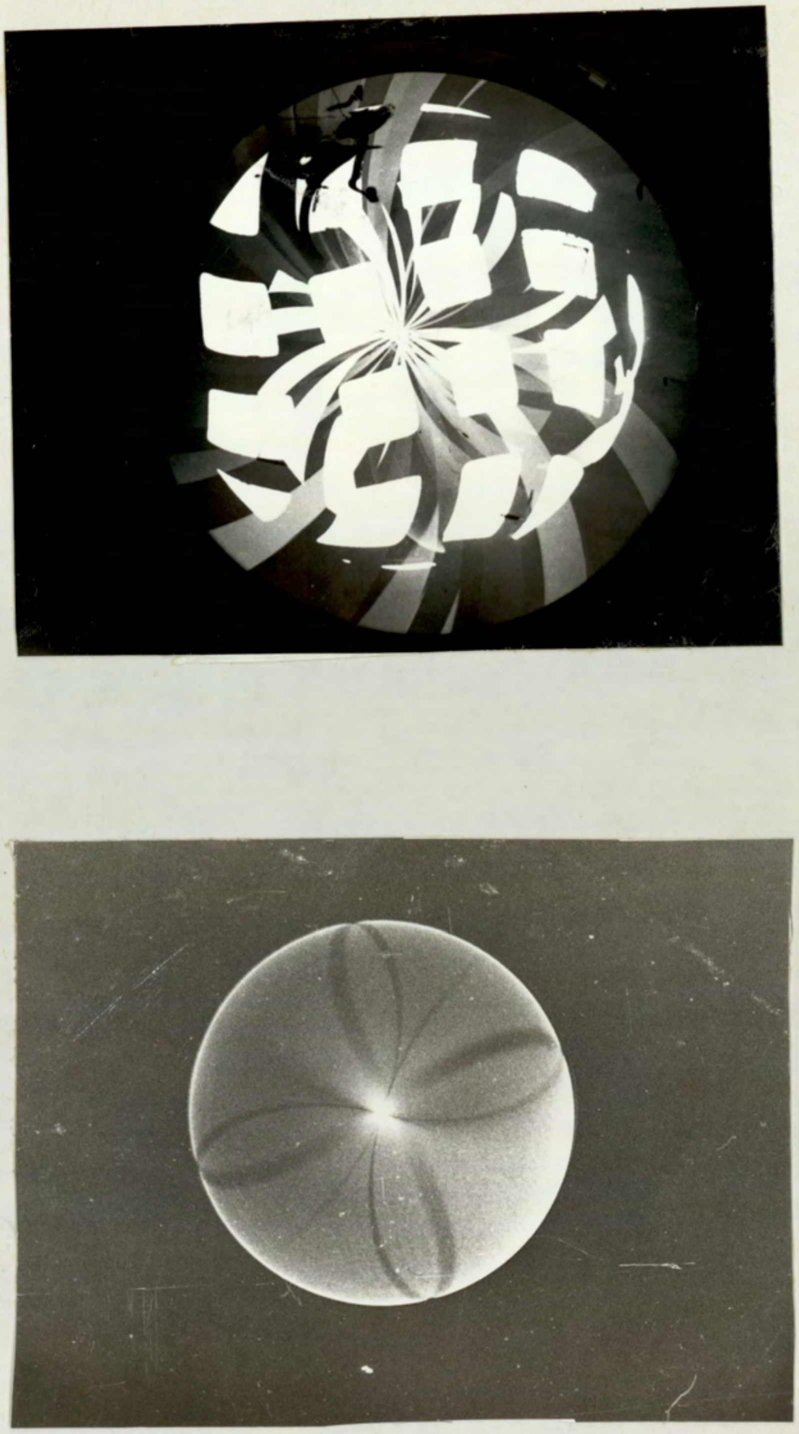

Figure 2.10: External photography of images on the transmission screen of the JEOL Superscope produced by the doublet lens (a) the second is excited only with $NI/\sqrt{V_r} = 16.4$ showing the limiting projection angle of the lens besides the start of streaks appearing. (b) A cross wire is used here, this image confirms the limiting projection angle for the system of lenses as well as folding over of the marginal rays towards the centre of the image.

CHAPTER THREE

NUMERICAL RAY TRACING

3.1 INTRODUCTION

In the study of the electron properties of magnetic lenses, the tendency has been to use an analytical treatment for third order aberrations based on the paraxial ray equation. The limitation in adopting such an approach is that beams of large semi-projection angle cannot be treated adequately.

This chapter is concerned with the calculation of non-paraxial rays by means of the general ray equation. The calculation here is confined to the rays passing through a purely magnetic field of axial symmetry, although the method can be extended to ray tracing in electrostatic systems as well.

3.2 THE EQUATION OF MOTION

The total force $\underline{F}$ acting on an electron of charge $q = -e$ travelling in a combination of an electrostatic and magnetic field is given by

$$\underline{F} = -e\ (\underline{E} + \underline{v} \times \underline{B})$$

where $\underline{E}$ is the electric field strength, $\underline{v}$ is the velocity of the electron and $\underline{B}$ is the magnetic field strength.

The vector equation 3.1 can be resolved into three scalar equations in any orthogonal coordinate system. The path of the electron can then be calculated by integrating these scalar equations.

Consider the special case of tracing the electron in a purely magnetic field. The equation of force will reduce to the form:

$$\underline{F}_m = -e\ (\underline{v} \times \underline{B})$$

Since the acceleration $\underline{a}$ is given by

$$\underline{a} = \underline{F}/m$$

Then the equation of motion will be represented as

$$\underline{a} = \left(\frac{-e}{m}\right)\ (\underline{v} \times \underline{B}) \qquad (3.2)$$

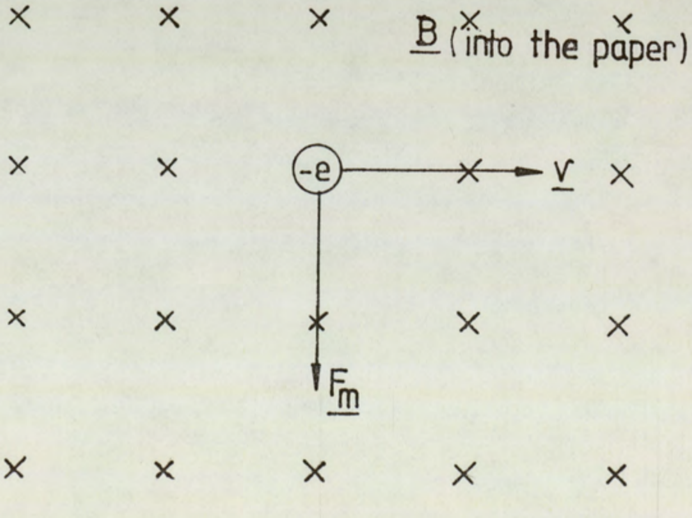

Figure 3.1: The force on an electron moving towards the right through a magnetic field perpendicular to the plane of the paper is downward.

This shows that in a magnetic field, the electron is accelerated in a perpendicular direction both to the field vector and to its velocity. So it is easier to understand the motion of the electron in a magnetic field by considering the two-dimensional motion in two separate planes.

The convenient planes are:

The 'Equatorial' plane at right angles to the axis of axial symmetry, moving with the longitudinal velocity v_Z of the electron.

The 'Meridional' plane rotating with the electron about the axis of the system.

In cylindrical coordinates (r,z,θ), taking into account the axial symmetry of the field, the vector equation takes the simple form of the three scalar equations as given by Goddard et. al. (Goddard and Klemperer, 1944).

$$\ddot{z} = -\left(\frac{e}{m}\right)^2 A \frac{dA}{dZ}$$

$$\ddot{r} = -\left(\frac{e}{m}\right)^2 A \frac{dA}{dr} \qquad (3.3)$$

$$\dot{\theta} = -\frac{e}{m}\frac{A}{r}$$

where $\ddot{z}$ is the acceleration in the z-axis direction, and $\underline{A}$ is the magnetic vector potential so that:

$$\underline{B} = \text{curl } \underline{A}$$

In carrying out the calculations, the relevant magnetic vector potential A were evaluated by the VPSAT (Nasr,1981) program mentioned in chapter I. These values were stored in the computer and used as an input to the general ray calculations.

3.3 GENERAL RAY CALCULATION

The set of equations (3.3) are second order differential equations in which the first order derivatives $\dot{z},\dot{r}$ do not appear. These may be integrated numerically using the numerical integration formula due to Milne (1933).

$$Z_{n+1} = Z_n + Z_{n-2} - Z_{n-3} + \frac{\Delta t^2}{4}(5\,\ddot{Z}_n + 2\,\ddot{Z}_{n-1} + 5\,\ddot{Z}_{n-2})$$

$$r_{n+1} = r_n + r_{n-2} - r_{n-3} + \frac{\Delta t^2}{4}(5\,\ddot{r}_n + 2\,\ddot{r}_{n-1} + 5\,\ddot{r}_{n-2}) \qquad (3.4)$$

The values of $\ddot{Z}$, $\ddot{r}$, etc. are taken from equation (3.3) which in turn needs the calculation of $\frac{dA}{dr}$ and $\frac{dA}{dZ}$. This was calculated making the assumption of the variation of the vector potential A over each quadrilateral given by Nasr (1981).

$$A = f + gZ + hr + iZr \qquad (3.5)$$

where f, g, h, i are constant over each quadrilateral. Differentiating equation (3.5) with respect to Z gives the value of $\frac{dA}{dZ}$ and, with respect to r, gives $\frac{dA}{dr}$.

$$\frac{dA}{dZ} = g + ir \qquad (3.6)$$

$$\frac{dA}{dr} = h + iZ \qquad (3.7)$$

The values of f, g, h, and i were found by solving the four simultaneous equations produced by the substitution of the values of A, Z, and r at each node of the quadrilateral in equation (3.5).

Three lattices were constructed accordingly, i.e. $\ddot{z}$, $\ddot{r}$ and $\dot{\theta}$ lattices. These were computed at each node of the defined mesh in the vector potential calculating program.

Since the energy equation is given by:

$$\frac{1}{2} mv^2 = e V_r \qquad (3.8)$$

where v is the velocity of the electron corresponding to the relativistically corrected accelerating voltage V_r where:

$$V_r = V(1 + 10^{-6}V) \qquad (3.9)$$

Accordingly, the velocity of the electron will be :

$$v = \sqrt{2 \frac{e}{m} V_r}$$

assuming that the electron is moving initially in an axial plane ($\dot{\theta}_o = 0$).

The initial velocity components $\dot{z}_o$ and $\dot{r}_o$ can be calculated if the electron is projected from a point on the axis with an inclination angle γ, by using $\dot{z}_o$ = v cos γ and $\dot{r}_o = v \sin \gamma$. If the electron is assumed to be parallel to the axis, then $\dot{z}_o = v$ and $\dot{r}_o = 0$.

The four initial values (Z_{n-3}, Z_{n-2}, Z_{n-1} and Z_n) needed in equation (3.4) are obtained by choosing a sufficiently small time interval t and applying the laws of uniform motion:

$$\dot{Z}_{n+1} \simeq \dot{Z}_n + t\,\ddot{Z}_n$$

$$Z_{n+1} \simeq Z_n + t\,\dot{Z}_n + \frac{1}{2} t^2\,\ddot{Z}_n \qquad (3.10)$$

Similarily, $\dot{r}_n+1$ and r_{n+1} can be found by using the laws of uniform motion applying the above equations of Z by changing each Z into r.

The electron can now be traced using a step by step method with the use of equation (3.4); results were tabulated at the end of each step.

This method is sufficiently accurate since there is a ready means of estimating and controlling the accuracy. One of these checks is to calculate the energy, W, of the electron which should be constant in view of the energy equation given by:

$$W = \dot{r}^2 + \dot{z}^2 + r^2\dot{\theta}^2 \qquad (3.11)$$

Thus, a direct measure of the accuracy of the path is available at each step. However, if the energy value at any step varies significantly, that would affect the end result. It is then advisable either to shorten the time interval or to use a more accurate formula such as that given by Milne (1933).

$$Z_{n+1} = Z_n + Z_{n-4} - Z_{n-5} + \frac{t^2}{48}(67\ddot{Z}_n - 8\ddot{Z}_{n-1} + 122\ddot{Z}_{n-2} - 8\ddot{Z}_{n-3} + 67\ddot{Z}_{n-4})$$

$$r_{n+1} = r_n + r_{n-4} - r_{n-5} + \frac{t^2}{48}(67\ddot{r}_n - 8\ddot{r}_{n-1} + 122\ddot{r}_{n-2} - 8\ddot{r}_{n-3} + 67\ddot{r}_{n-4}) \tag{3.12}$$

These formulas actually need six initial points to be evaluated as mentioned before by using equation (3.10).

3.4 RAY TRACING THROUGH A HOMOGENEOUS MAGNETIC FIELD

The homogeneous magnetic field is defined as that in which $B(Z) = B_o$ where B_o is constant over a distance $Z = S$ which limits the field (figure 3.2).

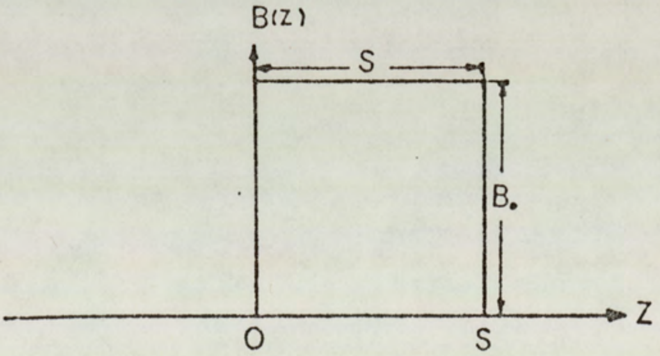

Figure 3.2: The square top field of half width S and constant height B_o

Although the homogeneous magnetic field can never exist in practice, it can be accepted as an approximation for a very long solenoid assuming an abrupt start and termination of the field at the entrance and exit of the coil, respectively.

As mentioned in the previous section the vector potential A has to be obtained first. Applying Stoke's equation:

$$\int_{\mathcal{S}} \underline{B}.d\underline{a} = \oint_C \underline{A}.d\underline{s} \qquad (3.13)$$

where $\underline{B}$ = Curl $\underline{A}$. This shows that, for a closed curve C that bounds a surface $\mathcal{S}$, the integral taken over the scalar product of B and the surface element da equals the line integral taken over the vector potential times the line elements ds which form the boundary enclosing the surface $\mathcal{S}$. Applying equation (3.13) over a disc of radius r_o hence set area πr_o^2 set normal to the axial component of the flux density B_Z, the closed curve that bounds the disc has a line length of $2\pi r_o$.

Since the magnetic field B_Z of the homogeneous field is constant, then:

$$2\pi r_o \ A = 2\pi \ B_Z \int_o^{r_o} r dr$$

hence the vector potential A is given by:

$$A = \frac{B_Z r}{2} \qquad (3.14)$$

The derivatives of the vector potential A with respect to Z and r take the form:

$$\frac{dA}{dr} = \frac{B_Z}{2}, \qquad \frac{dA}{dZ} = 0$$

Substituting the value of these derivaties in equation (3.3) for an electron initially in an axial plane gives:

$$\ddot{Z} = 0$$

$$\ddot{r} = -\left(\frac{e}{m}\right)^2 \frac{B_Z^{\,2}}{4}$$

$$\dot{\theta} = -\left(\frac{e}{m}\right) \frac{B_Z}{2}$$

These results were used by Hindy (1980) to trace the trajectory of an electron projected in a meridional plane from a point on the axis at distance d from a chosen point O at a different angle γ to the axis.

Figure 3.3 shows the tracing of a 100 kev electron travelling through a magnetic field B = .02 Tesla. This was computed using a program written for the mini-computer PET. This program was developed to trace a ray through a known magnetic field (Hindy, I.K. 1980) with the aid of the mini-computer. Figure 3.4 demonstrates the tracing of the same electron in the equatorial plane.

These calculations depend on the analysis of the square-top field distribution, hence it does not apply in practice for the practical field distribution of the wide angle projection system. A general program has therefore been developed which will be discussed in the next section.

3.5 COMPUTER PROGRAM TRAJ FOR TRACING A RAY THROUGH A MAGNETIC LENS

A computer program TRAJ for numerical ray tracing based on the general equation of motion has recently been developed making use of both VPSAT program (Nasr, H. 1981) for getting the vector potential values and the basic program produced by Hindy (1980). A block diagram of this program (TRAJ) is shown in figure 3.5.

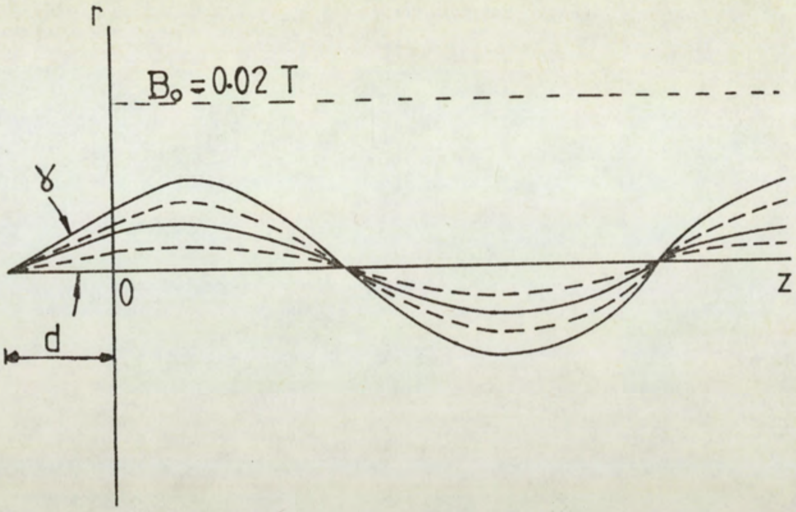

Figure 3.3: Calculated electron trajectories in the meridional plane of a square top field beginning at O. Initial energy is 100 kev. Four electrons are shown with inclination angle γ = 2°,5°,7° and 10° to the axis respectively. (Hindy, I.K. 1981)

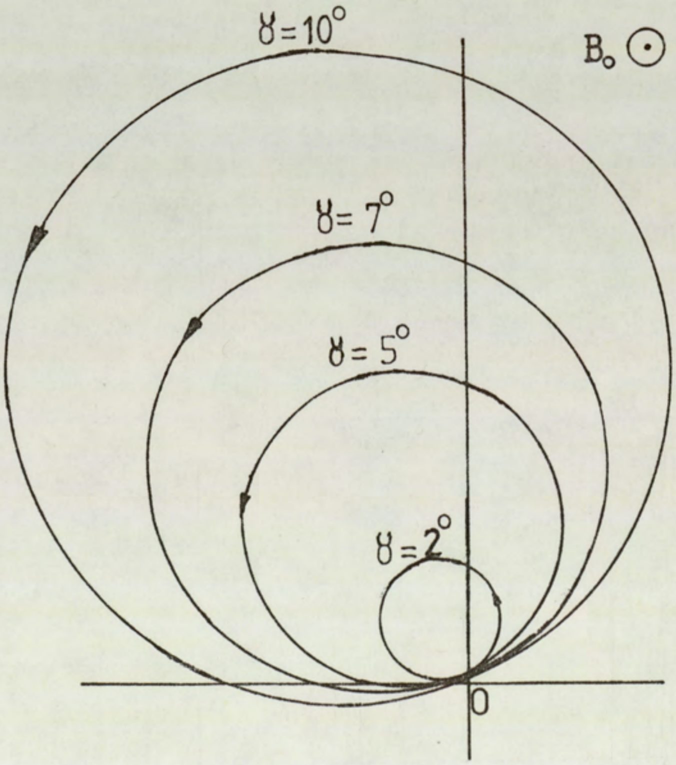

Figure 3.4: Corresponding electron trajectories in the equatorial plane for the 100 kev electrons shown in figure 3.3.

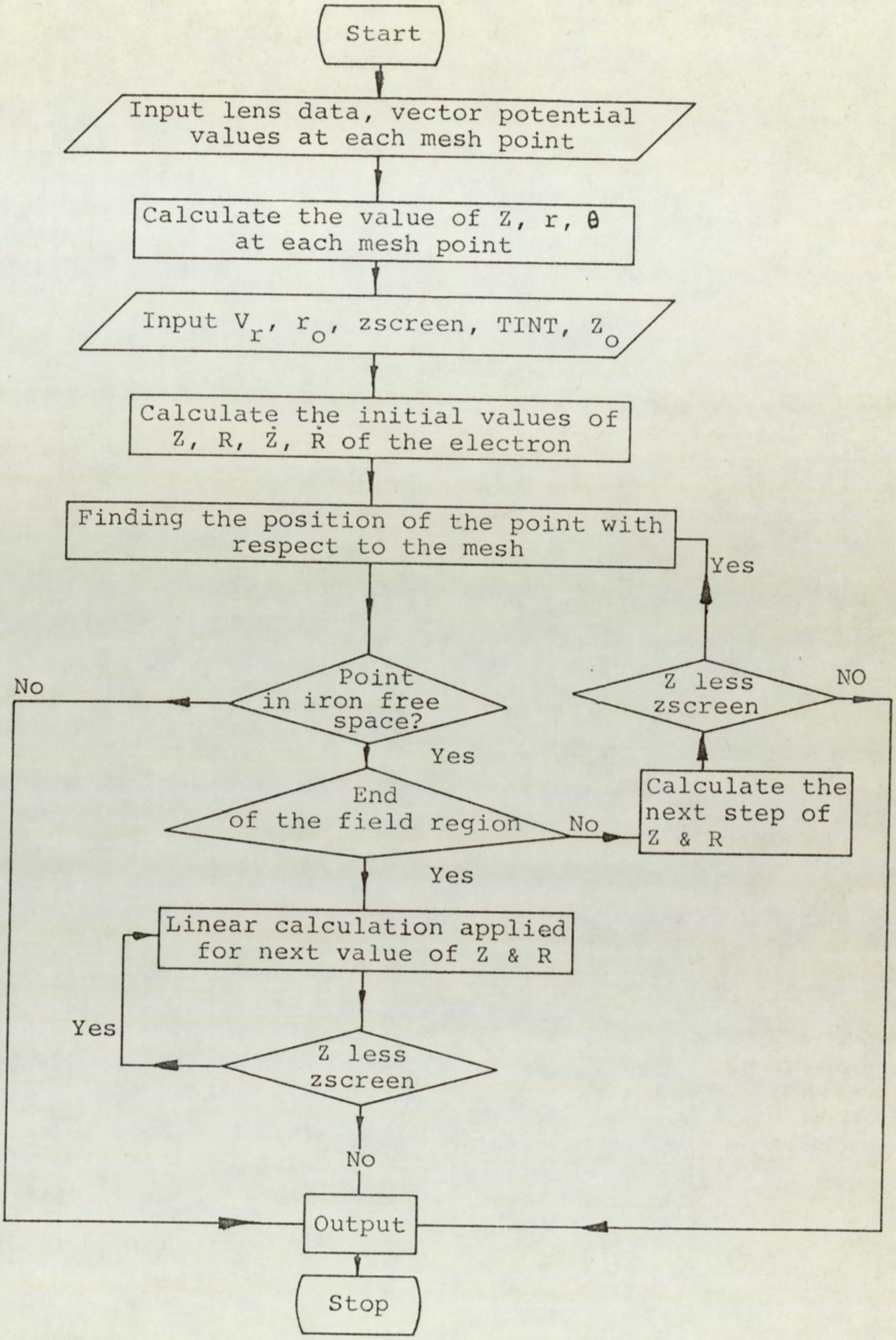

Figure 3.5: Block diagram of the general ray program TRAJ.

3.6 PREPARATION OF DATA

The data of the TRAJ program consists of the axial co-ordinates of the major mesh lines, the radial co-ordinate of the major mesh lines, the magnetic circuit specification, coil current specifications and some initial conditions needed in the programs. These initial conditions are the relativistically corrected accelerating voltage, (V_r), and the height of the ray at

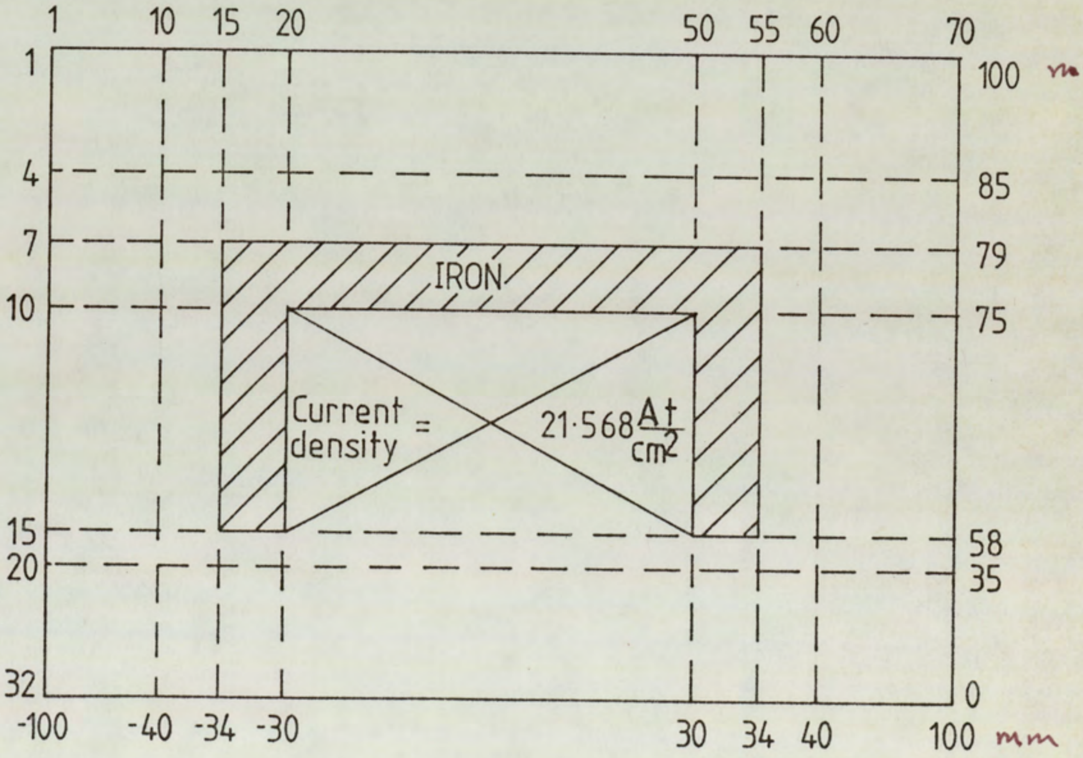

Figure 3.6: The test lens used by Goddard et. al. (1946). The iron shield has an inner and outer radius of 58 and 75 mm respectively. Shield thickness 4 mm. The main meshes employed in the present computation are inserted.

the start of the boundary of the mesh (r_o), i.e. at the start of the magnetic field. The screen distance from the lens is needed as well (zscreen), besides the time interval chosen for each step of the calculation (TINT). Finally, the point from which the calculation start, Z_o.

As an example of such data used as an input to the program to show its performance and uses, the data of a test lens shown in figure 3.6 which was previously published by Goddard and Klemperer (1944) is shown in figure 3.7.

3.7 APPLICATION OF THE PROGRAM TO RAY TRACING IN ELECTRON LENSES

The computer program TRAJ was applied to the tracing of pencils of rays in a single magnetic lens and also in a system of magnetic lenses. As a check on the program it was used to re-calculate the tracing of the rays travelling in the test lens mentioned in section 3.6.

The axial components of flux density B(Z,r) against the axial Z - coordinate along lines parallel to the axis and at various distances from it, were computed as shown in figure 3.8.

These were calculated using the VPSAT program from which the value of the vector potential was recorded in a file in the computer to be used as an input to the TRAJ program. The trajectory tracing was carried out for seven 500 ev electrons passing through the field of

```
          1    10    15    20    50    55    60    70
    1-100. -40. -34. -30.  30.  34.  40. 100.
    4-100. -40. -34. -30.  30.  34.  40. 100.
    7-100. -40. -34. -30.  30.  34.  40. 100.
   10-100. -40. -34. -30.  30.  34.  40. 100.
   15-100. -40. -34. -30.  30.  34.  40. 100.
   20-100. -40. -34. -30.  30.  34.  40. 100.
   32-100. -40. -34. -40.  30.  34.  40. 100.

          1    10    15    20    50    55    60    70
    1 100. 100. 100. 100. 100. 100. 100. 100.
    4  85.  85.  85.  85.  85.  85.  85.  85.
    7  79.  79.  79.  79.  79.  79.  79.  79.
   10  75.  75.  75.  75.  75.  75.  75.  75.
   15  58.  58.  58.  58.  58.  58.  58.  58.
   20  35.  35.  35.  35.  35.  35.  35.  35.
   32   0.   0.   0.   0.   0.   0.   0.   0.

   15    55     7    10      4000.
   15    20    10    15      4000.
   50    55    10    15      4000.

   20    50    10    15    21.568

           500.             .001            .110 1.00E-10
```

Figure 3.7: Typical data of the test lens of figure 3.6 used in the TRAJ program. Current density in the coil is 21.568. A.t/Cm^2.

figure 3.8. As discussed before, initially and finally the trajectories were assumed to be linear. The path of these electrons in the meridional plane is shown in figure 3.9.

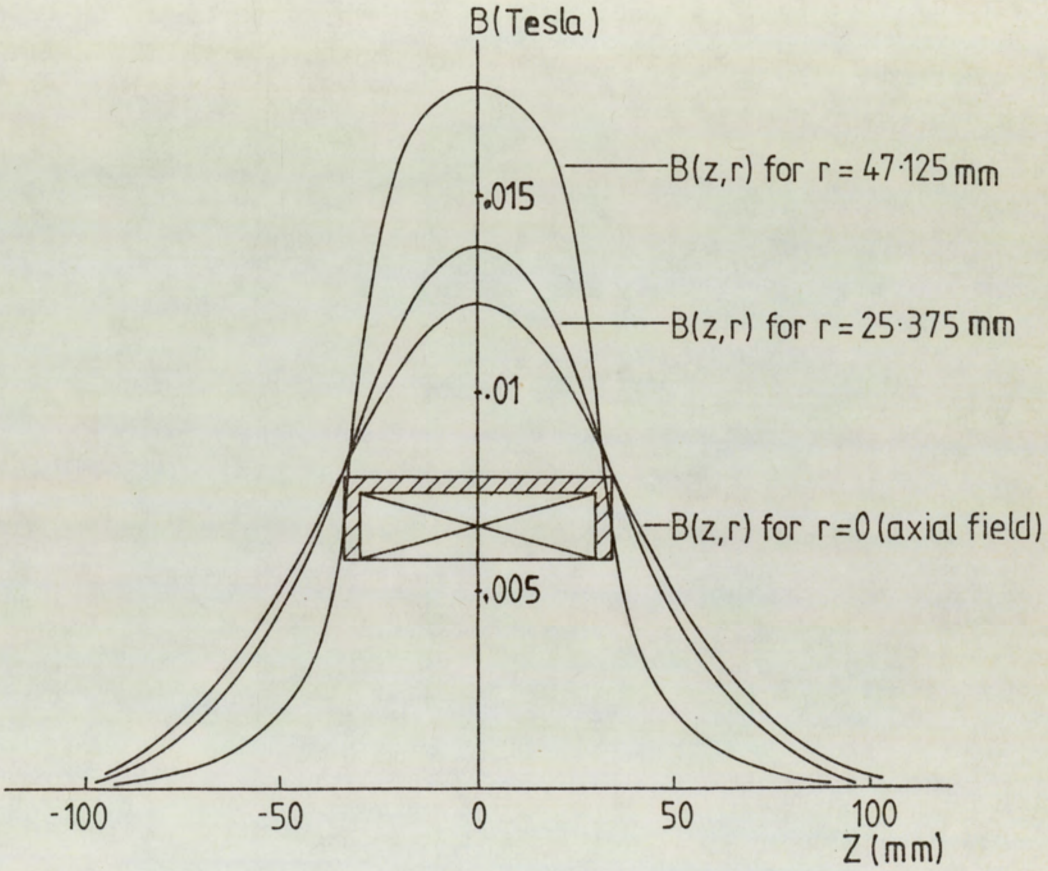

Figure 3.8: Variation of flux density B(z,r) with axial z - coordinates for three values of r, namely; r = 0, 25.4 and 47.1 mm ($NI/\sqrt{V_r} = 9.8$).

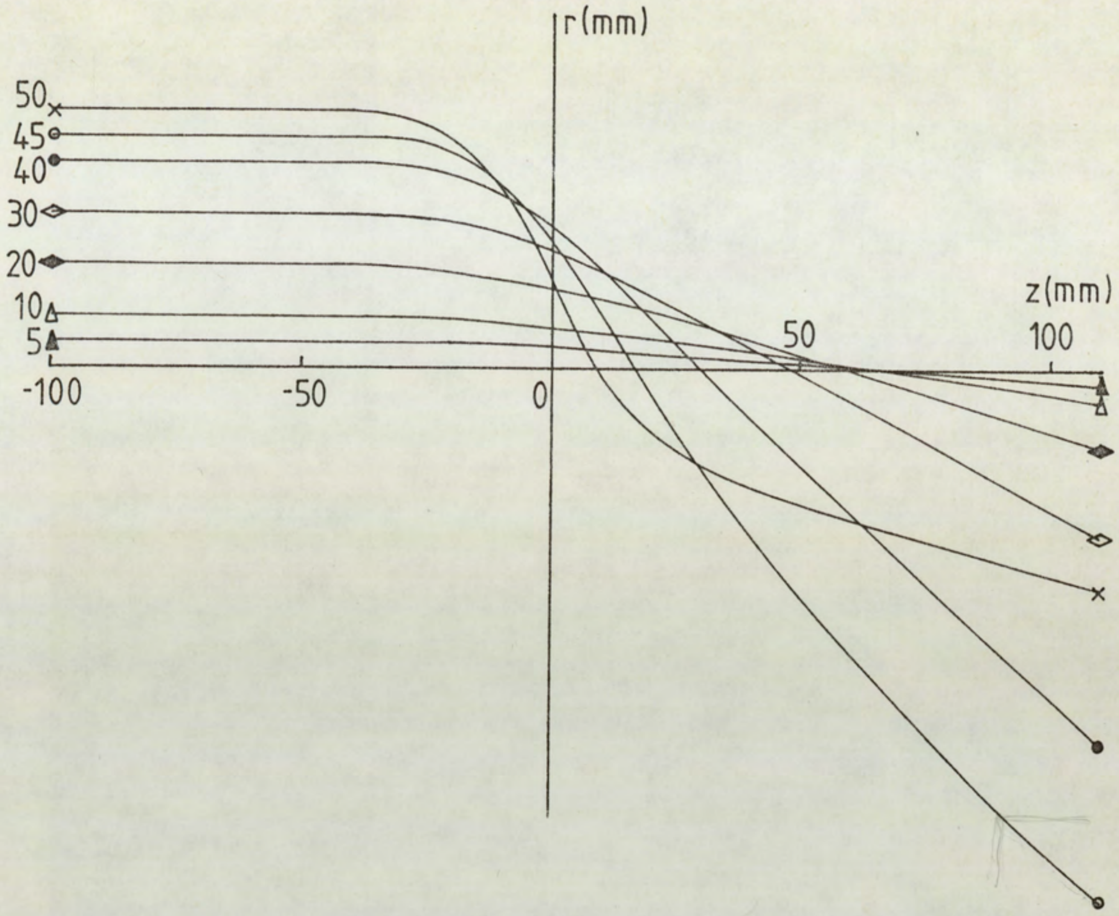

Figure 3.9: Ray tracing through the meridional plane for ray initially parallel to the axis $NI/\sqrt{V_r} = 9.8$. Accelerating voltage is 500 volt. Note the breakdown of the third order theory for off-axis rays e.g. electron of ray height 50 mm is bent strongly towards the axis.

While in Figure 3.10 the corresponding paths in the equatorial plane is drawn for the electrons of rays height 10 mm and 20 mm. The radial distortion was calculated from figure 3.9 using the assumption that

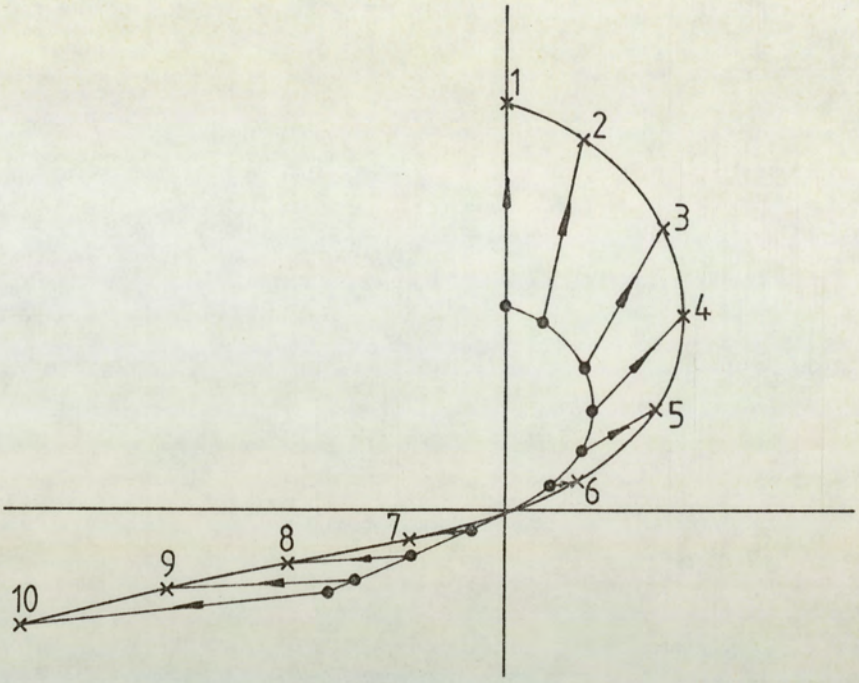

Figure 3.10: Trajectories of electrons of ray height 10 mm and 20 mm initially parallel to the axis through the equatorial plane. $NI/\sqrt{V_r} = 9.8$.

for a comparatively small ray height distortion is absent since the electrons then follow the gaussian trajectory. Accordingly, the gaussian image height ρ_G can be evaluated by:

$$(\rho_G)_i = \frac{\rho_1}{r_1} \times (r)_i \tag{3.15}$$

Hence, the percentage radial distrotion present for any point (i) can be found as:

$$\Delta\rho/\rho)_i = \frac{\rho_i - \rho_{Gi}}{\rho i} \times 100 \tag{3.16}$$

Using equations 3.15 and 3.16 the radial distortion was calculated for the set of electrons mentioned in figure 3.9. The variation of the radial distortion $\Delta\rho/\rho)_{rd}$ against the square of the initial height is shown in figure 3.11.

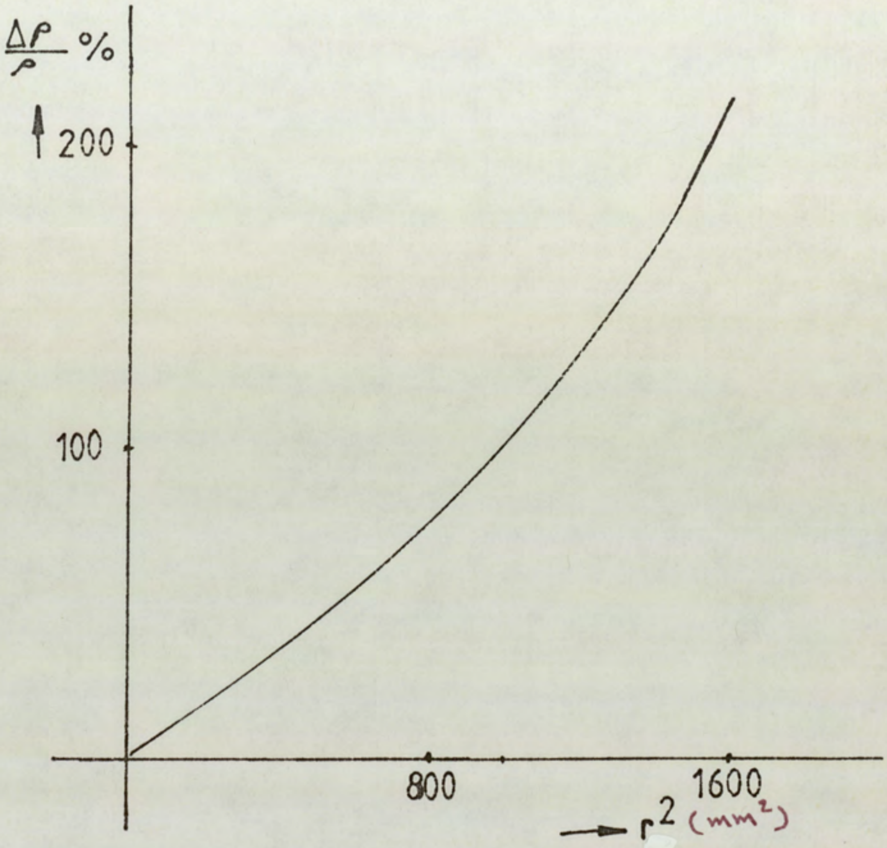

Figure 3.11: Variation of the radial distortion $\Delta\rho/\rho$% with r^2.

A simulation of the image of a cross wire can readily be produced since the computer output gives both the values of the image height ρ and the rotational angle θ for different points on the cross wire. Figure 3.12 shows the simulated distorted image produced by the Goddard test lens. This image explains the origin of the distortion in an image of the cross-wire shown previously in Figure (2.10b).

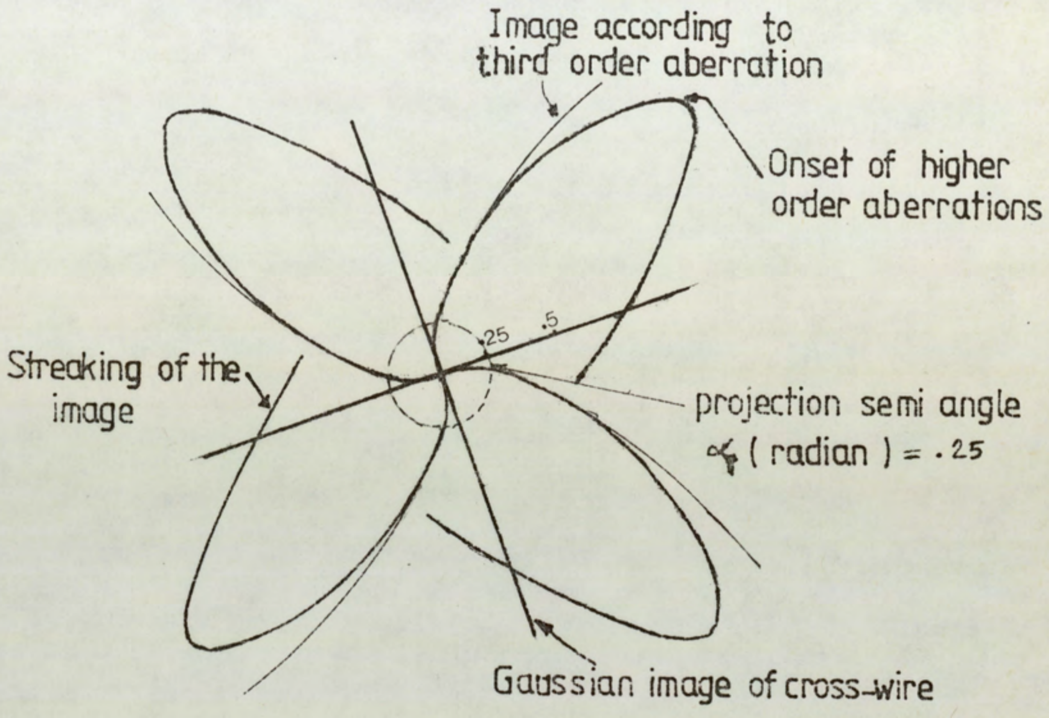

Figure 3.12: A) Gaussion image of a cross-wire and the computer simulated image actually by the Goddard test lens ($NI/Vr^{\frac{1}{2}} = 9.8$).

B) Image according to 3rd order aberration then,

C) Actual image calculated by the general ray equation, indicating the appearance of image " streaking " caused by higher order aberration.

3.8 THE SIMULATION PROGRAM 'IMAGE'

A computer program 'IMAGE' was written to simulate the image. This helps to visualize the appearance of the actual image of a square mesh grid object produced at the screen of the electron microscope. The program was based on the known object coordinate points. These points are generated in the subroutine described in Appendix B. Because of axial symmetry only eighth of the total object points are needed to represent the whole set. These are then used as an input ray heights for the 'TRAJ' program. The image coordinate points were computed accordingly. Using the plotting facilities in the ICL main frame computer, the image was simulated from the computed image coordinate points.

CHAPTER FOUR

DESIGN OF A WIDE-ANGLE PROJECTION SYSTEM

4.1 GENERAL DESIGN CONSIDERATIONS

In designing a wide-angle projection system it is useful to start with a simple model field distribution, disregarding the position of the polepieces. Such a model field distribution can be used for initial calculations of the design such as to simulate the trajectories of the two projector lenses. Besides that, one can use to advantage the asymmetrical behaviour of the single polepiece lens; mainly because there are two possible beam orientations for the single polepiece lens. This polepiece either faces the incoming rays or the fluorescent screen. The lens has higher aberration when the beam of electrons enters the field from the steep part of the field, i.e. the polepiece facing the screen. This will cause the lens to exhibit a large Q value. Large amount of image distortion in the corrector lens, is useful for correcting the distortion produced by the final projector lens. The final projector lens is another single polepiece lens with its polepiece facing the beam. This is a favourable orientation leading to a low projector distortion. For example, Elkamali et. al. (1977) found that at a projection semi-angle (α_p) of 8^o, the double polepiece lens shows 2% of spiral distortion, while 1.3% distortion is found in the single polepiece lens.

According to the above considerations a model field distribution can be chosen, whereby the trajectories are calculated at the selected excitation. From these trajectories the polepieces shape has been modified to allow the passage of the rays through the polepiece structure. The outline design of the wide-angle projector system, suggested by the author (1979) depending on the previous method, is shown in Figure 4.1.

On the basis of the above discussion and because the necessary computer programs were available, such as the field distribution program, the aberration programs and the general ray program, a suitable design was developed. Figure 4.2 illustrates the integral magnetic circuit of the design. In this figure, the main meshes needed for the computation of the magnetic field are shown. Three important points arise in the design of a wide-angle projection unit. The first is that the small bore projector lens produces a smoothly rising magnetic field. The second requirement is a wide bore corrector lens to allow a large beam of the incoming ray to pass through. This bore should not be larger than strictly necessary, so as to eliminate higher order aberrations from the image. A practical compromise for the size of this bore together with a suitable aperture is important here. Finally, the reduction of magnetic field cancellation between the two opposing fields must be considered. This is achieved in practice by using an intermediate iron plate. The position of this plate is determined by the fact that ideally it should not affect the desirable field distribution of the projector

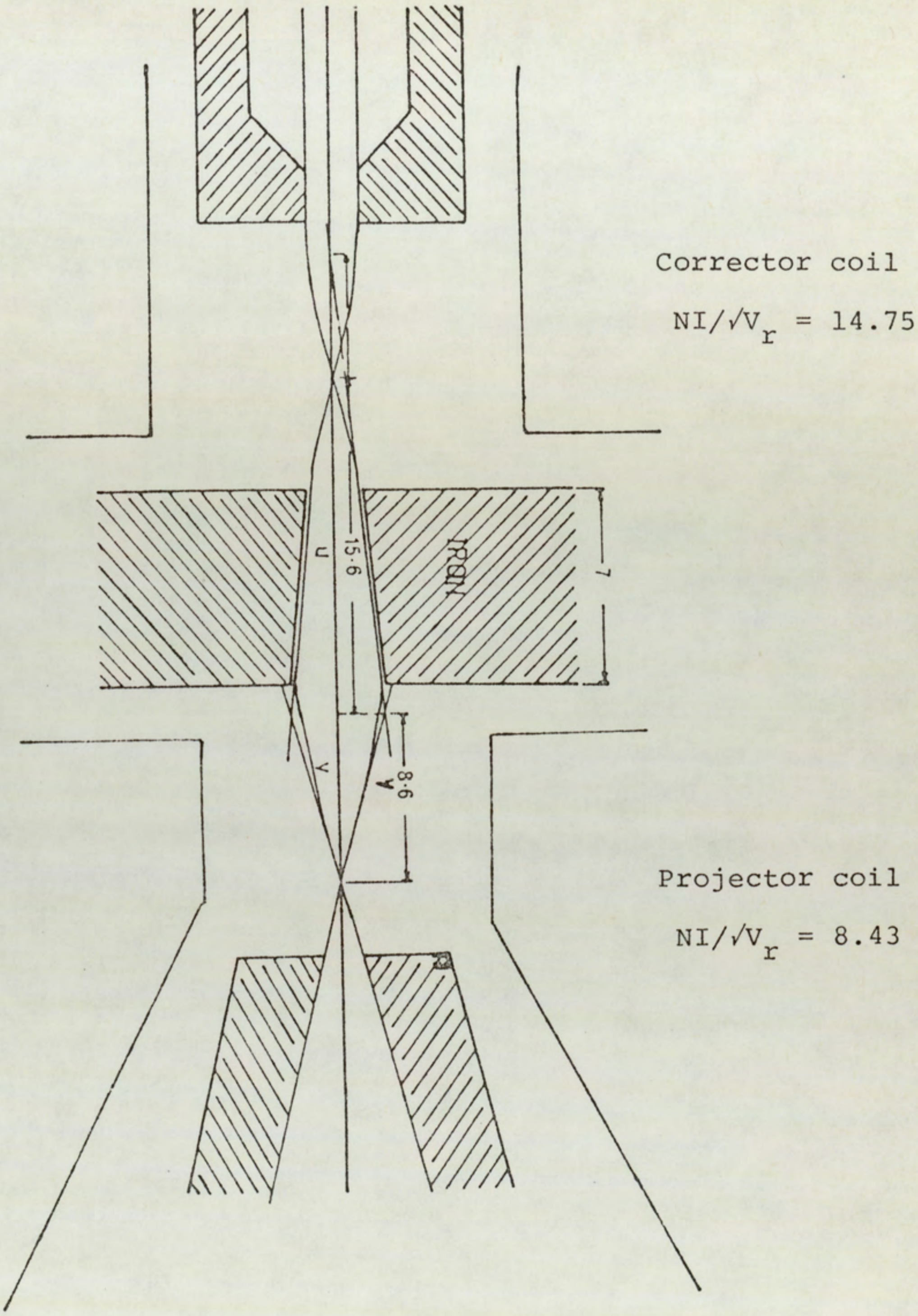

Figure 4.1: Outline design for a wide-angle projector system.

Whose distotion aberrations should be kept to the absolute minimum. The field distribution of the conector lens on the other hand, not so critical since its spiral distortion aberration must in any case be large. Moreover in the present correction system the spiral distortion of this lens can be varied over wide limits it needed by smilarly adjusting the lens excitation

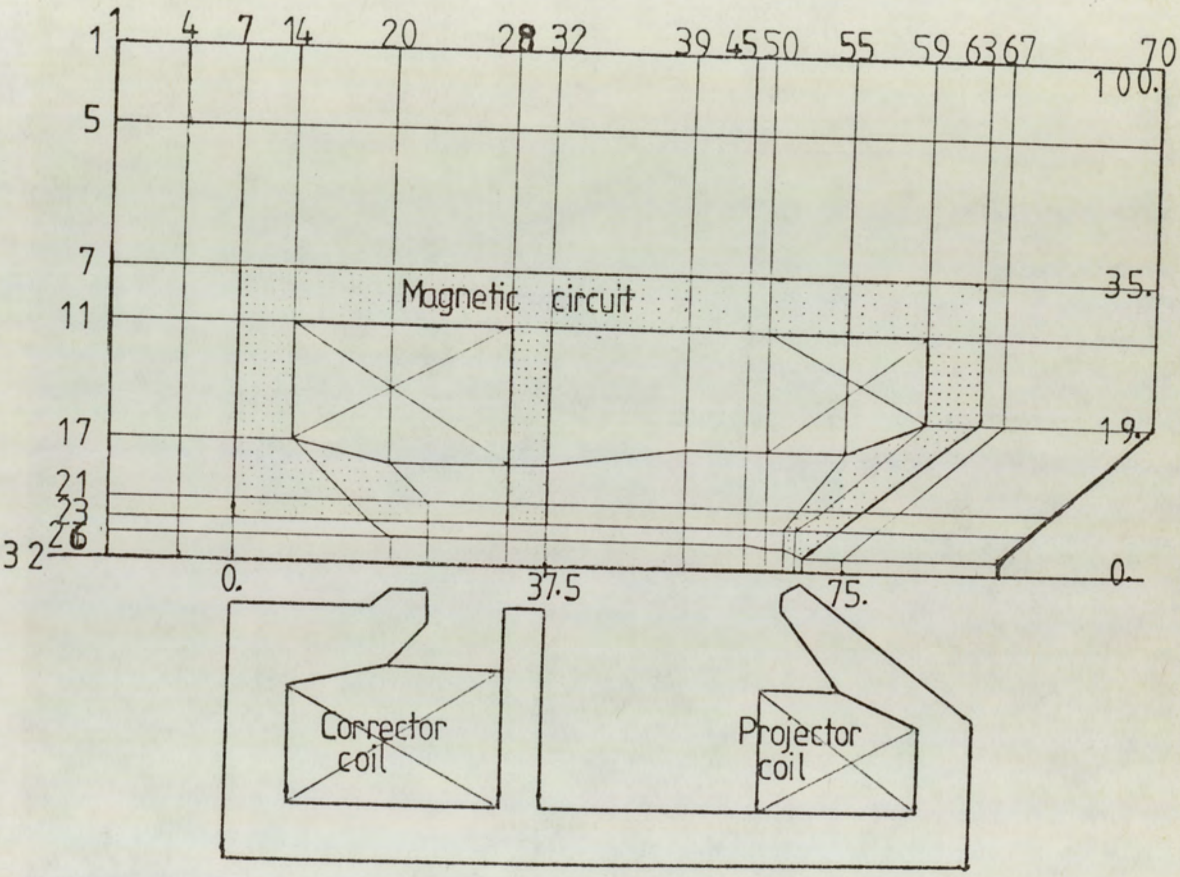

Figure 4.2: The finalized design of the wide-angle integral unit. The mesh distribution used in the computation of the field distribution is shown in the upper part of the diagram.

In any compromise between the desirable electron optical property of the single-polepiece lenses and the need to avoid field cancellations, between the corrector and the projector, the performance of the corrector should be sacrificed rather than that of the projector, i.e. the iron middle plate should be placed near to the corrector lens. The important aspect of the screening action of the middle plate is that it should preserve the desirable shape of the magnetic field distribution of the projector lens which thereby retains its very low spiral distortion.

The design of the correcting system was aimed at overcoming the difficulties encountered by previous workers in simultaneously correcting radial and spiral distortion. In particular, it was desirable to remove the alignment problem of two separate lenses by using an integral unit constructed with pre-aligned polepieces.

4.2 THE EXPERIMENTAL INTEGRAL UNIT

The wide angle experimental distortion-free integrated lens unit is shown in Figure 4.3. The corrector polepiece bore is relatively large, 6 mm in diameter, and the distance from the polepiece face to the middle plate was 10 mm. The bore of the middle plate was 10 mm diameter and the distance between the middle plate to the projector polepiece face was 29.5 mm.

The iron magnetic circuit consists of three main parts; the body and two lids (i.e. the polepieces). Figure 4.4 illustrates the construction of the lens system. It is made from "O" quality mild steel, with

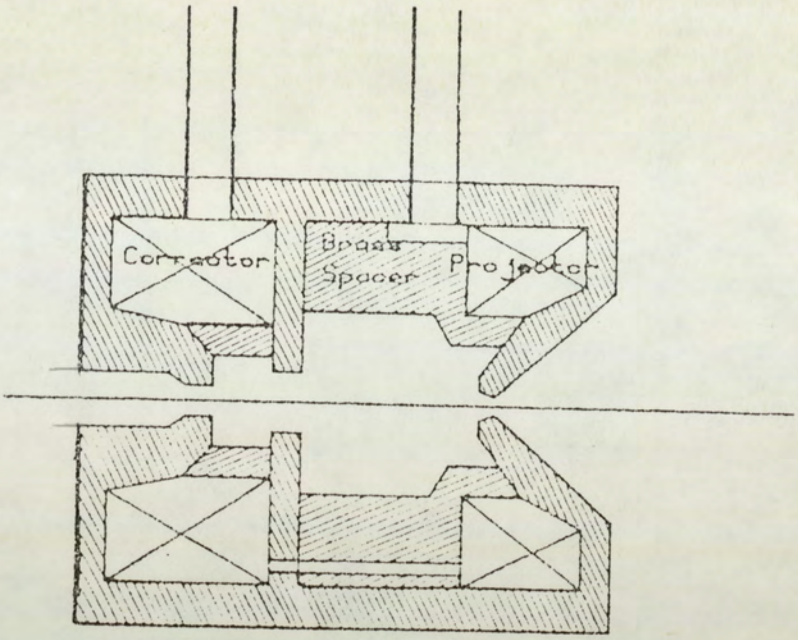

Figure 4.3: Scale drawing of the integral wide-angle projection unit.

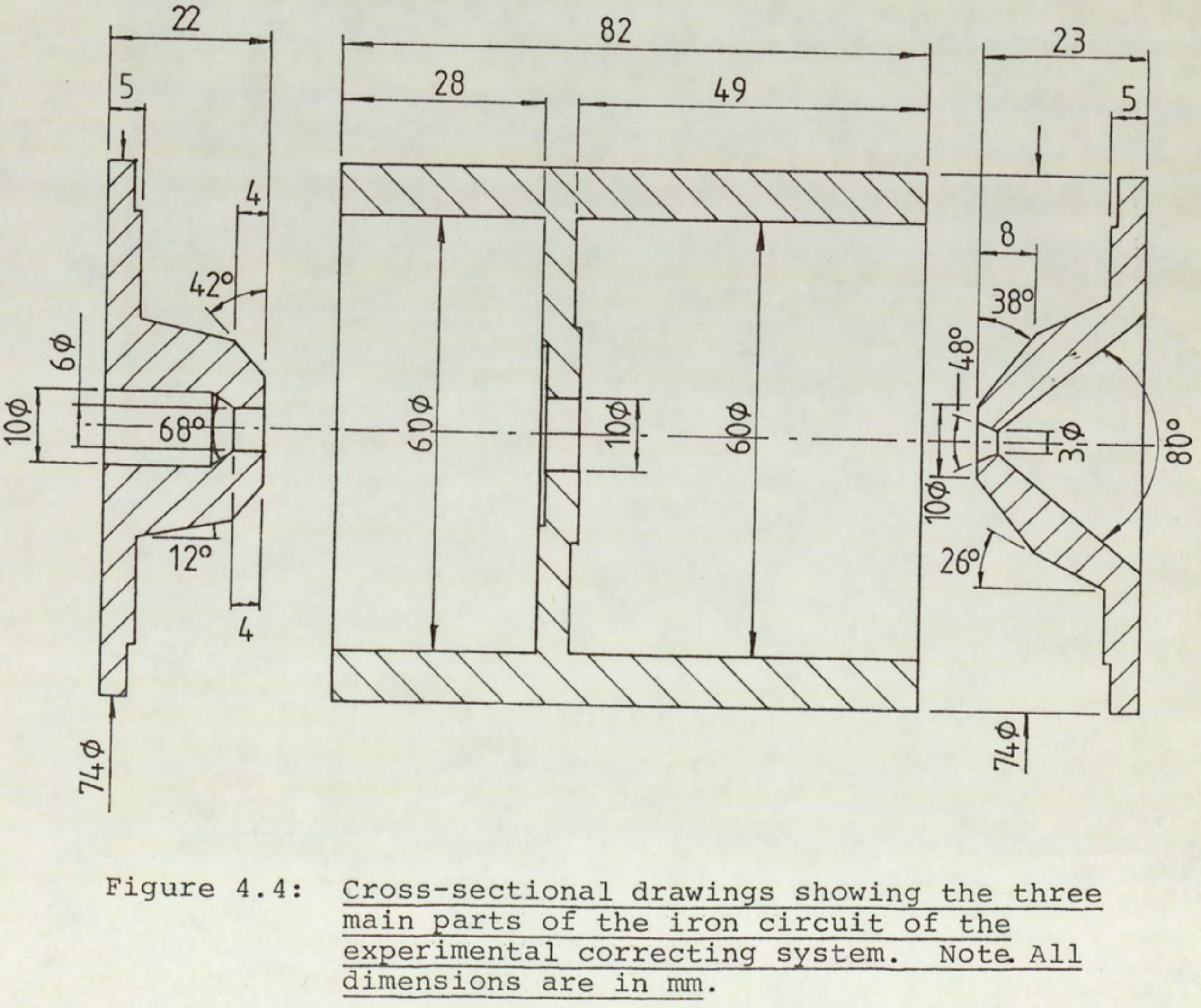

Figure 4.4: Cross-sectional drawings showing the three main parts of the iron circuit of the experimental correcting system. Note. All dimensions are in mm.

an overall diameter of 7.4 cm and an axial length of 9.0 cm. It is essential in this case to make sure that the three bores were made concentric. The area of the corrector coil in this design was 4.665 cm^2 while that of the projector was 2.75 cm^2. Hand winding of the coil on a perspex former (Figure 4.5) was used. The wire gauge used was 24 SWG, giving 340 turns for the corrector and 270 turns for the projector. The coils were water cooled by circulating tap water around the coils. The resistance of the corrector coil was 1.94Ω and that of the projector coil was 1.6Ω.

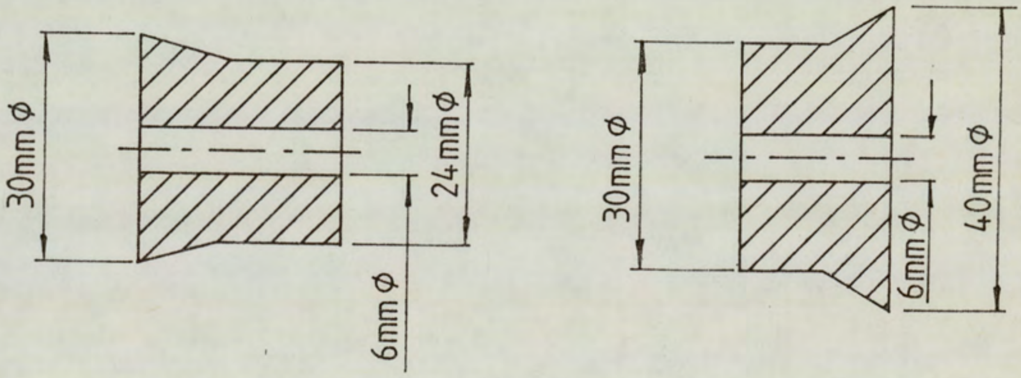

Figure 4.5: Coil formers for winding the lens of the integral correcting unit.

The axial flux density distribution for the projector lens with the corrector lens switched off, the corrector lens with the projector coil switched off, and the two lenses excited in the subtraction mode was measured experimentally. The measured field distributions are shown in Figure 4.6. The measurement was carried out using a Bell Model 120 Hall probe Gaussmeter. The experimental set-up is shown in Figure 4.7.

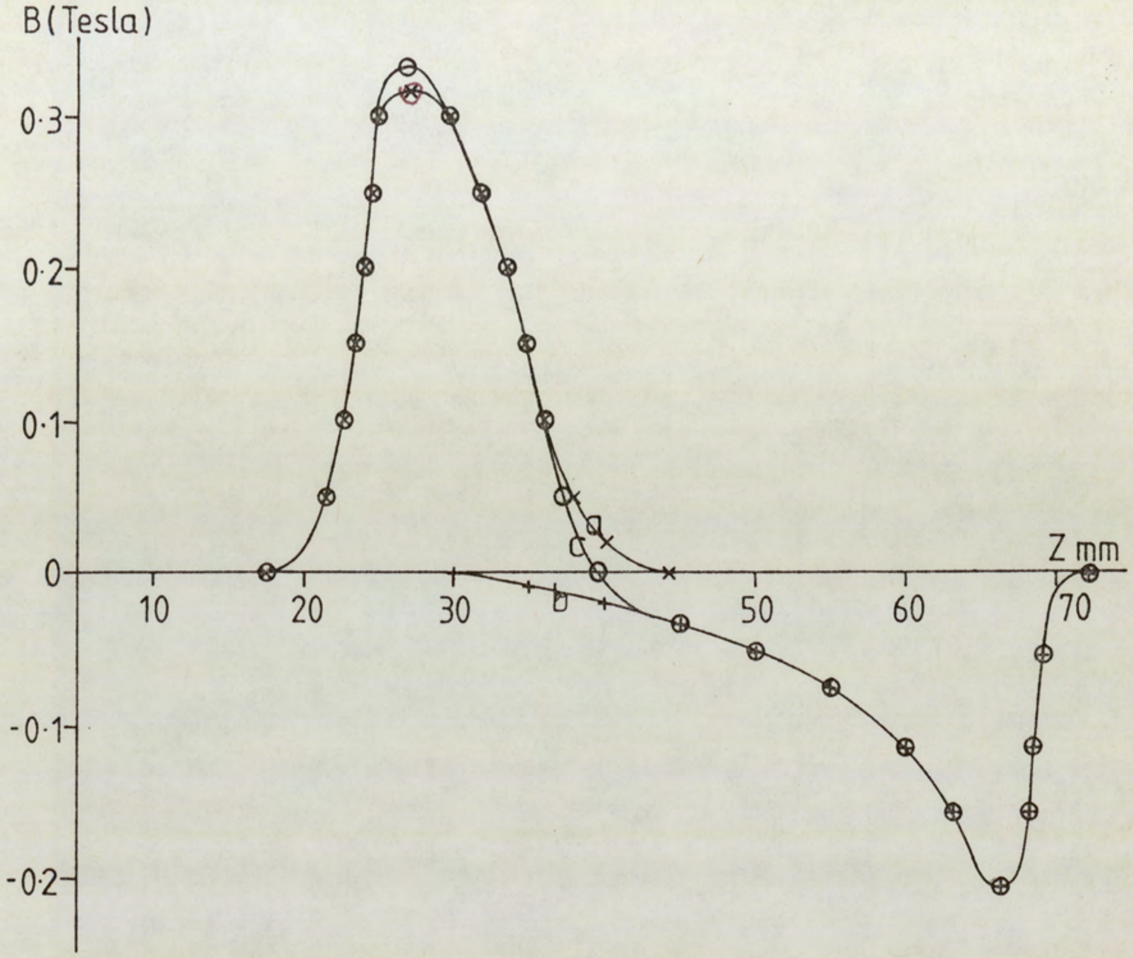

Figure 4.6: Axial field distribution of the integral correcting unit

(a) Corrector lens excitation 3060 A-t. Projector excitation zero.(⊖)

(b) Projector lens excitation 2134 A.t. Corrector excitation zero.(✱–)

(c) Projector excitation 2134, corrector excitation 3060 A-t.(⊗–)

Note. The total loss of lens excitation due to field cancellation is less than 6%.

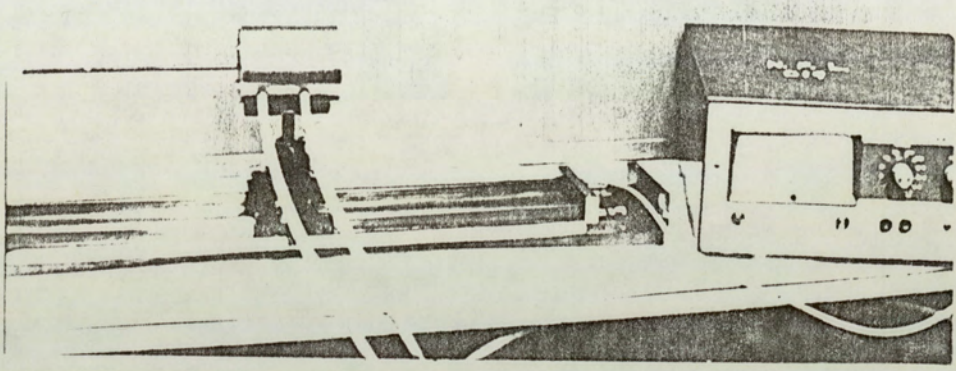

Figure 4.7: Hall probe Gaussmeter arrangement for measuring the axial field distribution of the integral lens unit.

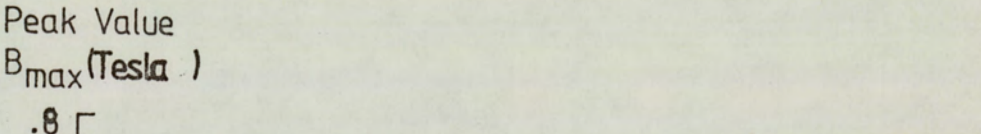

Figure 4.8: Variation of the peak magnetic flux density of projector and corrector as a function of their respective coil currents.

The variation of the peak value with increasing excitation $NI/\sqrt{V_r}$ (i.e. by increasing the current) was measured for both the corrector and for the projector. Figure 4.8 indicates that the lenses and in this case operated in the unsaturated region.

The focal properties and distortion factors of the projector lens, shown in Figure 4.9, and that of the corrector, shown in Figure 4.10, were calculated

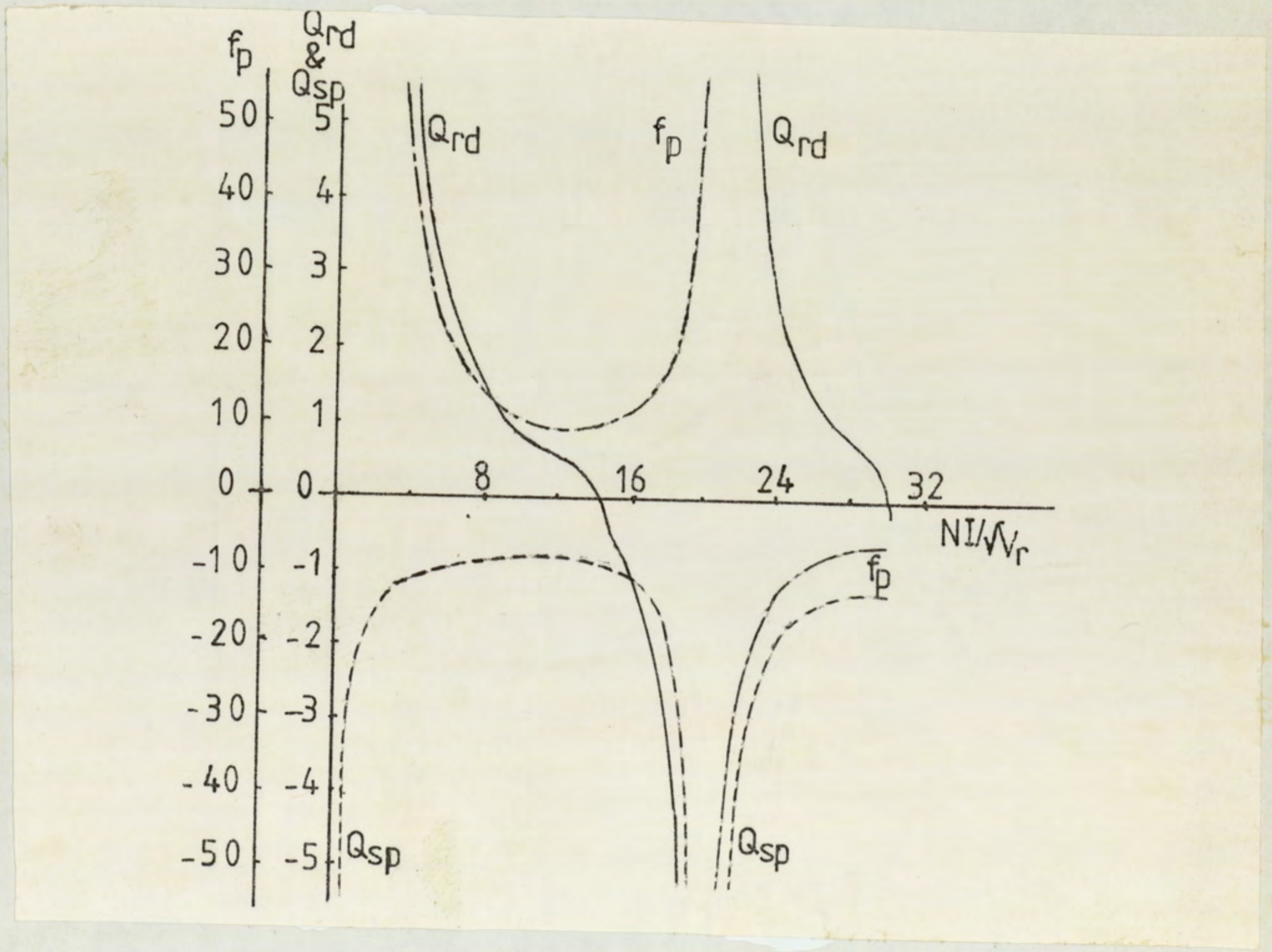

Figure 4.9: Electron optical properties of the projector lens of the wide-angle projection system (corrector lens switched off). Projector focal length fp radial Qrd and spiral Qsp distortion quality factors as a function of the projector excitation parameter $(NI/\sqrt{V_r})_{proj}$.

at different excitation parameters $NI/\sqrt{V_r}$. The experimental field distribution was employed in these calculations. The minimum focal length of the projector was 0.92 cm at an excitation parameter of ($NI/\sqrt{V_r} = 13$), while the minimum focal length of the corrector was 0.59 cm at an excitation parameter of $NI/\sqrt{V_r} = 13$. From

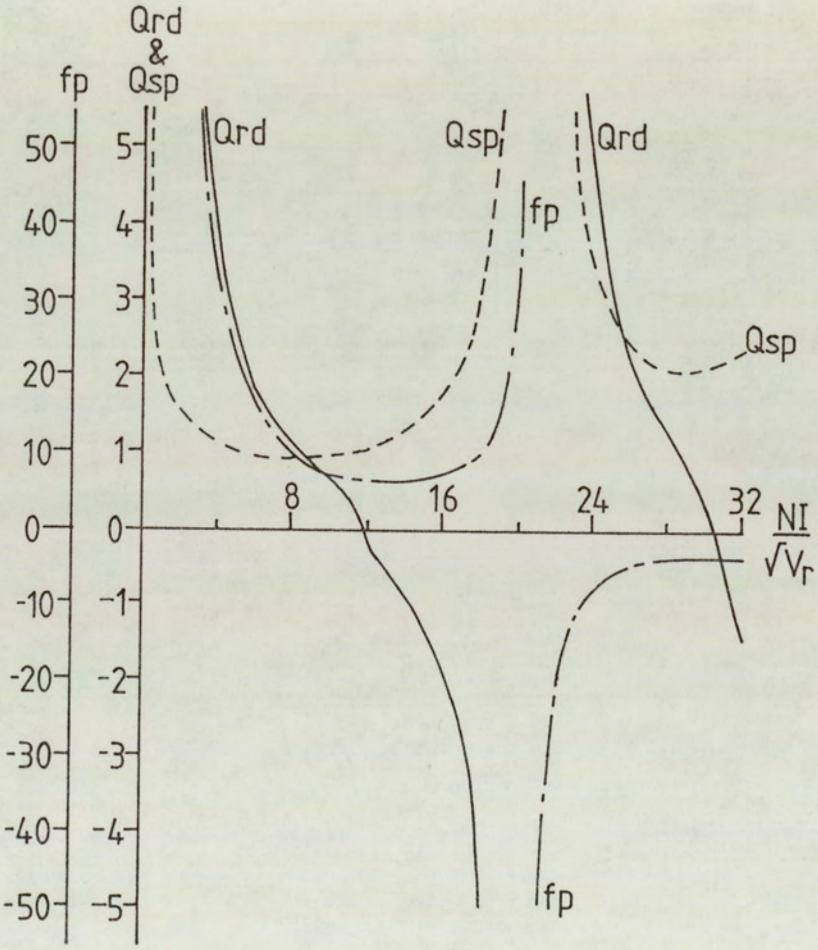

Figure 4.10: Electron optical properties of the corrector lens of the wide-angle projection system (projector lens switched off). Projector focal length fp radial Qrd and spiral Qsp distortion quality factors as a function of the corrector excitation parameter $(NI/\sqrt{V_r})_{corr}$.

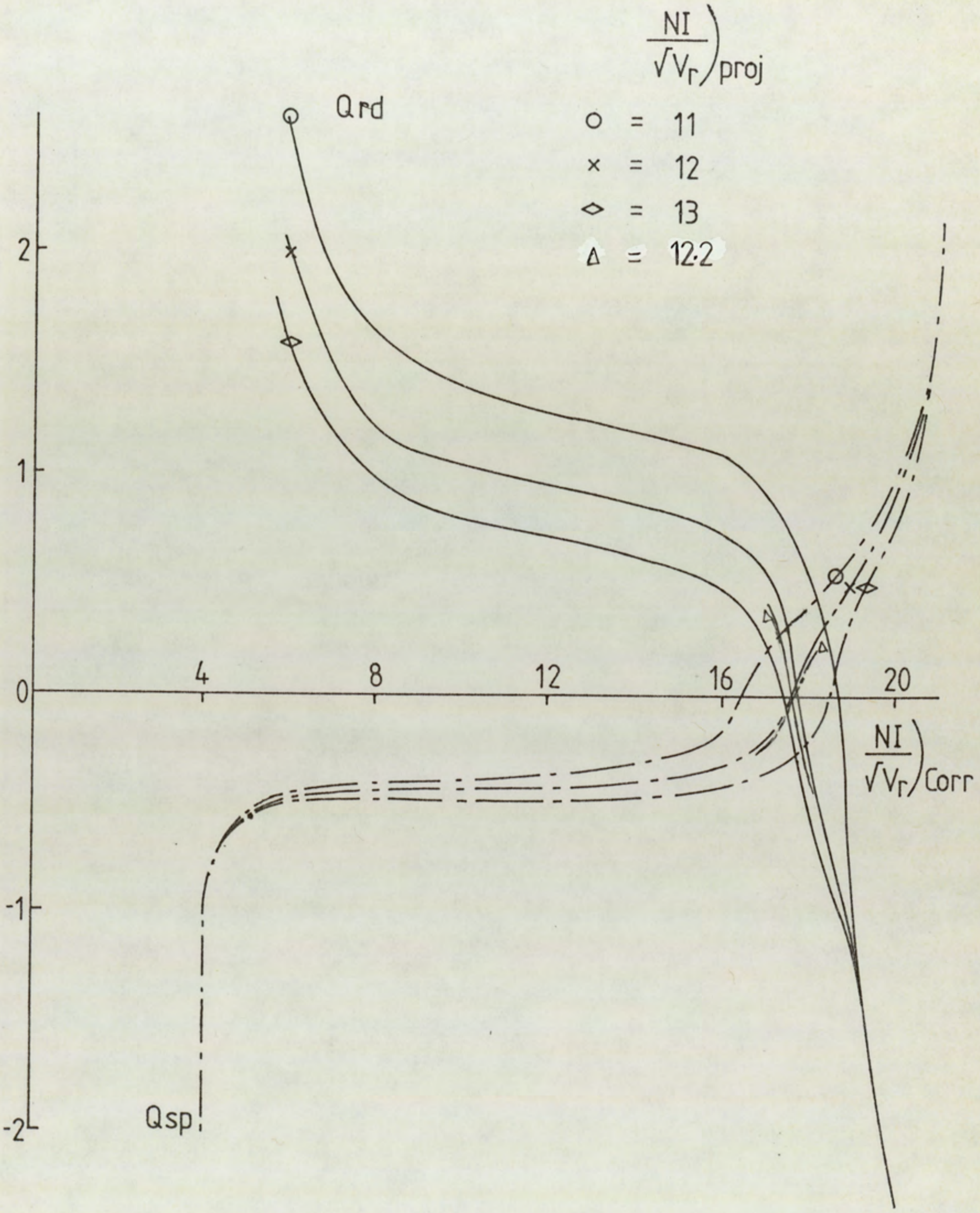

Figure 4.11: Variation of the distortion quality factor with excitation parameter of the corrector lens for different excitation parameters of the projector lens.
Note the condition of simultaneous correction of radial and spiral distortion in accordance with third order aberration theory.

the distortion quality factor curve it is clear that the radial distortion quality factor of the projector and that of the corrector vanish at excitation parameter of $NI/\sqrt{V_r} = 14$ and 13.5, respectively.

Radial and spiral distortion quality factors, of the system with both lenses energized, as a function of the corrector excitation at three different projector excitation (11, 12 and 13) as shown in Figure 4.11.

These results showed that operating the lens with the corrector at an excitation parameter $NI/\sqrt{V_r} = 17.8$ and the projector at excitation parameter $NI/\sqrt{V_r} = 12.2$ in the subtraction mode, gives an image with an angle of $\alpha p > 30$ for a ray height of r = 3mm. Moreover, third order aberration calculations show that both radial and spiral distortions can indeed be corrected simultaneously. However, these calculations cannot be expected to apply accurately to off-axis rays. This is where the need arises to find the real trajectories of the electron passing through such a field without relying on third order aberration theory. The general ray program (TRAJ) was therefore, applied to find the trajectories of different incident rays passing through the field of the integral lens unit operated in the region specified above. Figure 4.12 illustrates the resulting electron trajectories; this shows that for incident beam of

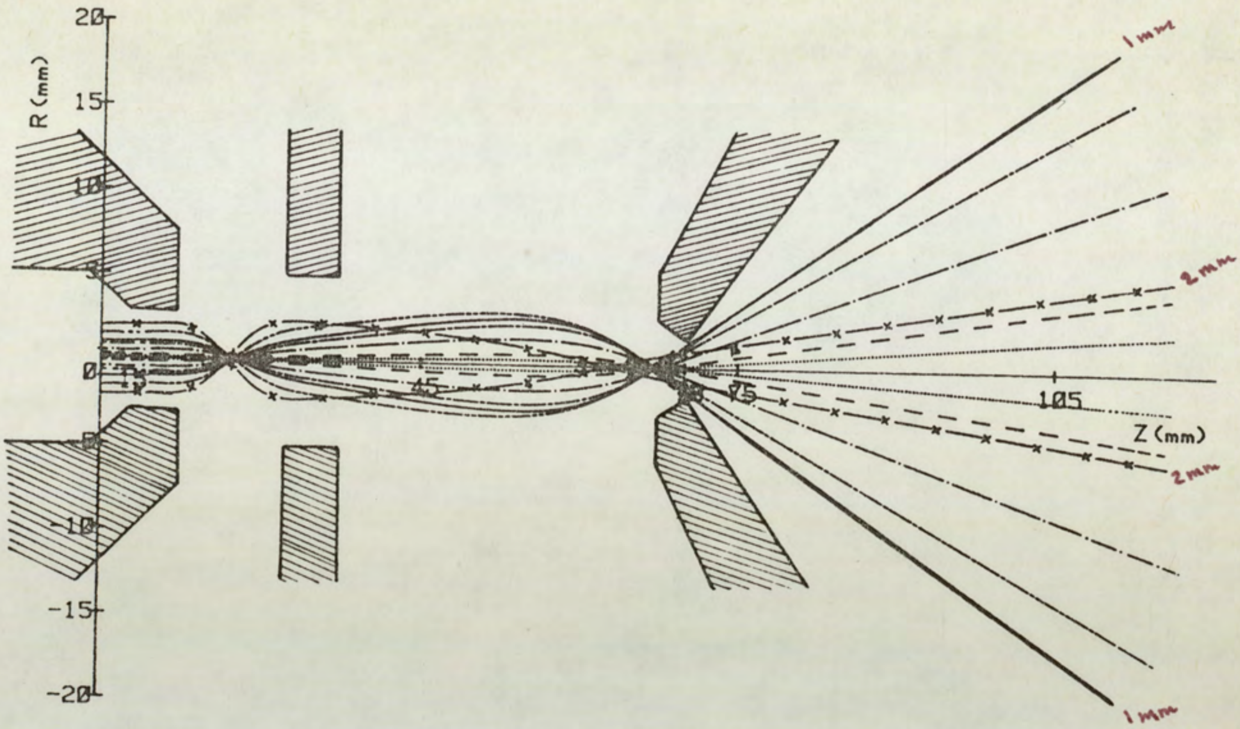

Figure 4.12: Computed general ray trajectories with the polepiece configuration of the wide-angle projector unit. $NI/\sqrt{V_r}$ of the corrector = 17.8 and $NI/\sqrt{V_r}$ of projector = 12.2.
Note the failure of correction for marginal rays R > 1 mm, for example r = 2 mm.

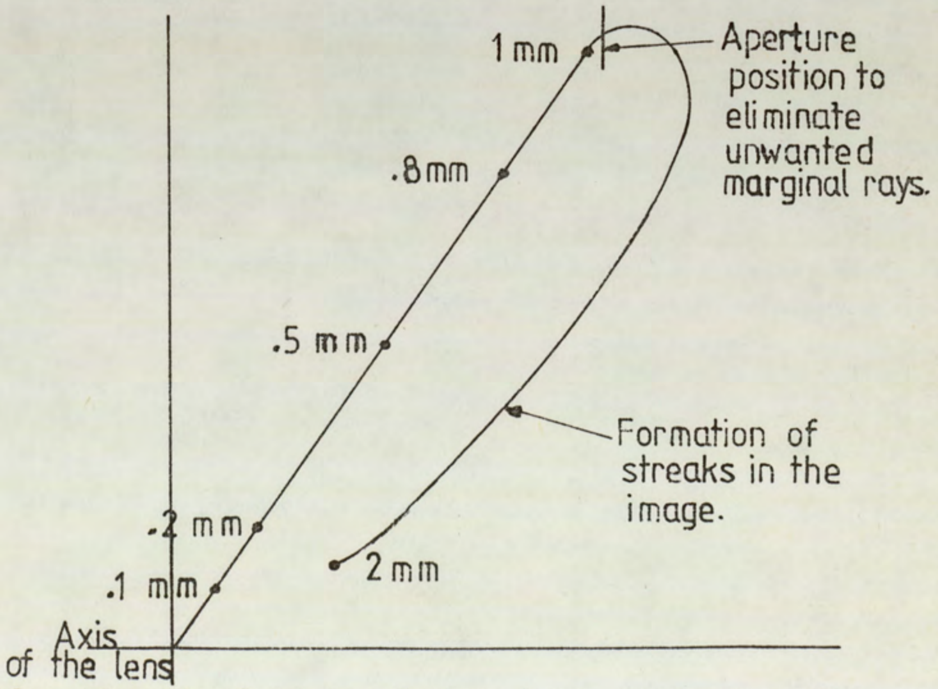

Figure 4.13: The simulation of the above rays as will be seen at the screen.
Note the sudden appearance of large radial distortion after ray height 1mm which causes streaks in the image.

radius R = 1 mm ($\alpha p \simeq 30^{\circ}$) radial distortion is virtually absent. Similarly the image rotation calculations (Figure 4.13) show that spiral distortion is virtually absent. However, for ray height R = 2 mm, the trajectories show that the correction no longer holds. Here the idea of introducing an aperture to limit the height of the incident rays was considered, since Figure 4.14 confirms the idea of the breakdown of correction for such off-axis rays. This figure shows a corrected image in the middle of the fluorescent screen surrounded by streaks arising from incident electrons of considerable radial height.

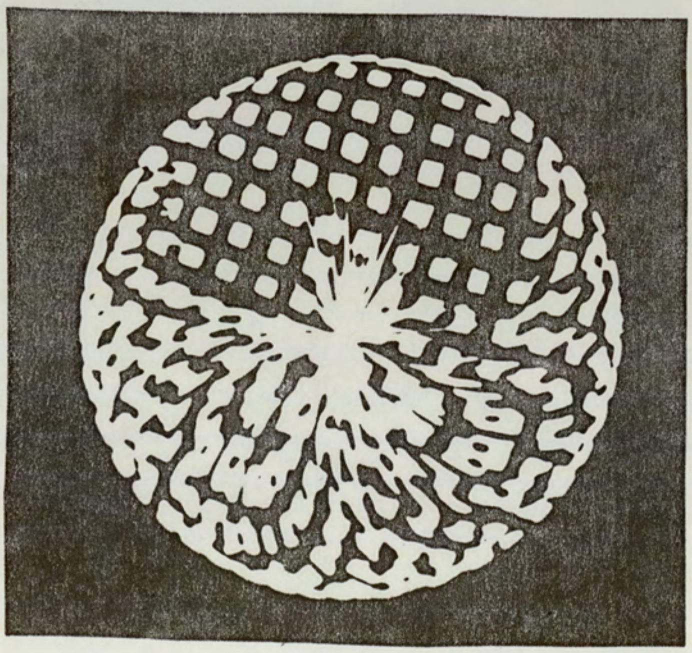

Figure 4.14: A preliminary experimental image of a square mesh grid taken with the wide-angle projector system (external photography) showing residual distortion as well as radial streaks resulting from off-axis rays indicating the breakdown of third order aberration theory.

4.3 EXPERIMENTAL ARRANGEMENT

The experimental arrangement of the integrated lens unit mounted in the viewing chamber of an existing JEOL-Superscope instead of the internal photographic plate camera is shown in Figure 4.15. The JEOL-Superscope was used for evaluating the performance of the projection unit. The integrated system was inserted by removing the transmission screen, and placing the lens unit into the position shown in Figure 4.15. This set-up reduced the projection distance from 20 cm to 6.6 cm, so that a projection semi-angle of more than 30° was available.

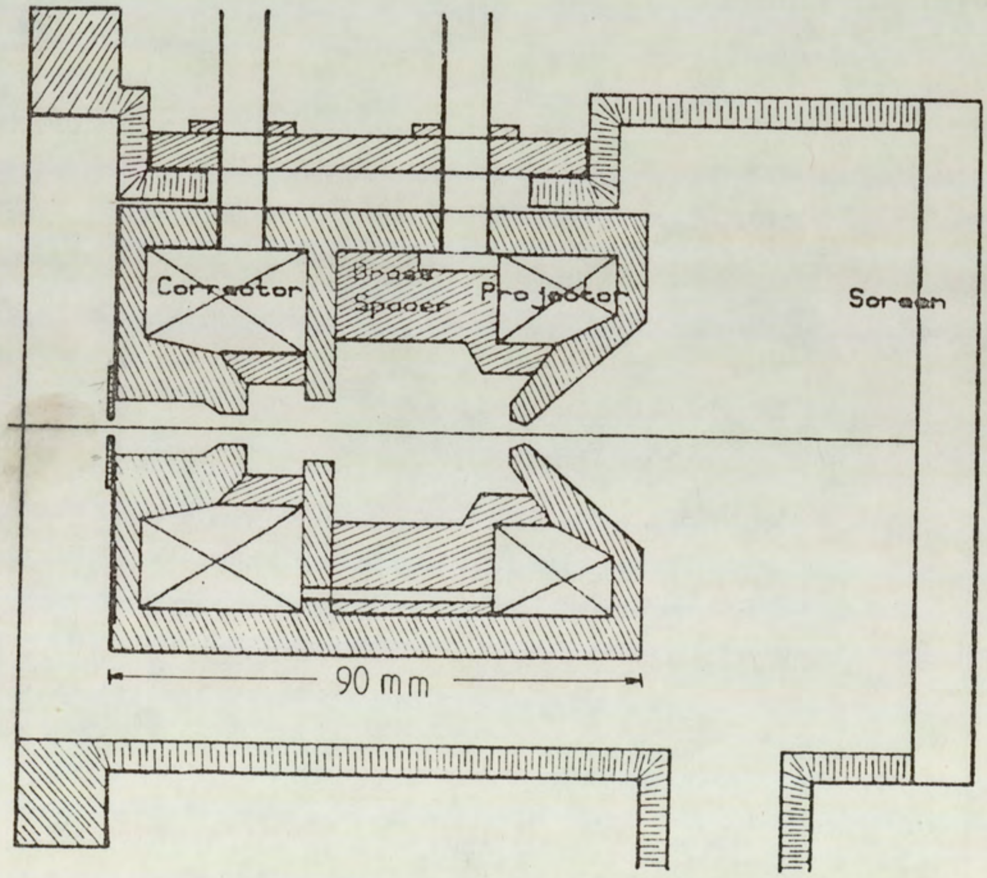

Figure 4.15: The experimental integral wide-angle projection system fitted in the viewing chambers of the JEOL-Superscope.

This image on the screen was photographed by external photography as shown in Figure 4.16. The external camera was placed 29 cm away from the screen.

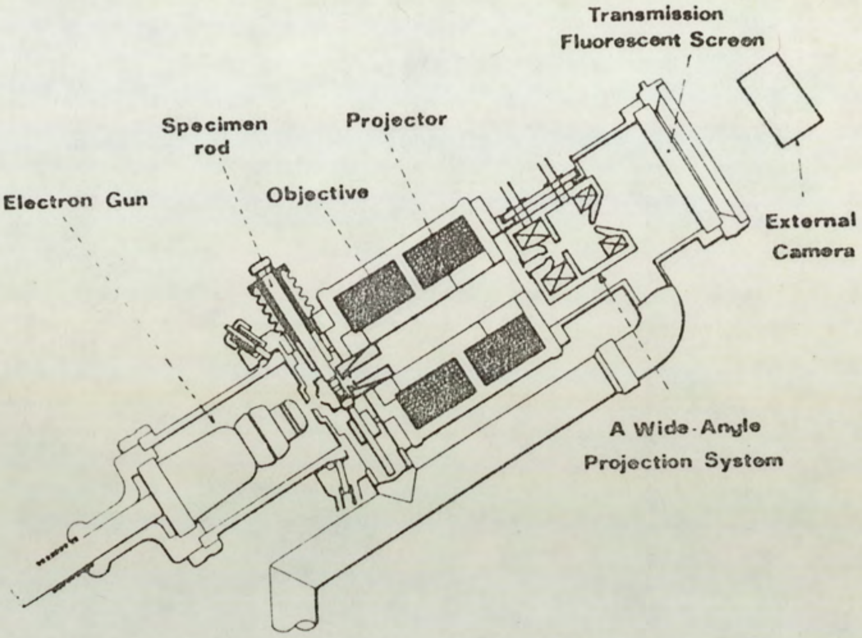

Figure 4.16: Experimental arrangement for external photography of the transmission screen.

An aperture of 2 mm diameter was used at the entrance of the lens unit shown in Fig. 4.15 to restrict the height of the incoming electrons and so get rid of the unwanted radial streaks mentioned before.

4.4 EXPERIMENTAL RESULTS

Guided by the previous calculation, the corrector was operated at excitation parameter $NI/\sqrt{V_r} = 17.8$, i.e. at the end of the first focal zone to produce the large amount of spiral distortion needed to compensate the spiral distortion produced by the projector lens. This excitation produces a virtual image with a considerable amount of unwanted barrel distortion besides the needed spiral distortion. The projector lens was operated at an excitation parameter $NI/\sqrt{V_r} = 12.2$ which is just below the point of minimum focal length. Here, reducing the excitation of the projector lens below the excitation level for zero radial distortion produces an appropriate amount of pin-cushion distortion to compensate the unwanted barrel distortion. Figure 4.17a shows the wide-angle image obtained in the modified 'Superscope' compared to the image (Figure 4.17b) obtained in the original unmodified 'Superscope'. The latter shows the size comparison of the image obtained by internal photography, (the inner square) with 1.5% distortion at a semi-angle $\alpha p = 6.4^{\circ}$; the black cross wires show the image seen on the fluorescent screen. Here the distortion present is 7% at a semi-angle of 14°. The outer circle is an extrapolation to the image that would be observed for a semi-angle of 28°. The distortion calculated in this case amount to 30%. Figure 4.18 shows some typical wide-angle distortion-free images formed by the correcting system. The specimens were (a) biological in which a rat pancreas is shown (b) an Aluminium (AL)-alloy on a carbon film and (c) a replica of a worn surface. The inner circle here corresponds to the size of the image in the standard microscopes.

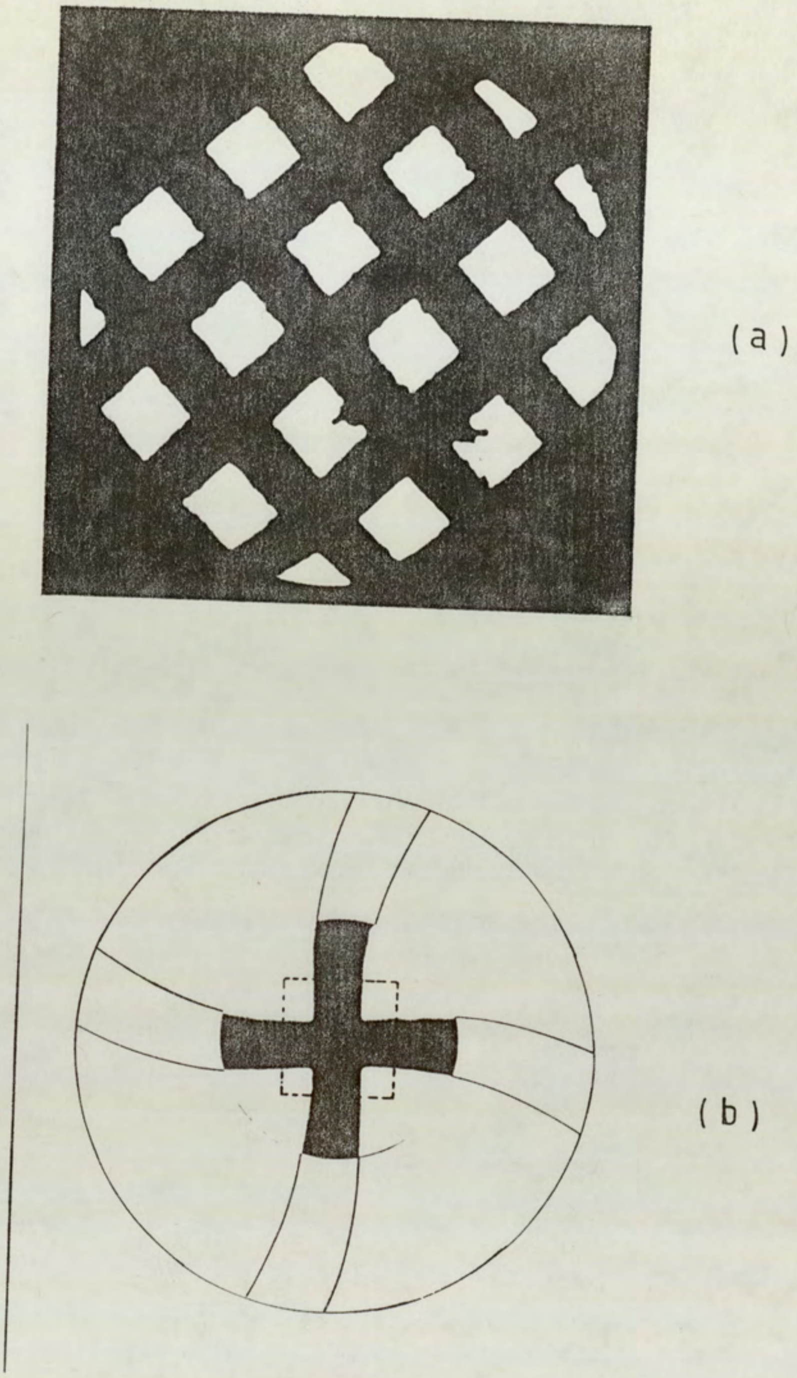

Figure 4.17: A comparison of two images taken by the 'Superscope' externally.

(a) A distortion-free wide-angel ($\alpha p=28^{o}$) projection image taken with the wide angle projection system fitted in.

(b) Without the projection system, the inner circle is the image taken to the screen externally the outer circle is the extrapolation of the image to the same angle as in (a), and dotted square showing the size of the image photographed internally.

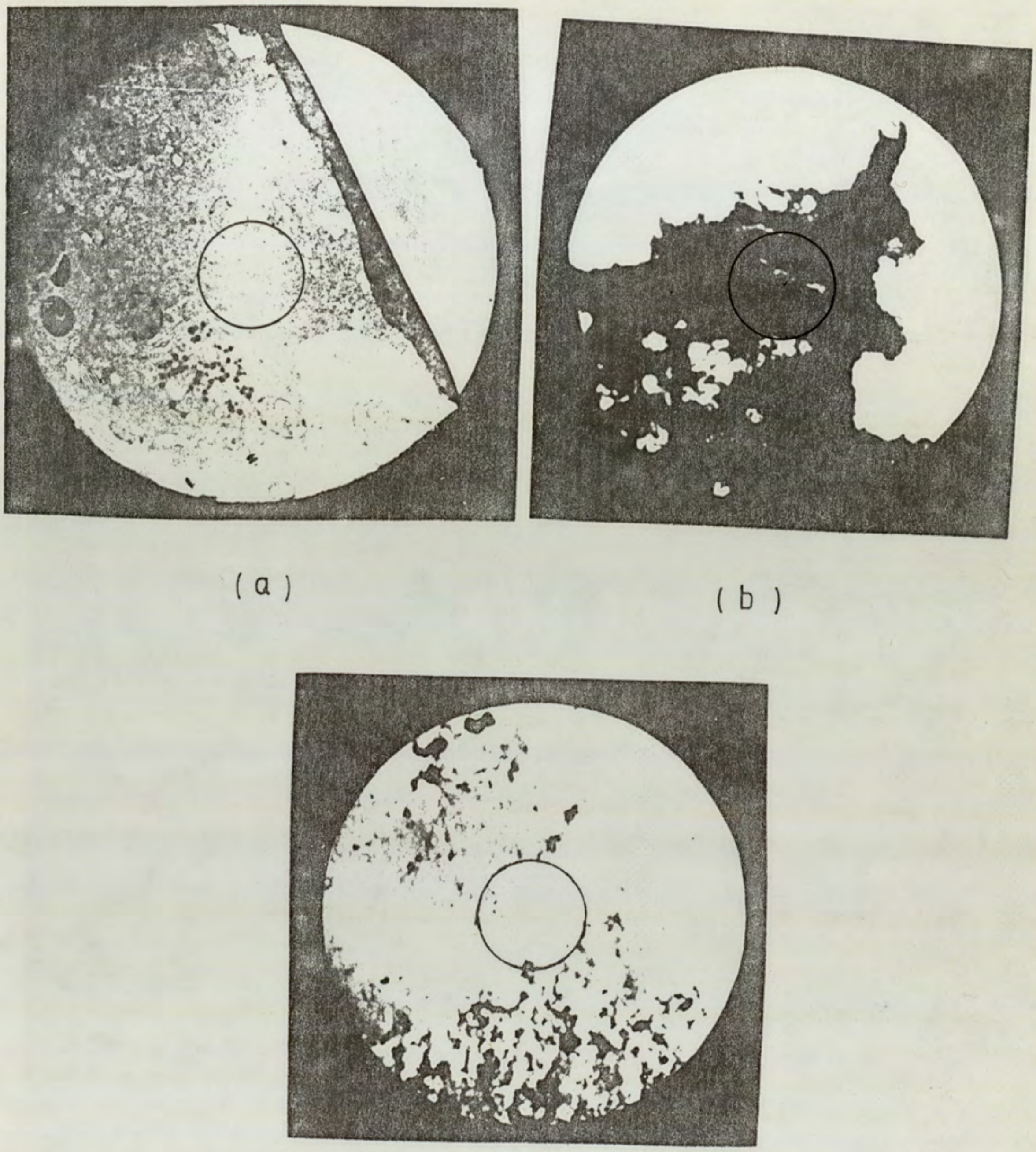

(a)

(b)

(c)

Figure 4.18: Typical wide-angle ($\alpha p \simeq$ ~~8~~3$0^{\circ}$) projection images. Projection distance is 68.2 mm (external photography).

(a) Biological specimen (pancreas of a rat.

(b) Al-Alloy on a carbon film.

(c) Replica of a worn surface the inner circle shows the size of the image in a standard microscope.

CHAPTER FIVE

CONCLUSION AND DISCUSSION

In the present investigation, it has been shown that, in the design of the wide-angle projection systems, third order aberration theory, which is based on paraxial rays, gives only a first approximation to the image distortion. In particular, it does not predict the sudden onset of the higher order aberrations which cause radial streaks to appear in the image. The general ray equation has proved a more satisfactory approach for the determination of the actual trajectories, thereby simulating directly the appearance of the image on the viewing screen.

It should be mentioned that the present design for wide-angle projection unit avoids alignment problems associated with separate projector lenses; in addition field cancellation has been reduced to 6% in such a system. The bore of the final projector lens acts as a differential pumping aperture which maintains a good vacuum in the electron-optical column. Such a wide-angle projection system could find an immediate application in a TEM with a transmission fluorescent screen such as the JEOL 'Superscope' in which the lens has been tested and also with the AEI Corinth electron microscope. The new arrangement would allow standard size photographic plates to be located in the optimum position for minimum exposure.

Although the lens unit in this investigation has been tested at an accelerating voltage of 30 kV, it can be operated at accelerating voltages up to 220kV without iron saturation occuring by suitably increasing the excitation. For operating at higher voltages the lens dimensions and coil excitation can be scaled by a suitable factor. Scaling the dimensions of a lens and its excitation by a factor n does not affect the flux density in the iron circuit nor does it affect the correction of distortion. However, the magnification will be reduced by the same factor n. For example, if the scaling factor n is taken 2.7 the lens can be operated at accelerating voltages up to 1 million V at a reduced magnification of about 13.

The employment of the wide-angle distortion-free integrated unit is not, of course, restricted to transmission electron microscope with transmission fluorescent screen. The viewing chamber of TEM needs to be redesigned when the correction unit is used.

Wide-angle correcting system can also be useful in scanning transmission microscopes. In modern scanning transmission electron microscope a large amount of information from the specimen under investigation is expected to be provided simultaneously by the use of different kinds of detectors and techniques. Craven et. al. (1980) has discussed the importance of the use of post-specimen lens systems in STEM to allow the desired range of angular distribution of the scattering angle of the electrons leaving the specimen to reach the appropriate detectors. The range of the angular distribution needed is important in matching the angular distribution of electrons entering the electron detectors and the electron spectrometer. The analysis of the performance of the post-specimen lens system produced by Craven and Buggy (1981) and Craven, Buggy and Ferrier (1981) showed that one of the important parameters to be considered is the distortion introduced by the post-specimen lens system into the scattering distribution. We can therefore recommend the employment of the integrated wide-angle correcting system to provide interfacing projector lenses to ensure that the angular cone of rays leaving the specimen is matched to the optimum angle for the detector used.

To summarise, therefore, the use of wide-angle projector lenses will enable the viewing system of TEM and STEM to be optimised without sacrificing operational convenience since standard size roll film or plates can now be put into the optimum position. Large distortion-free viewing screens can be employed, enabling large objects to be viewed at comparatively high magnification. Similary the size of high voltage microscopes can be substantially reduced and their viewing systems designed in a more rational way than hitherto.

REFERENCES

Al-Hilly, S.M. (1979)
'A MATHEMATICAL ANALYSIS OF THE CORRECTION OF SPIRAL DISTORTION IN THE ELECTRON MICROSCOPE'
M.Sc. Project, Department of Physics, The University of Aston in Birmingham.

Al-Hilly, S.M. and Mulvey, T. (1981)
'WIDE-ANGLE PROJECTOR SYSTEMS FOR THE TEM'
EMAG '81, Inst. Phys. Conf. ser. no. 61 (1982) ed. M. Goringe. p. 103-106.

Craven, A.J., Ferrier R.P., Chapman, J.N. and Nicholson, W.A.P. (1980)
'DESIGN CONSIDERATIONS FOR A DEDICATED ANALYTICAL STEM'
in: Electron Microscopy (1980) Vol. 3. Seventh European Congress on Electron Microscopy. eds. P. Bredroo and Cosslett, V.E., p. 168.

Craven, A.J. and Buggy, T.W. (1981)
'DESIGN CONSIDERATIONS AND PERFORMANCE OF AN ANALYTICAL STEM'
Ultramicroscopy, North Holland . 7 PP. 27-37 (1981)

Craven, A.J., Buggy, T.W. and Ferrier, R.P. (1981)
'POST-SPECIMEN LENSES IN ELECTRON SPECTROSCOPY'
in: Met Soc Book 277: Conf. Proc. "Quantitative Microanalysis with high Spiral Resolution", UMIST Manchester 25-27 April 1981, paper no. 7.

Elkamali, H.H. (1981)
'IMPROVED LENS SYSTEMS FOR THE ELECTRON MICROSCOPE'
Ph.D. Thesis, Department of Physics, The University of Aston in Birmingham.

Elkamali, H.H. and Mulvey, T. (1977)
'IMPROVED VIEWING ARRANGEMENTS IN THE TEM'
in: Developments in Electron Microscopy and Analysis. ed. D.L. Misell. EMAG '77, Inst. Phys. Conf. ser. no. 36 p. 33-34.

Elkamali, H.H. and Mulvey, T. (1980)
'A DOUBLE LENS SYSTEM FOR THE CORRECTION OF SPIRAL DISTORTION'
EMAG '79, Inst. Phys. Conf. ser. no. 52 Chapter 1. ed. T. Mulvey p. 63-64.

Elkamali, H.H. and Mulvey, T. (1980)
'A WIDE-ANGLE TEM PROJECTION SYSTEM'
in: Electron Microscopy 1980, Vol. 1.
SEVENTH EUOPIAN CONGRESS ON ELECTRON MICROSCOPY. eds. P. Brederoo and G. Boom p. 74-75.

Goddard, L.S. (1944)
'THE COMPUTATION OF ELECTRON TRAJECTORIES IN AXIALLY SYMMETIC FIELDS'
Proc. Phys. soc. no. 56, p. 372-378.

Goddard, L.S. and Klemperer, O. (1944)
'ELECTRON RAY TRACING THROUGH MAGNETIC LENSES'
Proc. Phys. soc. no. 56, p. 378-396.

Hillier, J. (1946)
'A STUDY OF DISTORTION IN ELECTRON MICROSCOPE PROJECTION LENS'
Journal of Applied Physics 17 no. 6, p. 411-420.

Hindy, I.K. (1980)
'THE NUMERICAL SOLUTION OF THE GENERAL RAY EQUATIONS IN ELECTRON OPTICS'
M.Sc. Project, Department of Physics, The University of Aston in Birmingham.

Juma, S.M. and Mulvey, T. (1974)
'NEW ROTATION-FREE MAGNETIC ELECTRON LENSES'
in: Electron Microscopy. ed. J.V. Sanders and D.J. Goodchild. Canberra: Australian Academy of Sciences
Vol. 1, p. 134-135.

Juma, S.M. and Mulvey, T. (1975)
'A NEW EXPERIMENTAL ELECTRON MICROSCOPE WITH A ROTATION-FREE PROJECTION SYSTEM'
in: Development in Electron Microscopy and Analysis. ed. J.A. Venables. EMAG '75. New York: Academic Press
p. 45-48.

Juma, S.M. and Mulvey, T. (1978)
'MINIATURE ROTATION-FREE MAGNETIC ELECTRON LENSES FOR THE ELECTRON MICROSCOPE'
J. Phys. E: Sci. Inst. Vol. 11, p. 759-764.

Klemperer, O. and Barnett, M.E. (1971)
'ELECTRON OPTICS' 3rd ed.
Cambridge Monographs on Physics. Chapter 5, p. 107-151.

Kynaston, D. and Mulvey, T. (1963)
'THE CORRECTION OF DISTORTION IN THE ELECTRON MICROSCOPE'
Journal of Applied Physics, Vol. 14, p. 199-206.

Lambrakis, E., Marai, F.Z. and Mulvey, T. (1977)
'CORRECTION OF SPIRAL DISTORTION IN THE TRANSMISSION ELECTRON MICROSCOPE'
in: Devlopments in Electron Microscopy and Analysis. ed. D.L. Misell, Inst. Phys. Conf. ser. no. 36, EMAG '77, p. 35-38.

Liebmann, G. (1950)
'FIELD PLOTTING AND RAY TRACING IN ELECTRON OPTICS A REVIEW OF NUMERICAL METHODS'
Advanc. Electron. Vol. 2, p. 101-145.

Liebmann, G. (1951)
'MAGNETIC ELECTRON MICROSCOPE PROJECTOR LENSES'
Proc. Phys. Soc. B65, p. 94-108.

Marai, F.Z.A. (1977)
'ELECTRON-OPTICAL PROPERTIES OF SINGLE-POLE MAGNETIC ELECTRON LENSES'
Ph.D. Thesis, Department of Physics, The University of Aston in Birmingham.

Milne, W.E. (1933)
'ON THE NUMERICAL INTEGRATION OF CERTAIN DIFFERENTIAL EQUATIONS OF THE SECOND ORDER'
American Mathematical Monthly, Vol. 40, p. 322.

Mulvey, T. (1976)
'DESIGN TRENDS IN TEM, STEM AND SEM'
in: Electron Microscopy 1976, Vol. 1. Sixth European Congress on electron microscopy, ed. D.G. Brandon, p. 59-64.

Mulvey, T. (1980)
'ELECTRON GUNS AND INSTRUMENTATION'
in: Electron Microscopy 1980, Vol. 1. Seventh European Congress on electron microscopy. eds. P. Brederoo and G. Boom. p. 46-53.

Mulvey, T. and Newman, C.D. (1973)
'NEW ELECTRON-OPTICAL SYSTEMS FOR SEM AND STEM'
Scanning Electron Microscopy: systems and applications. ed. W.C. Nixon, Inst. Phys. Conf. Series (1973) p. 16-21.

Munro, E. (1975)
'A SET OF COMPUTER PROGRAMS FOR CALCULATING THE PROPERTIES OF ELECTRON LENSES'
University of Cambridge.

Nasr, H. (1978)
'COMPUTER SIMULATION OF DISTORTION IN THE ELECTRON MICROSCOPE'
M.Sc. Project, Department of Physics, The University of Aston in Birmingham.

Nasr, H. (1981)
'A CRITICAL ASSESSMENT OF THE FINITE ELEMENT METHOD FOR CALCULATING ELECTRIC AND MAGNETIC FIELDS'
Ph.D. Thesis, Department of Physics, The University of Aston in Birmingham.

Nasr, H., Chen, W. and Mulvey, T. (1981)
'IMPROVED PROGRAMS FOR CALCULATING OPTICAL PROPERTIES OF ELECTRON LENSES'
EMAG '81, Inst. Phys. Conf. ser. no. 61 (1982). ed. M. Goringe, p. 75-78.

Tsuno, K. and Harada, Y. (1981)
'ELIMINATION OF SPIRAL DISTORTION IN ELECTRON MICROSCOPY USING AN ASYMMETRICAL TRIPLE POLEPIECE LENS'
J. Phys. E: Sci. Instrum. Vol. 14, 1981, p. 955-960.

Tsuno, K. and Harada, Y. (1981)
'MINIMISATION OF RADIAL AND SPIRAL DISTORTION IN ELECTRON MICROSCOPY THROUGH THE USE OF A TRIPLE POLEPIECE LENS'
J. Phys. E: Sci. Instrum. Vol. 14, 1981, p. 313-320.

Tsuno, K., Arai, Y. and Harada, Y. (1980)
'ELIMINATION OF SPIRAL DISTORTION IN ELECTRON MICROSCOPY BY MEANS OF A THREE POLEPIECE LENS'
in: Electron Microscopy (1980) Vol.1. Seventh European Congress on Electron Microscopy. eds. P. Bredroo and G. Boom, p. 955.

APPENDIX A

THE SCALING OF A MAGNETIC LENS AND ITS EFFECT ON DISTORTION

If the dimension and excitation of a magnetic lens are scaled by a factor n the magnetic field strength at the corresponding points of the original and scaled model are identical. This is true even if magnetic saturation is present, providing that the B-H properties of the iron circuit are the same in both lenses.

If we wish to retain the same excitation parameter $NI/\sqrt{V_r}$ in both lenses, the accelerating voltage is

$$V_{r_2} = n^2 V_{r_1}$$

where V_{r_1} is the relativistically corrected accelerating voltage of the original lens and V_{r_2} is that to be applied to the scaled lens.

The focal properties of the scaled lens can be predicted from these of the original lens, since the focal properties depend mainly on the excitation parameter $NI/\sqrt{V_r}$. For example, the focal length is scaled up by the same factor n, while the magnification is reduced by the factor n.

It should be mentioned here that image distortion will not be affected by such a scaling operation. The image distortion $\Delta\rho/\rho$, which is a dimensionless quantity is given by:

$$\frac{\Delta\rho}{\rho} = D\ r^2$$

where D, the distortion coefficient has dimension of (L^{-2}) and r the ray height has the dimension (L).

Thus the image distortion of the scaled lens will be

$$\Delta\rho/\rho = \left(\frac{D}{n^2}\right) \quad (n\ r)^2$$

$$= D\ r^2$$

Therefore the image distortion is not affected by scaling the lens.

APPENDIX B

SUBROUTINE FOR CALCULATING THE OBJECT POINTS OF THE SQUARE MESH

Because of symmetry in the case of a square mesh, ⅛ of the points can represent the points overall. Figure B.1 indicates that the points in the shaded triangle give the information needed to calculate the other points. Those object points Ro(i) have been calculated using the subroutine shown in Figure B2.

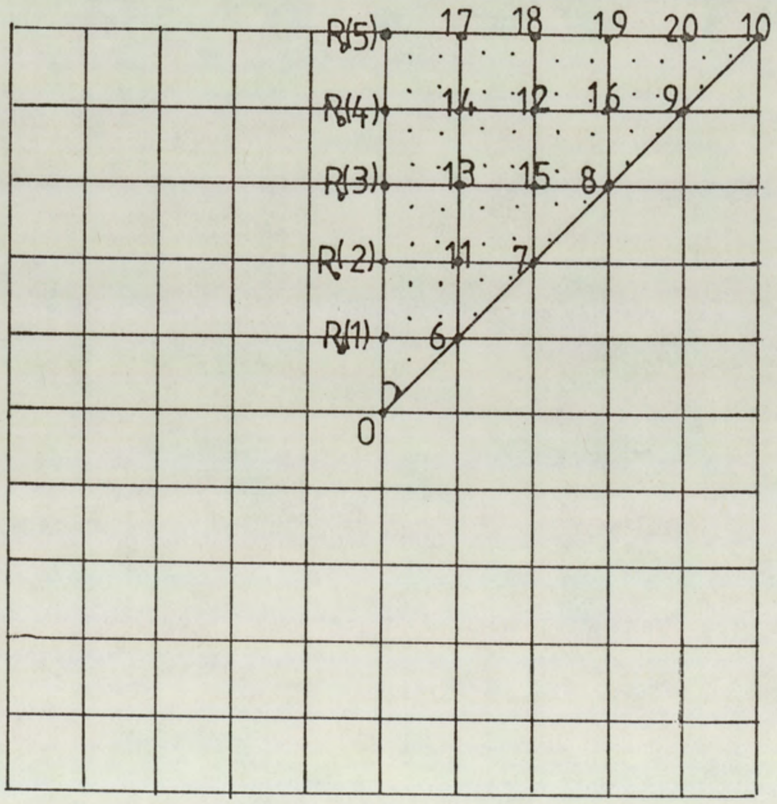

Figure B1: Square mesh representing the object points to be calculated where Ro(i) is the object ray height entering the field. θ is the rotational angle of the point.

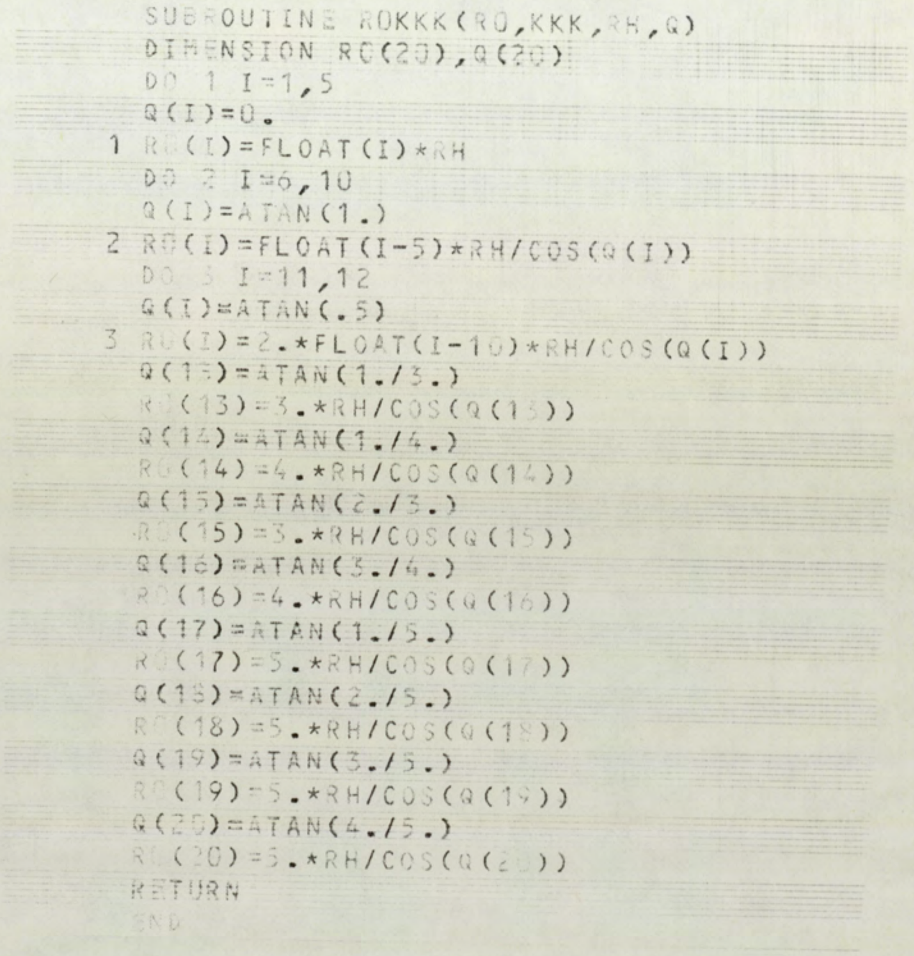

```
      SUBROUTINE ROKKK(RO,KKK,RH,Q)
      DIMENSION RO(20),Q(20)
      DO 1 I=1,5
      Q(I)=0.
    1 RO(I)=FLOAT(I)*RH
      DO 2 I=6,10
      Q(I)=ATAN(1.)
    2 RO(I)=FLOAT(I-5)*RH/COS(Q(I))
      DO 3 I=11,12
      Q(I)=ATAN(.5)
    3 RO(I)=2.*FLOAT(I-10)*RH/COS(Q(I))
      Q(13)=ATAN(1./3.)
      RO(13)=3.*RH/COS(Q(13))
      Q(14)=ATAN(1./4.)
      RO(14)=4.*RH/COS(Q(14))
      Q(15)=ATAN(2./3.)
      RO(15)=3.*RH/COS(Q(15))
      Q(16)=ATAN(3./4.)
      RO(16)=4.*RH/COS(Q(16))
      Q(17)=ATAN(1./5.)
      RO(17)=5.*RH/COS(Q(17))
      Q(18)=ATAN(2./5.)
      RO(18)=5.*RH/COS(Q(18))
      Q(19)=ATAN(3./5.)
      RO(19)=5.*RH/COS(Q(19))
      Q(20)=ATAN(4./5.)
      RO(20)=5.*RH/COS(Q(20))
      RETURN
      END
```

Figure B2: The subroutine for calculating the mesh points of the object.

APPENDIX C

Wide-angle projector system for TEM

(A paper published by the Institute of Physics for EMAG '81, Cambridge 1981).

Wide-angle projector systems for the TEM

S.M.Al-Hilly and T.Mulvey The Department of Physics, The University of Aston in Birmingham, Birmingham B4 7ET England.

In spite of the high resolving power now available in commercial electron microscopes, the electron optical design of the projector lens and viewing system has not changed significantly over the last forty years. This is largely due to the difficulty of reducing the radial and spiral distortion in the final projector to the tolerable limits of 1% radial and 2% of spiral distortion in the micrograph. This is invariably achieved by restricting the semi-projection angle (α_p) of the beam projected onto the fluorescent screen to about 0.1 radian (5.7°). For a photographic image of 100mm diameter, a minimum projection distance of 50cm is thus required between lens and photographic plate. This leads to bulky and inconvenient viewing chambers, especially in high voltage electron microscopes. Recently an experimental wide-angle projection system devised by Lambrakis et al (1977) has been modified for use in high voltage microscopes (El Kamali and Mulvey 1980) and essentially distortion-free images have been obtained at a projection semi-angle of 30°. Subsequent analysis of this system (El Kamali 1981) has shown that at such large projection angles, third order aberration theory, although a useful preliminary guide, cannot predict with sufficient accuracy the projected images actually observed on the microscope screen. This, therefore, makes it difficult to optimise the electron optical system without extensive experimental work. Recent advances in the calculation of magnetic fields (Nasr 1981) by the finite element method has made it convenient to use the general ray equation, and hence to determine the form of the final image directly and without recourse to aberration theory (Al-Hilly 1982).Since a wide-angle projector lens could find an immediate application in a TEM with transmission fluorescent screen, it was thought useful to employ computer-aided design in the construction of a wide-angle projector unit that could be readily inserted into an existing JEOL "Superscope" in place of the normal internal camera ($\alpha_p=6.4^{\circ}$) as illustrated in Figure 1. Because of the short projection distance (68.2mm) of the new lens unit an image with a projection semi-angle $\alpha_p \approx 30^{\circ}$ could easily be produced on the transmission fluorescent screen and photographed externally.

Figure 2 shows the construction of the lens unit in more detail. A nearly parallel beam of electrons from the objective lens enters the first (corrector) lens which is an asymmetrical lens strongly excited ($NI/V_r^{\frac{1}{2}} = 17.8$) beyond its minimum focal length but still in the first focal zone. The excitation and hence image rotation is in the opposite sense to that of the projector. The corrector lens produces a magnification of just over three with considerable spiral distortion (≈40%). This distorted image is projected onto the viewing screen by the projector lens so that the distortion produced by the projector lens is annulled. This arrangement is electron-optically favourable since the beam from the

0305-2346/82/0061-0103$01.50

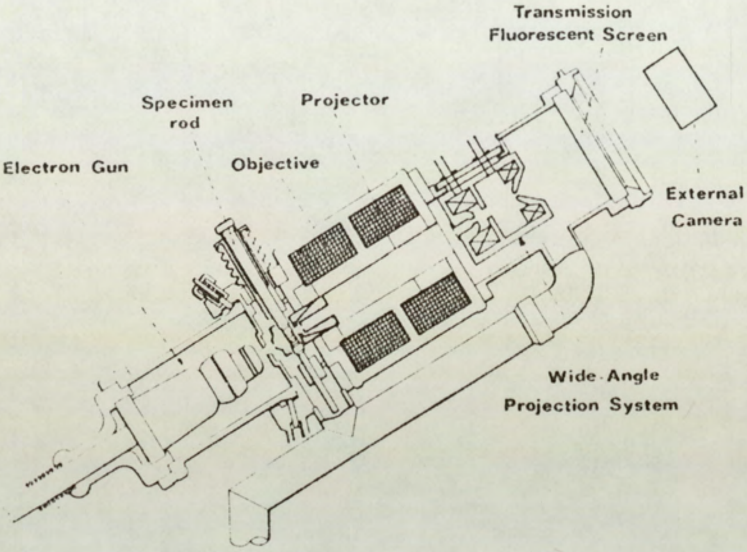

Fig.1. Cross-section of JEOL "Superscope" with transmission fluorescent screen. The internal camera (α_p = 6.4°) has been removed and a wide-angle (α_p = 28°) projector lens unit inserted in its place. Image diameter 70mm on fluorescent screen (M = 35). Photography by external camera.

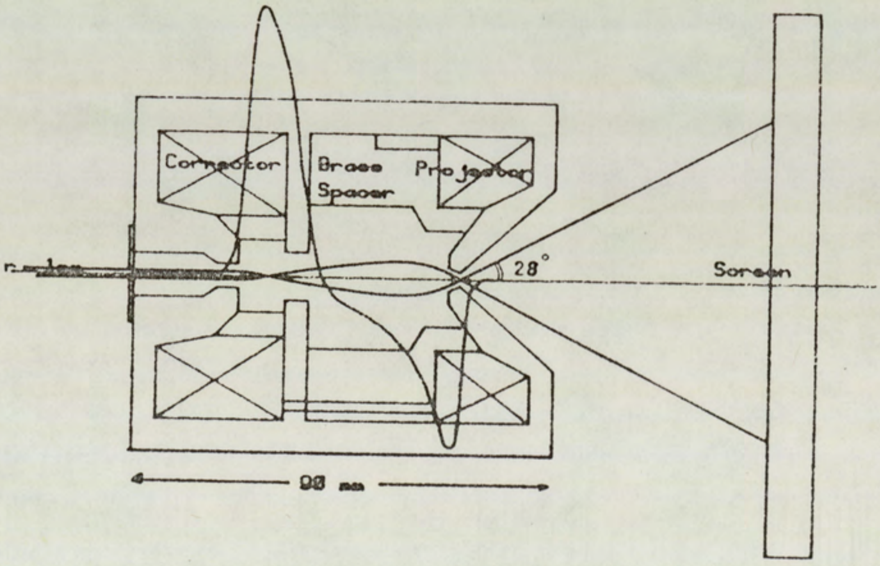

Fig.2. Cross-section of the wide-angle projector unit, showing axial field distribution and Gaussian trajectory of the extreme ray (α_p = 28°). Length of unit 90mm. Excitation of 3060A-t in the corrector and -2134 A-t in the projector at an accelerating voltage of 30KV. Average loss of ampere-turns due to field cancellation 6%. Entrance aperture 2mm dia. Effective focal length 2.2mm, projection distance 68.2mm.

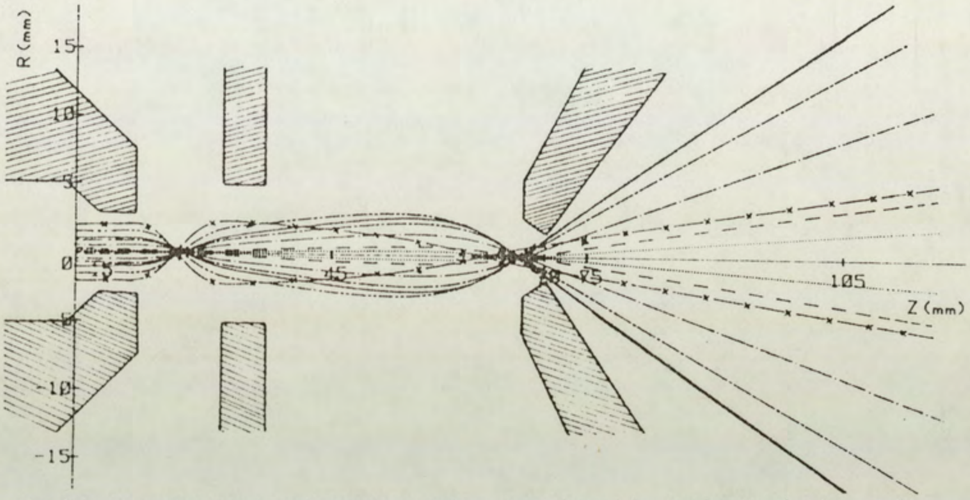

Fig.3. Computed general trajectories for the wide-angle projector unit with excitations adjusted for negligible radial and spiral distortion $NI/V_r^{1/2} = 17.8$ (corrector) and $NI/V_r^{1/2} = 12.2$ (projector). Note that failure of correction occurs , for example, if R = 2mm.

corrector lens enters the final projector lens at nearly parallel incidence (See Figure 2) which minimises the spiral distortion produced by this lens. The projector lens is of the single pole-piece type which has appreciably lower distortion than that of a conventional lens. It also has the useful property that its spiral distortion is insensitive to excitation in the region of minimum focal length. This is a critical feature of the present design since the virtual image produced by the corrector produces considerable unwanted barrel distortion in addition to the wanted spiral distortion. This means that although spiral distortion will be corrected, a considerable amount of barrel distortion will appear in the final image. Fortunately this can be readily compensated by reducing the excitation of the projector lens (Kynaston and Mulvey 1973) so as to produce an appropriate amount of pin-cushion distortion.

Third order aberration calculations carried out with the field distribution shown in Figure 2 (Nasr et al 1981, Al-Hilly 1982) show that the spiral and radial distortion can indeed be corrected simultaneously. However, such calculations give no indication of the maximum projection angle for which the calculation remains valid, or indeed the optimum polepiece configuration. This is illustrated in Figure 3 which shows the electron trajectories in the lens unit as calculated from the general ray equation. For an incident beam of radius R = 1mm ($\alpha_p \approx 30^o$) radial distortion is virtually absent. Similarly the image rotation calculations show that the spiral distortion is likewise absent. However, for a ray height R=2mm the trajectory shows that the correction no longer holds. In fact, it is necessary to provide an entrance aperture to restrict the entry of these rays, otherwise they will appear as radial streaks in the image. It can also be seen that the correct shaping of the projector polepiece is important and that further small improvements are possible. This can readily be

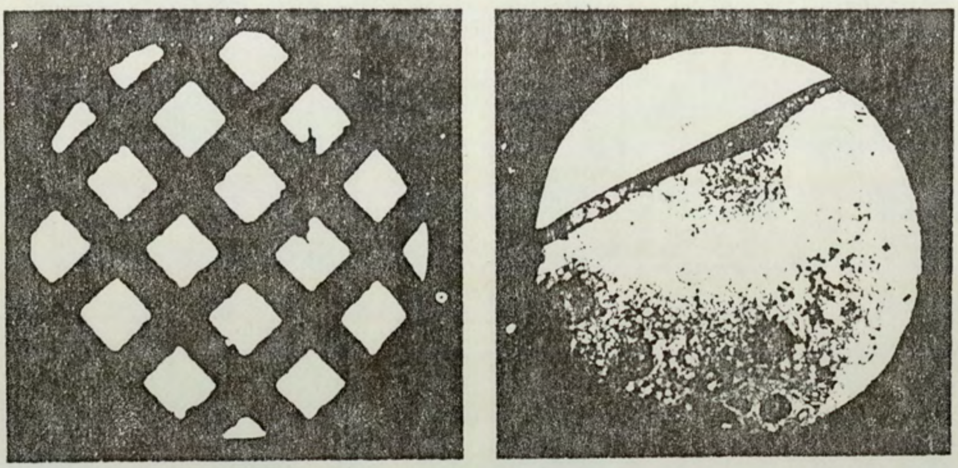

Fig.4. Wide-angle ($\alpha_p = 30^\circ$) projection images. Projection distance 68.2mm.
(a) Specimen grid (b) Rat pancreas

Diameter of image at standard projection distance (50cm) 58cm.

carried out by further computer-aided design calculations. Figure 4 shows some wide-angle images obtained in the modified "Superscope". It should perhaps be mentioned that at the standard projection distance of 50cm these images would be 58cm in diameter.

The lens unit described here has been tested at an accelerating voltage of 30kV. However, since the axial flux density in the lens unit is low (see Fig.2) it can be operated at accelerating voltages up to 220kV by suitably increasing the excitation. It should also be remembered that scaling its dimensions and excitations by a factor n leaves the distortion-free properties unchanged but reduces the magnification by a factor n. For an accelerating voltage of one million, for example, the appropriate factor n is 2.7 giving a magnification of about 13.

This investigation shows that it is now feasible to construct wide-angle projector lenses for the TEM that will allow standard size photographic plates to be located in the optimum position for minimum exposure techniques as well as providing a large distortion-free image for viewing.

References

Al-Hilly S M 1982 PhD thesis Aston University

El-Kamali H and Mulvey T 1980 Electron Microscopy 1980 (Leiden) eds. P Brederoo and G Boom Vol.1 pp74-75

El-Kamali H 1981 PhD thesis Aston University

Kynaston D and Mulvey T 1963 B. J. Appl. Phys. 14 199-206

Lambrakis E, Marai F Z and Mulvey T 1977 Inst. Phys. Conf. Ser. No. 36 PP35-38

Nasr H 1981 PhD thesis Aston University

Nasr H, Chen W and Mulvey T (These proceedings)